UNIVERSIDADE FEDERAL DO RIO GRANDE DO SUL
INSTITUTO DE FÍSICA
DEPARTAMENTO DE ASTRONOMIA

Formação Estelar Espacialmente Resolvida em Galáxias de Núcleo Ativo:

Efeitos do *Feeding* e *Feedback* na Formação Estelar [⋆]

Spatially Resolved Star Formation in Active Galactic Nuclei: Feeding and Feedback Effects on Star Formation

Nícolas Dullius Mallmann

Tese de doutorado, realizado sob orientação do professor Dr. Rogério Riffel, submetida ao programa de pós graduação em física como requisito parcial para obtenção do título de doutor em ciências.

Porto Alegre, RS, Brasil
Junho de 2023

[⋆] Trabalho financiado pelo CNPq e CAPES

Agradecimentos

Esse trabalho só foi possível através do apoio financeiro do CNPq e LINeA (Laboratório Interinstitucional de e-Astronomia), possibilitando a minha participação no projeto SDSS (Sloan Digital Sky Survey) além de suporte para esse trabalho. Também gostaria de agradecer ao pessoal do ESO (European Southern Observatory) pela experiência única durante o doutorado.

Agradeço ao Rogério Riffel que, além de um ótimo orientador, possui a paciência de um santo, o companheirismo de um irmão e o ouvido de um psicólogo. Esse trabalho e minha futura carreira, devem muito à insistência e dedicação desse ilustre profissional. Obrigado por não desistir do seu aluno depois de tantas dificuldades.

Aos meus amigos e colegas do departamento, vos agradeço pelos encontros festivos, jogos de vôlei e futsal e quaisquer momentos de descontração, fundamentais para a minha sanidade.

À minha família, agradeço o apoio e carinho que me fornecem, dos mais variados e peculiares jeitos: sejam eles um abraço, alguns tapinhas nas costas ou até mesmo um golpe de jiu-jitsu enquanto cozinho. Um agradecimento especial para meu sobrinho Thomas, cujo nascimento me fez sorrir em momentos de dificuldade e isolamento da pandemia.

Resumo

A influência do núcleo ativo de galáxias (AGN – *active galactic nuclei*) sobre a formação estelar nas galáxias hospedeiras ainda é tema de muito debate, possuindo resultados incertos e controversos. A análise do histórico de formação estelar e da cinemática do gás e das estrelas de galáxias ativas, comparadas com galáxias sem AGN, é uma das maneiras pela qual podemos estudar o problema em questão: O AGN afeta a evolução da galáxia hospedeira?

Através dos dados observados com espectroscopia de campo integral pelo projeto Mapping Nearby Galaxies at APO (MaNGA), um dos principais programas do Sloan Digital Sky Survey de quarta geração, selecionamos duas amostras de galáxias com e sem núcleos ativos para comparar os efeitos de alimentação e retroalimentação do AGN no histórico de formação estelar. Mapas e perfis radiais de diferentes propriedades (dentre elas, avermelhamento, metalicidade, populações estelares e idades médias) foram produzidos neste trabalho. A comparação da amostra de AGN com galáxias inativas revelou um crescimento na produção de populações jovens na região central de núcleos ativos bem como uma diminuição na idade média das populações estelares das galáxias hospedeiras como um todo.

Técnicas modernas de processamento de dados são necessárias para que possamos analisar o grande volume de dados obtidos por levantamentos astronômicos assim como realizar a análise estatística dos resultados. Para tal, desenvolvemos um pipeline modular, chamado URUTAU, capaz de automatizar o processamento paralelo de diversos cubos de dados (em formato padrão FITS) para diferentes propósitos conforme a necessidade do usuário. Neste trabalho, utilizamos e testamos o pipeline em um ambiente científico com o propósito de apresentar resultados científicos relevantes e produzir cubos de dados para a comunidade astronômica – que podem ser encontrados no portal do Laboratório Interinstitucional de e-Astronomia (LIneA, https://manga.linea.org.br/).

Abstract

The influence of active galactic nuclei (AGN) on the star formation of host galaxies is still subject of debate, with numerous uncertain and controversial results. The analysis of the star formation history and of the gas and stellar kinematics of active galaxies, when compared with non-active galaxies, is one way we can study the following problem: Does the AGN affect the host galaxy's evolution?

Using the integral field spectroscopy data observed by the project Mapping Nearby Galaxies at APO, one of the core programs of the fourth-generation Sloan Digital Sky Survey, we selected two galaxy samples, with and without active nuclei, in order to compare the effects of the feeding and feedback of AGN on the host galaxy's star formation history. Maps and radial profiles of different properties (such as, reddening, metallicity, stellar populations and mean age) were produced for this work. The comparison of the active and non-active galaxy samples reveal an increase in young stellar population production on the central regions of active galaxies as well as a reduced overall stellar mean age.

Modern data processing techniques are necessary for us to process the large volume of data obtained by astronomical surveys as well as to analyse the results in a statistical manner. To this end, we have developed a modular pipeline, called URUTAU, capable of automating the parallel processing of several data cubes (in standard FITS format) for different goals according to the needs of the user. In this work, we employed and tested the pipeline in a scientific environment in order to present relevant scientific results and to produce datacubes for the astronomy community – which can be found on the Laboratório Interinstitucional de e-Astronomy portal (LIneA, https://manga.linea.org.br/).

Abreviaturas

AGN: Núcleo Ativo de Galáxia (*Active Galactic Nucleus*).
IFU: Unidade de campo integral (*Integral Field Unit*).
MaNGA: Mapping Nearby Galaxies at APO
MNRAS: Monthly Notes of the Royal Astronomical Society.
MPL: MaNGA Product Launch
RSR: Razão Sinal-Ruído
SDSS: Sloan Digital Sky Survey.
SMBH: Buraco Negro Supermassivo (*Supermassive Black Hole*)
SSP: População Estelar Simples (*Simple Stellar Population*)

Conteúdo

Lista de Figuras

Capítulo 1

Introdução

A formação e evolução de galáxias é governada por uma série de processos, sendo esses divididos, a grosso modo, em processos internos e ambientais. Uma questão em aberto refere-se ao controle do tamanho das galáxias no momento presente. Em modelos de formação e evolução de galáxias, o tamanho final dos objetos é controlado por processos de *feedback*, por exemplo: ventos causados pela acreção de material ao núcleo ativo, jatos de gás ionizado e radiação devido ao material circumnuclear aquecido. Esses processos, geralmente, são inclusos em simulações de modo *ad-hoc*. No presente trabalho, investigo a influência dos processos de *feedback* do Núcleo ativo de galáxia (AGN – *active galactic nuclei*) na formação estelar das galáxias hospedeiras. Para tal desenvolvi uma ferramenta de análise de cubo de dados para processar os cubos de dados utilizados nesse trabalho.

1.1 Núcleos Ativos

Existem galáxias cuja luminosidade na região central (não resolvida) excede o que é esperado puramente da contribuição da emissão estelar. Esse excesso é caracterizado por luminosidades bolométricas da ordem de 10^{42} à 10^{48} $ergs/s$ concentrados em volumes menores que 1 pc^3 e variações temporais na intensidade luminosa (Peterson, 2009). Com a impossibilidade de atribuir às estrelas a causa desse fenômeno energético, algumas hipóteses foram formuladas com o intuito de explicar essa ocorrência. A hipótese mais aceita descreve a conversão de energia potencial gravitacional em luminosa através da alimentação de buracos negros supermassivos (SMBH – *supermassive black holes*). Inúmeras galáxias, em especial as mais massivas, possuem evidências de SMBH nas suas regiões centrais[1] e, conforme a hipótese de acreção de matéria, quando o buraco negro atrai o material circumnuclear próximo, o gás espirala em direção ao centro e aquece devido a própria viscosidade (fricção interna), resultando na excitação das partículas e, consequentemente, emitindo grandes quantidades de fótons ao tentar se esfriar ou através de colisões internas. Esse disco de gás, chamado de disco de acreção, possui uma camada interna mais espessa devido à temperaturas elevadas e uma camada mais externa fria e estreita cuja espessura aumenta com a distância ao SMBH (Peterson, 2009). Outra contribuição energética é causado pelo forte campo magnético gerado no entorno do buraco negro, transportando partículas carregadas em direções perpendiculares ao disco de acreção e formando jatos relativísticos de partículas que, ao entrar em contato com o meio interestelar, transferem sua energia e geram lóbulos de emissão em rádio. Atribuímos a esses efeitos energéticos nas regiões centrais de galáxias a denominação de núcleos ativos de galáxias. Núcleos ativos são classificados conforme o espectro de emissão (veja Beckmann & Shrader, 2012, para detalhes), cuja fenomenologia é descrita através do Modelo Unificado de AGNs. Esse modelo atribui a todos os diferentes objetos com núcleos ativos o mesmo fenômeno de origem, cuja variação observada é devida à efeitos geométricos (torus) ou ocultação por nuvens de poeira da fonte central (Ramos Almeida & Ricci, 2017). A figura 1.1 ilustra o Modelo Unificado.

1.2 *Feeding* e *Feedback*

A evolução de galáxias é um processo intrinsecamente complicado. A extensão e a quantidade de matéria envolvida produz uma heterogeneidade de processos que conduz o desenvolvimento de sua estrutura. Cada processo – seja ele a formação ou explosão de uma estrela, o esfriamento ou aquecimento do gás interestelar, ou até mesmo a interação com outras galáxias – é capaz de se comunicar com outros através de trocas de energia e matéria, denominados de processos de alimentação (*feeding*) e retroalimentação (*feedback*), resultando em coevolução das estruturas e componentes das galáxias (Storchi-Bergmann & Schnorr-Müller, 2019).

Uma importante fase na evolução de galáxias é caracterizada pelo núcleo ativo. A alimentação do SMBH pelo disco de acreção produz efeitos de retroalimentação altamente energéticos: jatos de partículas relativísticas emitidos do interior do disco

---

[1] Primeira imagem confirmando a existência de um SMBH no centro de uma galáxia, M87, e do disco de acreção foi obtida via observações com os telescópios do Event Horizon em 2019.

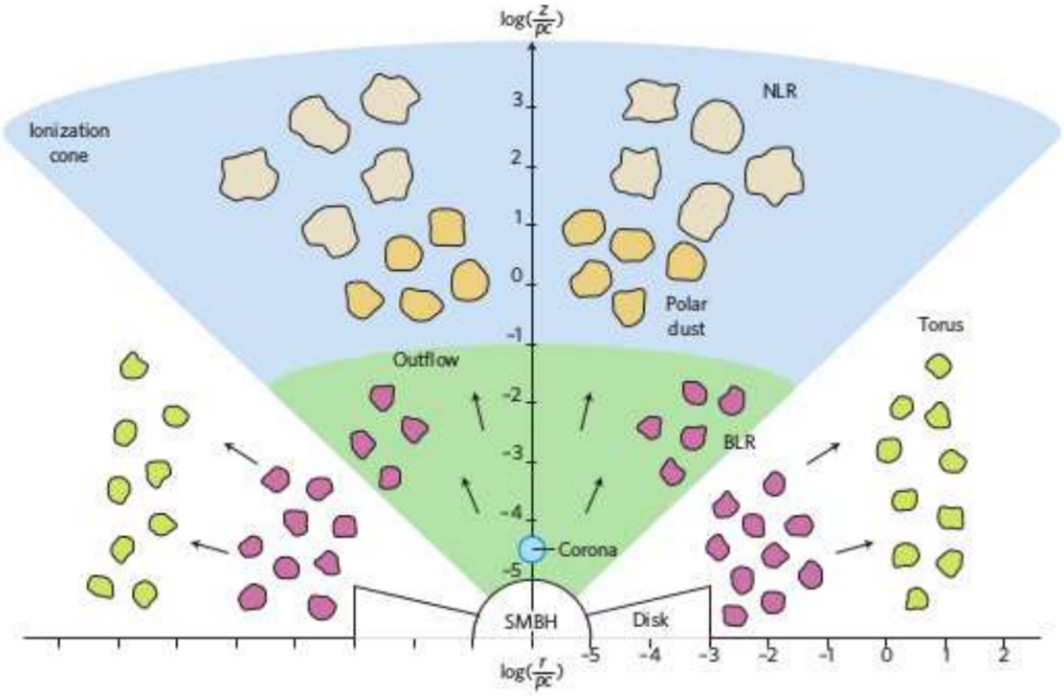

(a)

Figura 1.1: Esquematização do Modelo Unificado: O buraco negro supermassivo (SMBH) atrai material da galáxia hospedeira, formando o disco de acreção (Disk) que o alimenta. Circundando o disco de acreção, nuvens de gás e poeira (Torus) cobrem parcialmente a região central. O *feedback* do AGN resulta em *outflows* de partículas relativísticas que gera um cone de ionização (Ionization Cone) ao interagir com o material da galáxia hospedeira. Diversas linhas de emissão do espectro de um AGN são gerados em duas regiões: Região de linhas estreitas (*Narrow-Line Region*; NLR) e a Região de linhas largas (*Broad-Line Region*; BLR). Como o próprio nome diz, a NLR gera linhas estreitas de baixa dispersão de velocidades enquanto que a BLR gera linhas largas de alta dispersão. Figura retirada de Ramos Almeida & Ricci (2017).

de acreção, ventos emanando de sua região mais externa e radiação emitida pelo plasma quente do disco ou de sua coroa (Elvis, 2000, Ciotti et al., 2010). Acredita-se que esses processos de alimentação e retroalimentação relacionados ao SMBH conectam o crescimento do buraco negro com o crescimento de inúmeras galáxias e, consequentemente, são apontados como principais responsáveis pela correlação entre a massa do SMBH e a massa do bojo da galáxias (Somerville et al., 2008, Kormendy & Ho, 2013). Estudos precedentes associam estrelas massivas jovens à características da distribuição de energia de AGNs – excesso no azul e diluição das linhas em absorção (Terlevich et al., 1990) – sugerindo uma possível associação entre núcleos ativos e formação estelar. Trabalhos posteriores (Kauffmann et al., 2003, Cid Fernandes et al., 2004, Riffel et al., 2009, Mallmann et al., 2018, Burtscher et al., 2021, Dahmer-Hahn et al., 2022, Riffel et al., 2022), utilizando espectroscopia de fenda longa e unidades de campo integral (IFUs), encontraram um acréscimo na contribuição luminosa de populações estelares jovens em galáxias ativas quando comparadas com galáxias não ativas. Os indícios de aumento da formação estelar em galáxias ativas levou à proposta de um cenário, chamado de *feedback* positivo, na qual o fluxo de gás direcionado à região central da galáxia é parcialmente convertida em estrelas (em uma região circumnuclear) e parcialmente acretada pelo núcleo, responsável pela ignição do AGN (Storchi-Bergmann et al., 2001, Hopkins, 2012).

1.3 Formação Estelar em Galáxias com AGNs

Não há um consenso acerca do efeito de AGNs na formação estelar de galáxias hospedeiras. Simulações computacionais de crescimento e evolução de galáxias (e.g., Croton et al., 2006) utilizando o resultado de simulações cosmológicas indicam uma possível dependência do *feedback* de núcleos ativos no tamanho das galáxias. Estes autores mostram que quando a simulação não dispõe de fontes centrais de aquecimento (e.g. $feedback$ de AGN, veja figura 1.2), resulta em uma quantidade de galáxias de alta luminosidade que não condiz com o que é observado no universo – ou seja, há um forte indício de que núcleos ativos são importantes para suprimir a produção de estrelas em galáxias mais massivas. Por outro lado, modelos e simulações de fluxo de gás nas centenas de parsecs centrais, nas redondezas do AGN, resultam em episódios de formação estelar circumnuclear (Kormendy & Ho, 2013, Heckman & Best, 2014, Zubovas & Bourne, 2017). Em particular, Zubovas & Bourne (2017) sugere que há um limite de luminosidade do AGN para o qual a retroalimentação do núcleo ativo induz a fragmentação de nuvens de gás: valores acima desse limite resultam em uma remoção eficiente do gás, impedindo a fragmentação das nuvens e, por consequência, a formação estelar.

Tanto a formação estelar, quanto o $feeding$ do AGN dependem da quantidade de gás disponível. Um ponto ainda em aberto, é se a formação estelar e a alimentação do AGN são coevas (Kawakatu & Wada, 2008), ou se a alimentação do SMBH ocorre após uma fase de intensa formação estelar (Cid Fernandes et al., 2005, Davies et al., 2007, 2009, Riffel et al., 2009, 2015, Mallmann et al., 2018, Riffel et al., 2022) ou, ainda se esses dois eventos são completamente desconexos (Sarzi et al., 2007, Hicks et al., 2013).

Uma maneira de testar esses cenários é mapeando o histórico de formação estelar de galáxias ativas e compará-las com galáxias inativas com as mesmas propriedades físicas das hospedeiras de AGNs (e.g., massa estelar, morfologia). Com esse intuito elaboramos uma amostra de galáxias ativas e suas controles inativas a partir do dados observados pelo Sloan Digital Sky Survey de quarta geração (SDSS-IV) com o projeto Mapping Nearby Galaxies at APO (MaNGA). A amostra selecionada do MaNGA Product Launch 5 (MPL5) está discutida em Rembold et al. (2017) e a amostra final contendo 293 AGNs e suas controles está descrita no Cap. 7.

Resultados obtidos utilizando a amostra descrita em Rembold et al. (2017), sugerem que populações estelares jovens são mais frequentes em AGNs mais luminosos que nas suas galáxias de controle. Bem como, também encontramos que no caso das AGNs de baixa luminosidade as populações jovens não são mais frequentes que nas galáxias de controle. Estes resultados estão de acordo com os resultados que encontramos para a amostra parcial, discutida em Mallmann et al. (2018). Neste trabalho também concluímos que as AGNs estão sofrendo um rejuvenescimento de sua população estelar na região central. Contudo, essa nossa amostra era limitada a algumas dezenas de AGNs, e quando a separação em luminosidade é feita, os resultados estatísticos não são robustos. O *survey* MaNGA finalizou a coleta de dados (Abdurro'uf et al., 2022), permitindo que, durante o período de doutorado, analisássemos todos os AGNs da amostra observada pelo *survey*. Os resultados referentes as populações estelares estão discutidos nos Cap. 6 e 7.

1.4 Objetivo deste Trabalho

A interdependência entre formação estelar circumnuclear e a atividade nuclear de galáxias pode ser estudada através da investigação da presença de populações estelares de diferentes idades em regiões próximas ao núcleo (centenas de *pc*). Há três

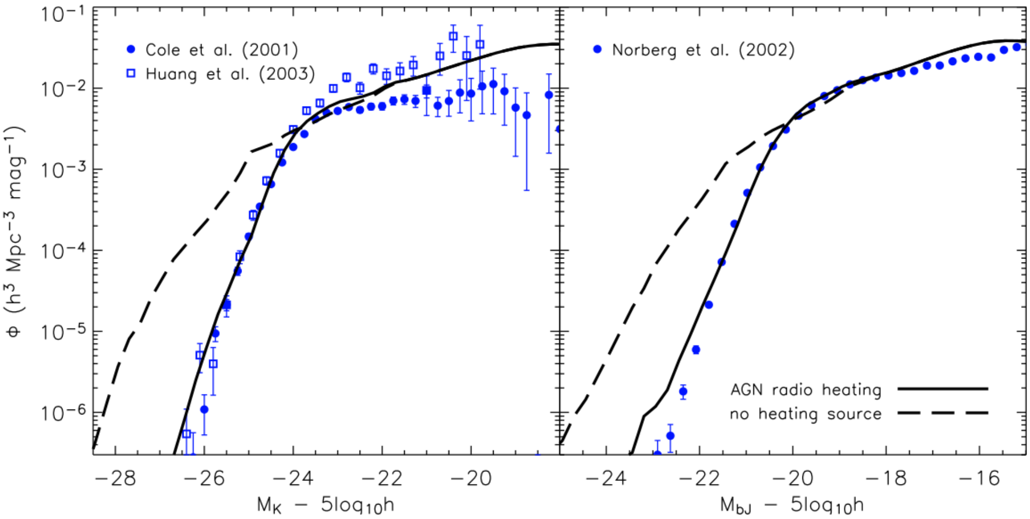

(a)

Figura 1.2: Simulação do crescimento e evolução de galáxias (Croton et al., 2006). Linha tracejada mostra a discrepância entre simulação e observação (pontos azuis) quando AGNs não são incluídos nos cálculos. A linha sólida representa os valores da simulação com adição *ad-hoc* de AGNs.

possíveis cenários em consideração nesse trabalho: (i) estrelas jovens dominando a luminosidade do espectro em AGNs indicando formação estelar coexistente com a atividade nuclear, ou seja, parte do material interestelar é usado para formar estrelas e parte para alimentar o SMBH; (ii) domínio de populações de idade intermediária em galáxias com núcleo ativo apontando para uma baixa formação estelar e a alimentação do buraco negro através de material ejetado pelas estrelas evoluídas ou atividade nuclear elevada suprimindo a geração de novas estrelas através de ventos e aquecimento das nuvens moleculares; (iii) presença majoritária de estrelas velhas e evoluídas implica em um fluxo de gás ao SMBH eficiente, cujo material não contribui significativamente para a formação estelar. O mapeamento de populações estelares de diferentes idades em galáxias com AGNs e galáxias sem atividade nuclear é fundamental para o estudo dos casos citados, possibilitando um avanço na compreensão dos processos envolvidos na alimentação de SMBHs.

Nosso objetivo é mapear espacialmente o histórico de formação estelar em AGNs e compará-lo com o de galáxias inativas com as mesmas propriedades das galáxias hospedeiras de AGNs (ex. luminosidade, massa estelar, morfologia, etc), e estudar os efeitos da luminosidade do AGN na formação estelar. Selecionamos 293 galáxias com núcleos ativos e 586 galáxias de controle observadas pelo *survey* Mapping Nearby Galaxies at Apache Point Observatory (MaNGA – ver seção 2.1) neste trabalho.

Contudo, vale ressaltar que o estudo de cubos de dados é extremamente complexo, pois esses contém uma grande quantidade de informações (Steiner et al., 2009) e a análise de um cubo de dados pode ser comparada a análise de dezenas a uma centena de milhares de espectros individuais (e.g. cubos do MaNGA tem tipicamente 4 mil spaxels, enquanto cubos do MUSE/VLT podem ter ∼100 mil spaxels). Portanto, acessar e manipular tamanha quantidade de informação, como a contida nos mais de 10 mil cubos de dados do MaNGA não é uma tarefa trivial. A fim de atingirmos os objetivos científicos propostos, desenvolvemos uma ferramenta modular chamada URUTAU (capítulo 4) e utilizamos o código STARLIGHT para síntese de populações estelares (capítulo 3) e construímos MEGACUBOS com as propriedades que derivamos para todas as 10 234 galáxias disponíveis no *survey* e as disponibilizamos para a comunidade (Veja Cap. 6). Essa ferramenta, por ser modular, é flexível e de fácil aplicação em qualquer cubo de dados (discutimos exemplos de aplicação em cubos de dados de distintos instrumentos no Cap. 8.1).

Capítulo 2

Dados

2.1 MaNGA

Os dados utilizados nessa tese são do survey Mapping Nearby Galaxies at APO (MaNGA) que é um dos três principais programas do Sloan Digital Sky Survey de quarta geração (SDSS-IV). O projeto tem como objetivo investigar a estrutura cinemática e composição química do gás e estrelas visando entender a evolução das galáxias e os processos que regulam a formação de suas componentes. Para tal, o MaNGA mapeou o fluxo de 10 235 galáxias próximas ($\langle z \rangle \approx 0.03$) com massas estelares $M_\star > 10^9 M_\odot$. Para mais detalhes veja Bundy et al. (2015) e Abdurro'uf et al. (2022).

O MaNGA utiliza um telescópio de 2,5 metros do Sloan, dedicado ao SDSS, no Apache Point Observatory (APO). As observações são feitas com unidades de campo integral (*Integral Field Unit*; IFU) compostos por um conjunto de 19 a 127 fibras ópticas agrupados em estruturas hexagonais, cobrindo campos de $12''$ a $32''$. Uma imagem do IFU pode ser vista na figura 2.1a e um exemplo do campo observado na figura 2.1b. Cada fibra alimenta um dos dois espectrógrafos BOSS, desenvolvidos anteriormente para o SDSS-III (Smee et al., 2013), que são capazes de fornecer uma cobertura espectral de 3600 Å à 10300 Å, com um poder de resolução médio de $R \sim 2000$. Para uma leitura mais técnica do design do IFU e estratégias de observação, recomenda-se ler Drory et al. (2015) e Law et al. (2015).

Inicialmente foi selecionada uma amostra de AGNs pertencentes ao MaNGA e uma amostra de controle. Essa amostra inicial, continha 62 AGNs selecionados do MPL-5 (contendo 2778 galáxias no total) e está descrita em Rembold et al. (2017). Em resumo, o método aplicado consiste em utilizar os dados espectrais dessas galáxias, obtidas no Data Release 12 (DR12) do SDSS-III, para calcular tanto

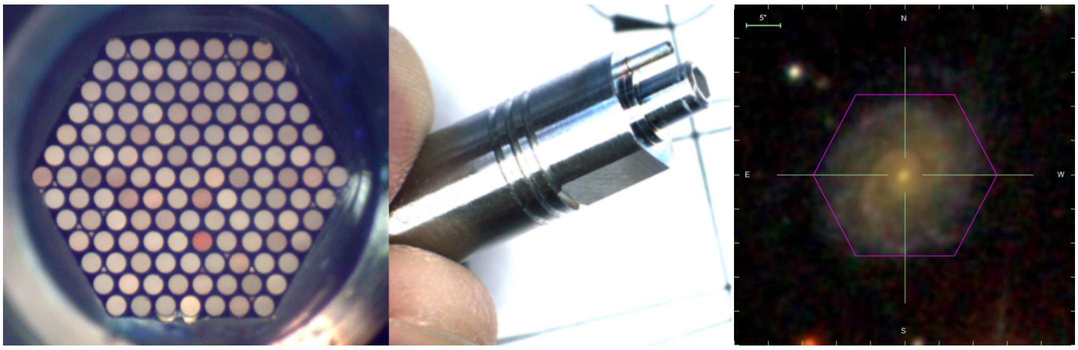

(a) (b)

Figura 2.1: Exemplo (a) de um conjunto de fibras do IFU do MaNGA, composto por 127 fibras, e (b) do campo de observação para a galáxia MaNGA ID 1-114306.

fluxos de linhas quanto larguras equivalentes (Hβ, Hα, [OIII]λ5007, [NII]λ6584). Com os valores de fluxos e larguras equivalentes, a identificação das galáxias ativas foi realizada empregando dois diagramas diagnóstico, BPT (Baldwin et al., 1981) que envolve as razões de linhas [NII]λ6584/Hα × [OIII]λ5007/Hβ e WHAN (Cid Fernandes et al., 2010, 2011) que usa a razão [NII]λ6584/Hα × EW(Hα). Esses diagramas foram desenvolvidos para identificar o mecanismo de ionização do gás que produz as linhas de emissão observadas. Para que uma galáxia observada pelo MaNGA fosse classificada como AGN e, consequentemente, adicionada à nossa amostra, ela deve ser classificada como AGN em **ambos os diagramas citados** (veja a figura 2.2 para a amostra final). A necessidade de utilizar ambos os diagramas se dá pelo fato do diagrama BPT não diferenciar AGNs com baixa ionização de galáxias com linhas de emissão geradas por estrelas evoluídas de baixa massa, caracterizadas por EW(Hα) < 3 Å (Cid Fernandes et al., 2010, Sánchez, 2020, Sánchez et al., 2021).

Uma segunda amostra, contendo galáxias inativas, foi selecionada através do pareamento de propriedades físicas dos AGNs desse trabalho. Para construir essa amostra, foram selecionadas diversas galáxias inativas, para cada AGN, cujo *redshift* z e massa estelar $M_\star$ não diferissem por 30% dos respectivos valores da galáxia ativa. Através da análise morfológica (razão dos eixos, tipo de Hubble, presença de barras, etc.), o número de candidatas à controle foi reduzido, chegando em alguns casos à duas galáxias por AGN. Para manter a amostra de controle mais homogênea, foram escolhidas apenas as 2 melhores galáxias de controle para cada galáxia ativa. A seleção resultou em uma amostra de controle com 109 objetos (ao invés de 124) pois 12 objetos da amostra de controle foram pareados com mais de um AGN. As populações estelares dessa primeira amostra foi estudada em Mallmann et al. (2018).

Com o término das observações realizadas pelo survey MaNGA, foi possível atualizar e expandir a nossa amostra de galáxias com núcleos ativos. Aplicando a metodologia descrita acima (e.g. ser classificada como AGN tanto no BPT quanto no WHAN), encontramos em 298 galáxias com núcleos ativos observadas pelo survey MaNGA.

Seguindo a metodologia de Rembold et al. (2017), foi atualizado a amostra de controle de galáxias não ativas cujas propriedades seguintes se assemelham a das galáxias com AGN: redshift, massa estelar e morfologia. Foram selecionados, do data release 17 (DR17) do MaNGA, como potenciais galáxias de controle, os objetos que apresentam linhas de emissão ou cujas linhas não foram detectadas nos espectros de fibra única do SDSS-III, exceto pelas galáxias já classificadas como AGN (ver acima). Além dos objetos sem linhas de emissão presentes, potenciais galáxias de controle são aquelas localizadas, dentro da incerteza, na região de formação estelar do diagrama BPT ou no caso em que o diagrama WHAN indica que a ionização do gás não resulta de região AGN. Esses compreendem objetos ionizados por estrelas jovens ou por estrelas evoluídas de baixa massa quentes ("hot, low-mass evolved stars" - HOLMES). Para cada AGN, foi designada uma subamostra preliminar de galáxias não ativas com redshift e massas estelares (com desvios menores que 30%) semelhantes. Essa subamostra preliminar (tipicamente com centenas de objetos) é então inspecionada visualmente e as duas galáxias cuja morfologia e razão de eixos melhor se equiparam com o AGN são selecionadas como amostra controle da galáxia com núcleo ativo. Da amostra de AGNs, apenas cinco objetos (MaNGA id 1-37440, 1-189584, 31-115, 1-641156 e 1-300461) não possuem galáxias de controle – ou por que o redshift está próximo demais dos limites de observação do MaNGA (ex., 1-189584 com $z = 0.0037$), ou por possuírem uma morfologia distinta e irregular (ex., 1-641156).

A amostra final de AGNs consiste em 293 galáxias, cada uma pareada com duas galáxias de controle. A amostra de controle contém 492 objetos, menos do que o esperado (586), pois algumas galáxias de controle foram pareadas com múltiplos AGNs. As tabelas com todos os objetos se encontram no Cap. 7.

Para verificar a qualidade das amostra de controle selecionada, foi utilizado o teste de Kolmogorov-Smirnov, capaz de indicar se distribuições (neste caso, massa estelar e redshift das amostras de AGN e de controle) são efetivamente indistinguíveis. A Fig. 2.3 mostra a distribuição de redshift, massa estelar, dispersão de velocidade estelar e luminosidade do [O III]. Além disso, de acordo com o projeto Galaxy Zoo (Lintott et al., 2011), 32%, 60% e 5% das galáxias com núcleos ativos são, respectivamente, elípticas, espirais e mergers. Essa distribuição morfológica se repete na amostra de controle, contento 35% de galáxias elípticas, 61% de galáxias espirais e 2% de mergers. Também foi utilizado o parâmetro T-TYPE entre galáxias AGN e controle de Vázquez-Mata et al. (2022) e verificado que ambas as distribuições são similares. Para mais detalhes, ver Rembold et al. (2017).

Na presente tese são apresentados os resultados a cerca da formação estelar na amostra de AGNs comparados com as das galáxias controle, bem como uma análise espacial do mecanismo dominante na excitação do gás em ambas as amostras.

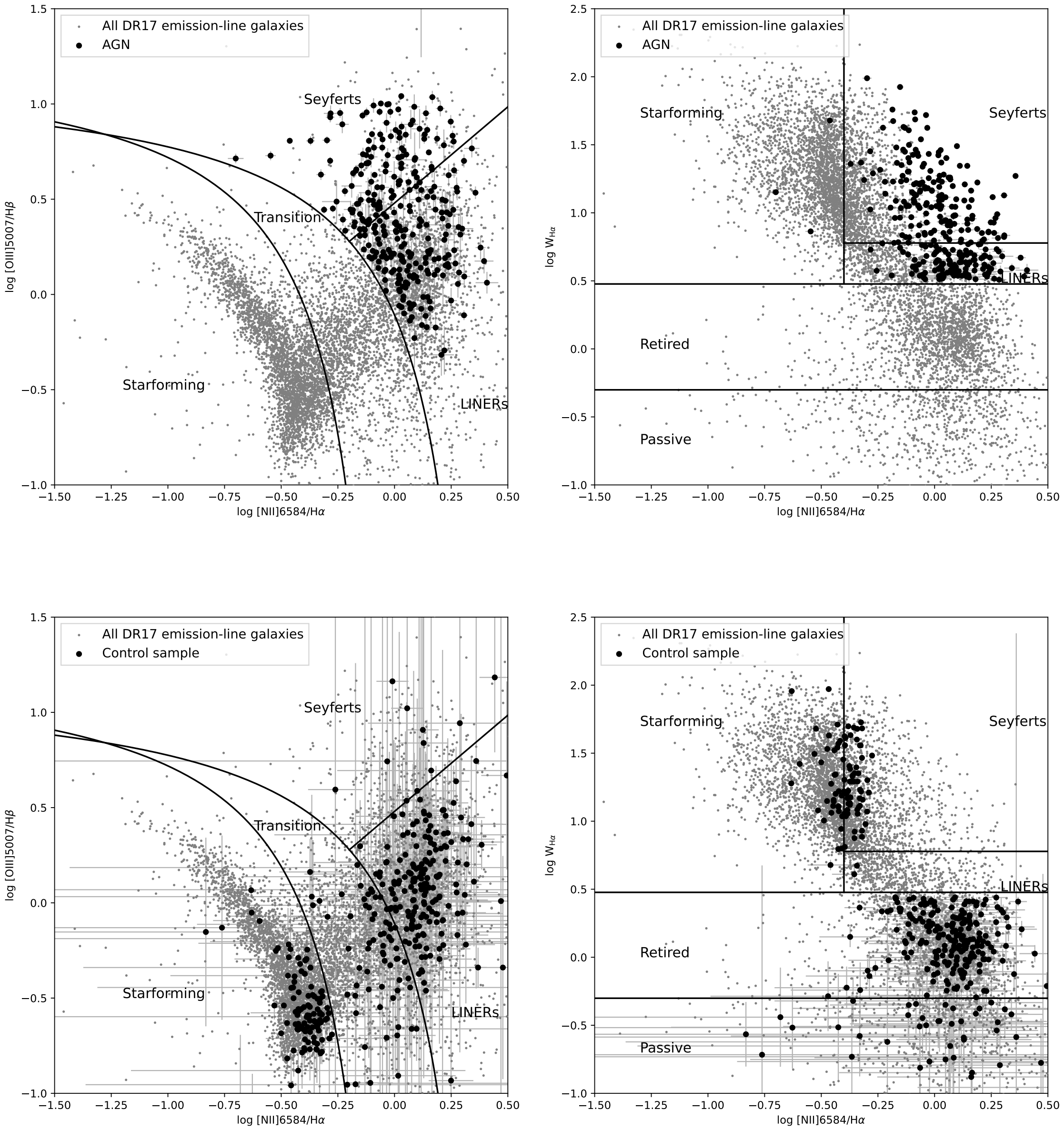

Figura 2.2: Diagramas BPT e WHAN gerados para a amostra final do MaNGA (superiores para as AGNs e inferiores para as controles). Pontos cinzas são todas as galáxias com linhas de emissão, pontos pretos são os AGNs. Figuras baseadas em Rembold et al. (2017).

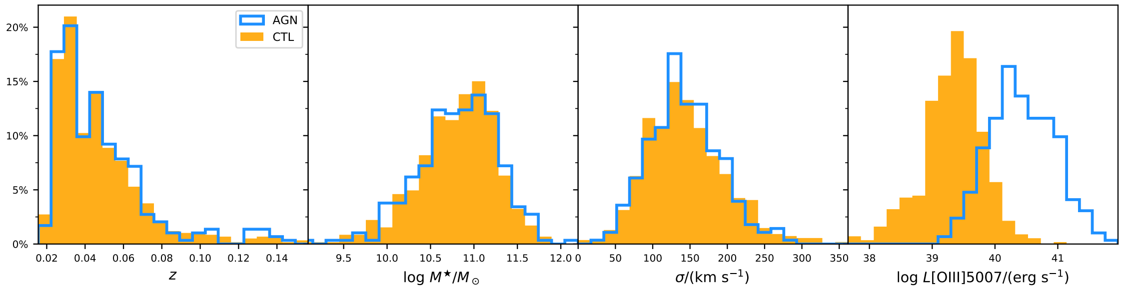

Figura 2.3: Distribuição das duas amostras, AGNs e galáxias de controle, para quatro propriedades. Para o *redshift*, massa estelar e magnitudes na banda r as duas amostras são semelhantes. Já para a luminosidade , a distribuição de galáxias ativas está deslocada em relação a das controles pois é um indicador da intensidade do AGN. Figura retirada de Rembold et al. (2017).

Capítulo 3

Síntese de Populações Estelares

Quando analisamos objetos celestes, não há melhor propriedade física para escrutinar que a luz emitida ou refletida pelos diversos componentes do universo: galáxias, estrelas, aglomerados de estrelas, nuvens de gás e poeira, planetas, etc. Isso é consequência clara das distâncias envolvidas em estudos astronômicos e das condições físicas irreprodutíveis em laboratórios científicos na Terra. Não é a toa que diversas técnicas para analisar a luz de astros foram desenvolvidas ao longo da história – de simples observações à olho nu à medições fotométricas, de medidas de dispersão do espectro à métodos matemáticos para discretizar os componentes químicos responsáveis por linhas de absorção e emissão. A técnica de síntese de populações estelares é apenas uma dentre todas essas técnicas, mas é de grande importância no estudo das componentes que formam galáxias e o histórico da evolução.

A complexidade de uma galáxia é inquestionável. Compostas por inúmeras estrelas, volumosas nuvens de gás e poeira, campos gravitacionais e eletromagnéticos complexos e intensa radiação, galáxias possuem inúmeras fontes de emissão e absorção causadas via interações entre seus componentes – dentre essas, pode-se citar algumas, tais como: gás esfriando e formando estrelas, estrelas envelhecendo e enriquecendo o ambiente com metais, radiação intensa corroendo ou aquecendo nuvens, núcleos ativos produzindo energia através da acreção de matéria a um buraco negro supermassivo. Ao observarmos uma galáxia, é impossível discriminar todos os componentes e interações através de medidas espacialmente resolvidas devido às escalas de distâncias envolvidas. Entretanto, podemos inspecionar o espectro integrado, contendo o somatório das fontes de emissão e reflexão da luz.

Neste capítulo, discutiremos brevemente algumas facetas de espectros integrados de populações estelares (seção 3.1), o que são modelos populações estelares simples e a técnica de síntese de populações estelares (seção 3.2) e, por fim, descreveremos o código utilizado para produzir espectros sintéticos a partir dessa técnica (seção 3.3).

3.1 Populações Estelares e Espectros Integrados

Conforme o paradigma atual de formação estelar, estrelas não se formam isoladamente. Durante o colapso de nuvens de gás, assimetrias no campo gravitacional e radiativo resultam em diversas regiões de sobredensidade, causando fragmentação da nuvem. Cada uma dessas sobredensidades tem o potencial de colapsar e formar um sistema estelar e o conjunto de estrelas formadas nesse processo constitui uma população estelar. É importante salientar que numerosos fatores podem influenciar a composição e a evolução de uma população estelar em formação, dentre estes: estrelas massivas podem evoluir rapidamente e explodir em uma supernova que enriquece o gás e outras estrelas com metais, inomogeneidades químicas na nuvem original (assim como interações com outras nuvens) alteram a taxa de formação e composição da população estelar em desenvolvimento, radiação de fontes intensas (como de um núcleo ativo) podem aquecer o gás e impedir o colapso da nuvem ou até mesmo destruí-la (Mo et al., 2010).

As limitações de resoluções espaciais nos telescópios atuais não nos permitem a observação de estrelas individuais (com algumas exceções) mesmo nas galáxias mais próximas. É consequência dessa limitação que os espectros medidos são composições da luz de diversas populações estelares e outros componentes luminosos (e.g., AGN, gás quente) ou iluminados (e.g., nebulosas de reflexão). A priori, podemos tirar várias informações úteis sobre as componentes de um espectro integrado simplesmente analisando a declinação do continuo (figura 3.1). Espectros cuja energia é dominada nas frequências mais altas (mais “azul”) podem indicar a presença de mais populações estelares jovens do que velhas, enquanto que um espectro mais “vermelho”aponta para o caso oposto. Essa regra, entretanto, não é sempre verdade. Existe um fator de degenerescência causado pela metalicidade das populações estelares, quanto maior a metalicidade, mais avermelhado o espectro fica.

Para tentar resolver esses problemas de resolução limitada e de degenerescência, se faz necessário o estudo e a utilização de modelos de populações estelares robustos que possam reproduzir os espectros observados ao mesmo tempo que fornecem medidas de propriedades físicas plausíveis.

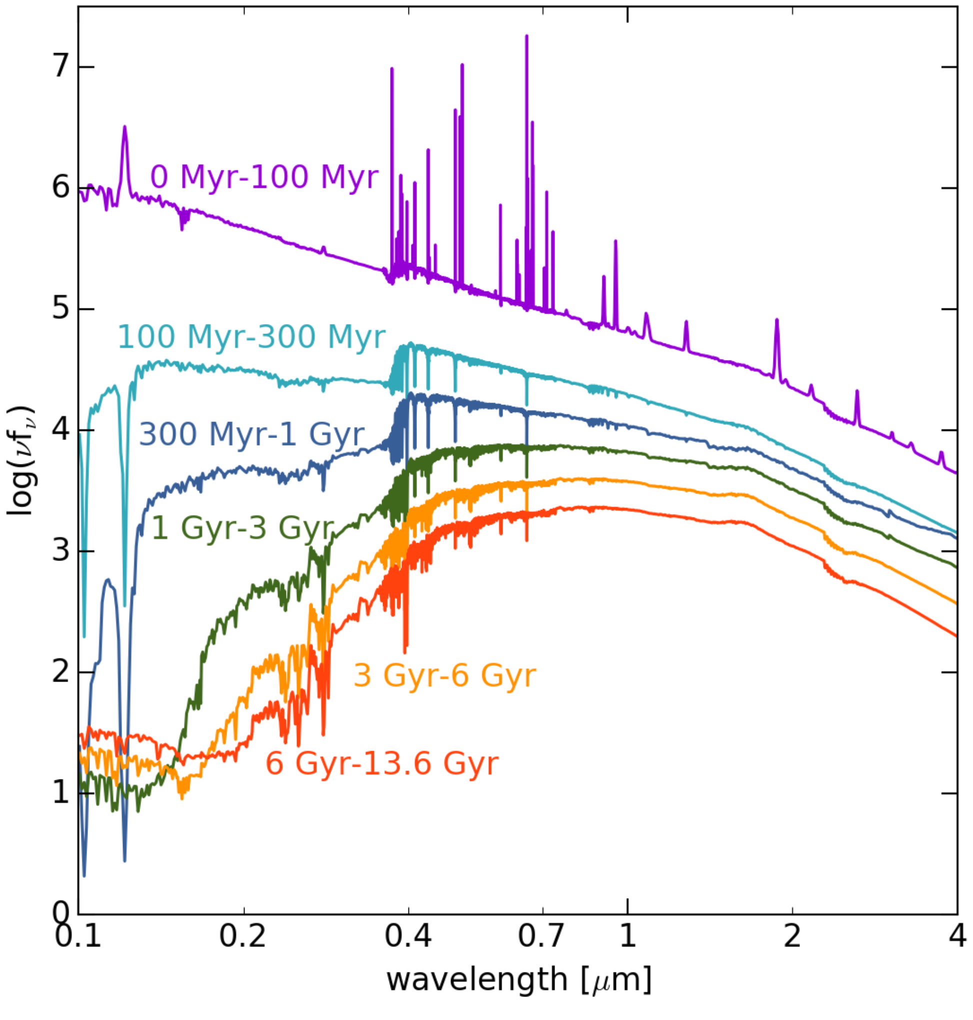

(a)

Figura 3.1: Exemplos de espectros integrados com diferentes declinações no contínuo. Essa variação resulta em populações estelares com diferentes cores. Espectros azulados podem sinalizar a presença de populações jovens ou populações pouco metálicas, já espectros avermelhados costumam indicar o contrário. Figura retirada de Leja et al. (2017).

3.2 Populações Estelares Simples e o Método de Síntese de Populações Estelares

O modelo mais simples de população estelar que podemos usar para averiguar os componentes responsáveis por um espectro integrado é o modelo de população estelar simples (SSP – *Simple Stellar Population*). Conceitualmente, uma SSP é uma população de estrelas coevas e de metalicidade uniforme, formadas de uma mesma nuvem de gás num colapso instantâneo (em uma escala de tempo desprezível frente a idade da população). Obviamente, uma SSP é uma idealização que abstrai diversas nuances ocorrentes durante a evolução de uma população estelar. É sabido modernamente que aglomerados estelares (que por um longo período foram considerados como uma população simples) na verdade são populações compostas (e.g. Bastian & Lardo, 2018). Felizmente, pode-se construir modelos evolutivos de populações estelares simples (EPS). Esses modelos podem ser completamente teóricos (e.g. usando bibliotecas estelares teóricas) ou utilizando bibliotecas empíricas em sua construção. Ambas as classes de modelos (puramente teóricos ou empíricos) por sua vez representam bem as características espectrais de aglomerados estelares (Cid Fernandes et al., 2010, Ahumada et al., 2019, Martins et al., 2019). Contudo, esses modelos EPS também possuem limitações de bibliotecas de espectros estelares, que no caso de bibliotecas teóricas esbarram no nosso entendimento a cerca da física dos processos que ocorrem no interior e nas atmosferas estelares, parâmetros atômicos ou no caso de bibliotecas empíricas nas limitações observacionais (e.g. Riffel et al., 2015, Lançon et al., 2021). Ao longo dos anos, muitos esforços foram feitos com o intuito de construir bibliotecas de populações estelares simples, o que resulta num grande número de modelos disponíveis (veja Conroy, 2013, para uma revisão). Contudo, estudos tem demonstrado que de um modo geral, na região do óptico os modelos apontam resultados coerentes entre si (e.g. Chen et al., 2010, Dahmer-Hahn et al., 2018).

Utilizando um conjunto representativo de SSPs (uma base de SSPs), contendo idades e metalicidades variadas, podemos empregar o método de síntese de populações estelares no estudo de espectros integrados. Essa técnica parte do pressuposto que espectros observados são resultados de medições da luz de inúmeras populações estelares contidas no mesmo *spaxel* (mistura de *spectral* e *pixel*). A variação mais simples dessa técnica mistura o espectro de populações estelares (no nosso trabalho, SSPs), em diferentes proporções de contribuição luminosa, para gerar um espectro final semelhante ao observado. Através das contribuições resultantes, podemos extrair uma miríade de informações: idade média, metalicidade média, histórico de formação, taxa de formação estelar, etc. Para aplicar o método de síntese de populações estelares, utilizamos o código STARLIGHT, descrito na próxima seção.

3.3 Código STARLIGHT

O código STARLIGHT é uma ferramenta que nos permite discretizar a contribuição das populações estelares que compõem um espectro integrado. Utilizando um conjunto base de $N_\star$ espectros ($b_{j,\lambda}$), o código produz diversas combinações dos elementos da base para modelar o espectro observado O_λ. Para sintetizar o espectro modelo M_λ, o programa normaliza os elementos da base em um comprimento de onda arbitrário λ_0, avermelha o espectro com o fator $r_\lambda = 10^{-0.4(A_\lambda - A_{\lambda_0})}$, atribui um peso ao vetor de população x_j (que representa a contribuição do j-ésimo elemento da base ao fluxo do espectro no comprimento de onda de normalização λ_0) e utiliza uma convolução Gaussiana $G(v_\star, \sigma_\star)$ para adicionar os efeitos cinemáticos nos espectros da base. Esses procedimentos são expressos pela equação:

$$M_\lambda = M_{\lambda_0} \left[\sum_{n=1}^{N_\star} x_j \, b_{j,\lambda} \, r_\lambda \right] \otimes G(v_\star, \sigma_\star) \tag{3.1}$$

onde M_{λ_0} é o fluxo sintético no comprimento de onda de normalização λ_0.

A qualidade da síntese é monitorada através da redução do valor da equação $\chi^2 = \sum_{\lambda_i}^{\lambda_f} [(O_\lambda - M_\lambda)\omega_\lambda]^2$, onde ω_λ representa o inverso do erro, e dos algorítmos SIMULATED ANNEALING e de METROPOLIS. Mais detalhes sobre o código podem ser encontrados em Cid Fernandes et al. (2005).

A *base de elementos* utilizada nesse trabalho é a base *GM* descrita em Cid Fernandes et al. (2013, 2014), que é construída utilizando os modelos de MILES (Vazdekis et al., 2016) e González Delgado et al. (2005). Utilizamos 21 idades (t= 0.001, 0.006, 0.010, 0.014, 0.020, 0.032, 0.056, 0.1, 0.2, 0.316, 0.398, 0.501 0.631, 0.708, 0.794, 0.891, 1.0, 2.0, 5.01, 8.91 e 12.6 Gyr) e quatro metalicidades (Z= 0.19, 0.40, 1.00 e 1.66 $Z_\odot$). Seguindo Cid Fernandes et al. (2004) adicionamos a base de elementos uma lei de potencia da forma $F_\nu \propto \nu^{-1.5}$ a fim de representar o contínuo do AGN. Finalmente, o fluxo de normalização, λ_0, foi o valor médio entre 5650 Å e 5750 Å. A lei de avermelhamento adotada foi a de Cardelli et al. (1989a) e a síntese foi feita para o intervalo 3700 Å $\leq \lambda \leq$ 6900 Å.

Capítulo 4

SOFTWARE URUTAU

Desenvolvemos um SOFTWARE, chamado URUTAU, com o propósito de facilitar o processamento e a organização dos resultados da síntese de populações estelares (capítulo 3). A proposta inicial de desenvolvimento do SOFTWARE consistia em tratar dos dados de entrada e saída do código STARLIGHT (seção 3.3), entretanto, durante o desenvolvimento, aumentou em escopo e complexidade.

Com a crescente demanda por processamento de dados – consequência do tamanho de amostras de estudo, técnicas modernas de observação (tais como IFS) e aprimoramentos nas resoluções espaciais e espectrais dos dados coletados – a necessidade de desenvolver e utilizar códigos automatizados é clara. Procuramos, então, desenvolver um SOFTWARE capaz de: produzir resultados a partir de um número indefinido de objetos da amostra, facilitar o desenvolvimento de aprimoramentos e modificações do fluxo de execução programa e facilitar o acesso à usuários com pouca compreensão de programação.

Os dois principais focos técnicos do desenvolvimento do URUTAU são versatilidade e velocidade de processamento. Para atingir esses objetivos, foram utilizadas técnicas de processamento paralelo e funcionalidade modular, descritos na seção 4.1. Os resultados científico produzidos para este trabalho foram gerados pelos módulos descritos na seção 4.3.

4.1 Programação Modular e Processamento Paralelo

Segue uma breve descrição dos conceitos de programação modular e processamento paralelos e suas vantagens no desenvolvimento e funcionalidade.

4.1.1 Programação Modular

A programação modular é um paradigma que propõe o desenvolvimento de aplicativos subdivididos em tarefas menores (módulos) que, por sua vez, podem ser facilmente substituídos ou aprimorados. As principais vantagens desse modelo de desenvolvimento se expressam de duas formas: facilidade de desenvolvimento para o programador e multifuncionalidade para o usuário.

A programação em módulos permite ao desenvolvedor se preocupar somente com o objetivo específico da parcela de código que está desenvolvendo, sem que precise pensar na origem dos dados de entrada e no destino dos dados de saída. Através de uma sintaxe específica criada para o URUTAU, cada módulo é tratado de maneira independente um do outro e a comunicação entre eles é definida pelo usuário através de um script de configuração.

A importância da multifuncionalidade em um SOFTWARE científico é nítida: trabalhos científicos contém amostras de origens distintas ou requerem métodos de análise de dados diferentes. Entretanto, nem todas as etapas de processamento de dados são dissemelhantes. A possibilidade de reutilizar porções de códigos (módulos) já desenvolvidos por outros programadores e a capacidade de adicionar outros módulos no processamento e produção de resultados é de suma importância no desenvolvimento científico coletivo. Essa facilidade de reutilizar módulos diminui o trabalho e o tempo gasto na construção de SOFTWARES já desenvolvidos.

O URUTAU emprega uma sintaxe específica para desenvolvimento de módulos, uma classe de objetos desenvolvida na linguagem Python, que será documentada no futuro.

4.1.2 Processamento Paralelo

Processamento paralelo já vem sendo usado à décadas em sistemas operacionais e programas que demandam grandes quantidades de processamento de dados e baixo tempo de resposta. Essa técnica utiliza o conceito básico de trabalho em equipe e divisão de tarefas – em termos técnicos, um programa é subdividido em tarefas específicas para serem processadas simultaneamente em diferentes núcleos de processamento de um computador. Com o URUTAU, cada dado de entrada inicial (cubo de dados) pode ser rodado em paralelo com outros dados conforme a necessidade. Utilizando uma sintaxe simples, o usuário pode escolher o número de dados a serem processados simultaneamente.

4.2 Pipeline do Urutau e Desenvolvimento de Módulos

Descrevemos nessa seção a estrutura e funcionamento do pipeline do URUTAU bem como a descrição de como desenvolver seus módulos.

4.2.1 Pipeline do URUTAU

O pipeline do URUTAU é composto de uma série de módulos que são executados em sequência. Cada módulo recebe como entrada um conjunto de extensões para arquivos FITS (HDUs – Header Data Units) contendo os dados relevantes para o processamento bem como um conjunto de parâmetros de configuração fornecidos pelo usuário. Durante o processamento, o módulo produz novas HDUs que, após o término da execução, é passado para o próximo módulo. Ao término da execução do último módulo, o pipeline gera um arquivo FITS com todas as extensões produzidas durante o processo.

A execução do pipeline do URUTAU é simples. O usuário fornece uma lista de módulos, na ordem a serem executados, uma lista de dados de entrada (no formato FITS) e um conjunto de parâmetros. Os parâmetros podem ser gerais (válidos para quaisquer módulos e/ou dados de entrada) ou específicos (para módulos e/ou cubos de dados individuais). Depois da configuração, basta que o usuário inicie o programa. Múltiplos dados de entrada podem ser processados simultaneamente e em sequência pelo pipeline conforme a necessidade do usuário. A figura 4.1 mostra o diagrama simplificado do processo.

Para que o programa possa processar diferentes dados de entradas com diferentes configurações de modo eficiente e automatizado, o usuário precisa fornecer uma série de dados de configurações. Para isso, foram desenvolvidos diversos métodos de entrada de parâmetros. Cada método possui um diferente escopo e prioridade durante a execução (Figura 4.2). Essa estrutura permite, por exemplo, que o usuário especifique configurações gerais de execução para todos os targets e, ao mesmo tempo, forneça configurações específicas pra um ou mais objetos.

Como exemplo, segue um script (4.1) demostrando a utilização e configuração do URUTAU com um conjunto de módulos (que foram utilizados nesse trabalho). O programa é compatível com arquivos CSV para a leitura de targets e seus parâmetros específicos (4.2). Os dados desse arquivo são utilizados por módulos que contenham parâmetros de configurações com os mesmos nomes das colunas.

```python
from urutau import Urutau
from urutau.filters_ur import ButterworthFilter
```

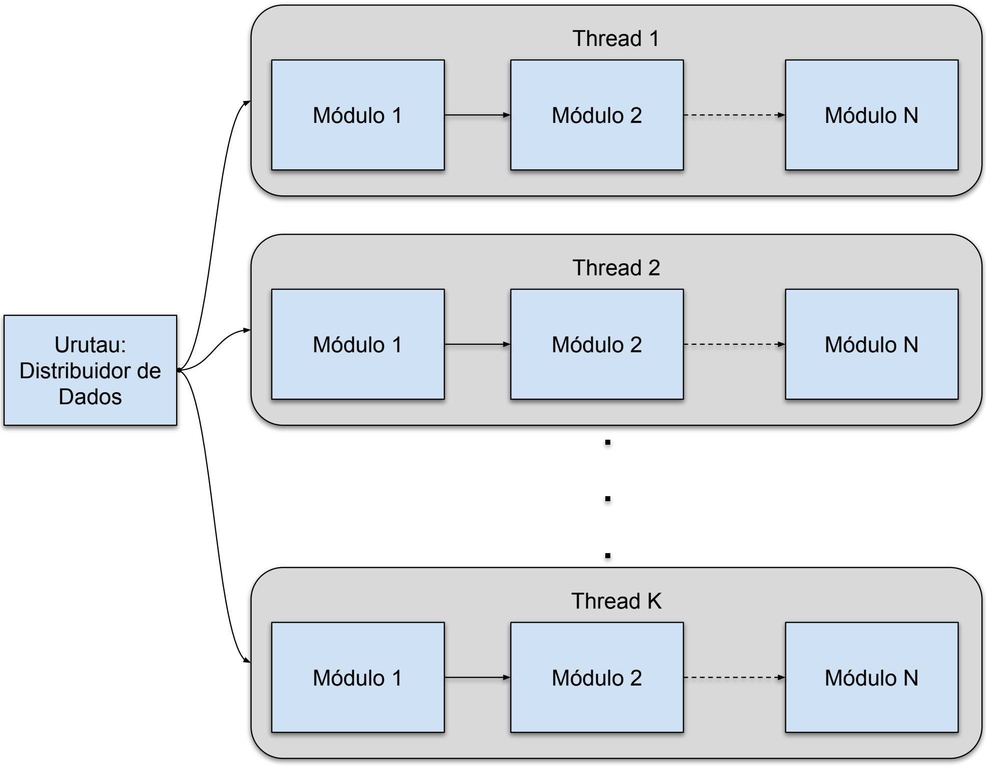

Figura 4.1: Urutau é responsável por distribuir os dados (i.e., arquivos FITS de entrada) aos threads criados pelo programa. Os threads rodam em paralelo e processam dados de entradas utilizando o pipeline (sequência de módulos configurada pelo usuário). O resultado de cada execução do pipeline é um arquivo FITS contendo os dados processados por cada módulo (ou somente pelo último módulo, conforme a escolha do usuário).

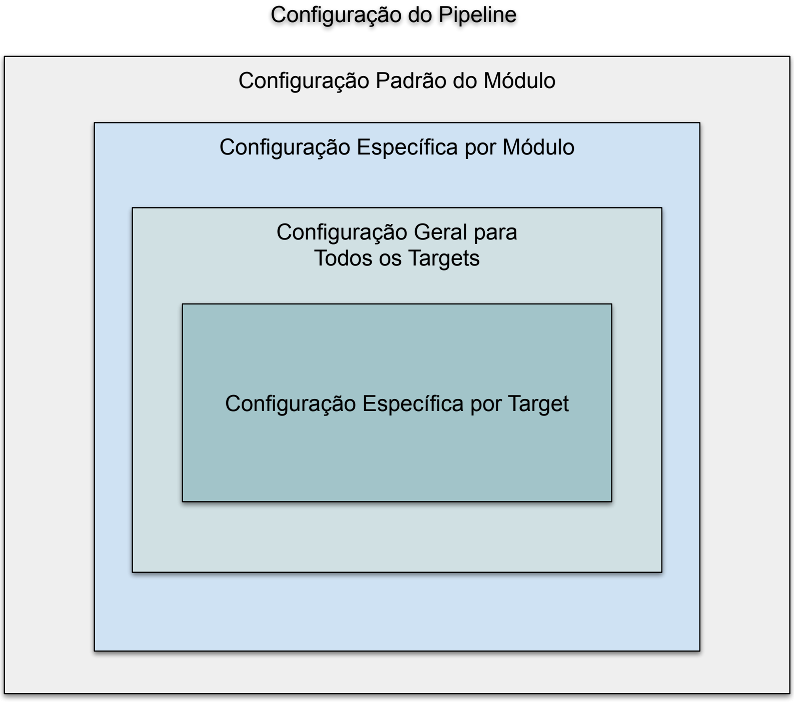

Figura 4.2: A prioridade dos dados de configuração cresce a medida que o escopo diminui (por exemplo, componente mais interno do diagrama possui maior prioridade).

```python
from urutau.dereddening_ur import CcmLaw
from urutau.starlight_ur import StarlightOnUrutau

# Create Urutau Object
urutau = Urutau()
urutau.set_number_of_threads(1)

# Load modules
modules = [ButterworthFilter, CcmLaw, StarlightOnUrutau]
urutau.set_modules(modules)

# Configure individual modules
butter_cfg = {"hdu flux": "FLUX"}
urutau.config_module(ButterworthFilter, butter_cfg)

ccm_cfg = {"hdu flux": "FLUX_BW"}
urutau.config_module(CcmLaw, ccm_cfg)

starlight_cfg = {
    "hdu flux": "FLUX_DRD",
    "starlight path": "./starlight/StarlightChains.exe",
    "default grid file": "./starlight/reference_grid.in",
    "root dir": "./synth_results/"
}
urutau.config_module(StarlightOnUrutau, starlight_cfg)

# Load targets
urutau.read_csv(targets_dir="./test_data/",
                csv_file="targets_data.csv")

# Execute urutau
urutau.execute("./urutau_results/", save_config=True, debug=True)
```

Listing 4.1: Utilizando o Urutau. Após o instanciamento do objeto Urutau, o usuário pode configurar o número de threads máximo, a sequência do pipeline, os targets.

```
target,galaxy distance,redshift
manga-9894-3701-LINCUBE.fits,96.662533975,0.0232843
```

Listing 4.2: Arquivo CSV com Targets e seus Parâmetros Específicos

4.2.2 Desenvolvimento de Módulos

Módulos podem ser facilmente desenvolvidos para serem integrados com o Urutau através do princípio de herança de classes. Desenvolvemos uma classe abstrata, chamada “UrutauModule”, que contém todas as funções necessárias para o URUTAU, com exceção de dois métodos que precisam ser implementados. Esses dois métodos são específicos de cada módulo e suas funções e requerimentos são descritos abaixo.

O método privado “_set_init_default_parameters” é responsável por inicializar os valores padrões de quaisquer variáveis usadas pelo modelo e não precisa retornar nenhum valor. Por exemplo, no módulo “ButterworthFilter”, inicializamos os parâmetros “hdu extension”, “order” e “range” com os valores “FLUX”, “3” e “0.3” respectivamente (ver código 4.3). O segundo método, chamado ”execute”, é responsável pelo processo principal do módulo e retorna, obrigatoriamente, dados processados no formato de um objeto “FitsHDU” (classe pertencente ao pacote “astropy.io.fits”).

Segue abaixo parte do código de “ButterworthFilter”, módulo usado nesse trabalho, para exemplificar o desenvolvimento de um módulo simples para o Urutau:

```python
import astropy.io.fits as fits
import numpy as np

from .urutau import UrutauModule

class ButterworthFilter(UrutauModule):
    """
        Module to apply a 2D butterworth along
        the z axis of a datacube HDU.
    """

    name = "Butterworth Filter"

    # Required Methods
    def _set_init_default_parameters(self) -> None:
        self.default_parameters["hdu extension"] = "FLUX"
        self.default_parameters["order"] = 3
        self.default_parameters["range"] = 0.3

    def execute(self, target_file: str) -> fits.FitsHDU:
        ext_name = self["hdu extension"]

        hdu_data = fits.getdata(target_file, ext_name)
        hdu_header = fits.getheader(target_file, ext_name)
```

```
25
26         bw_data = self._filter(flux_data=hdu_data,
27                                bw_order=self._config["order"],
28                                bw_range=self._config["range"])
29
30         hdu = fits.ImageHDU(data=bw_data, header=hdu_header)
31         hdu.header["EXTNAME"] = "FLUX_BW"
32         hdu.header["ORDER"] = self["order"]
33         hdu.header["RANGE"] = self["range"]
34
35         return hdu
36
37     # Custom methods
38     def _filter(...) -> np.ndarray:
39         ...
40
41     def _get_radial_matrix(...) -> np.ndarray:
42         ...
```

Listing 4.3: Módulo ButterworthFilter

O módulo herda as propriedades e métodos da classe “UrutauModule” conforme a linha 6. Para que possa ser usada pelo URUTAU, criamos os dois métodos necessários (iniciados nas linhas 15 e 20). Os métodos seguintes (a partir da linha 38) foram criados para auxiliar e organizar o código executado no método principal (“execute”) e seus códigos foram removidos para simplificar o exemplo.

4.3 Encapsulamento do STARLIGHT e outros Módulos Desenvolvidos

Foram desenvolvidos alguns módulos para o URUTAU utilizados neste trabalho. O módulo principal desse trabalho consiste no encapsulamento do programa STARLIGHT enquanto que os outros são utilizados pra preparar os dados para extração.

4.3.1 Módulos para Preparo de Dados

Diversos módulos foram usado para preparar as informações de um cubo de dados. Descrevemos os principais

Antes de extrair os espectros de cada *spaxel* dos cubos de dados, utilizamos um filtro bidimensional chamado Butterworth. Esse filtro utiliza transformadas de

Fourier nas imagens das galáxias, em cada comprimento de onda, para obter mapas no espaço de frequências. Utilizando um limite de corte nas altas frequências, o filtro remove linhas espúrias do espectro – nesse caso, pontos na imagem da galáxia cujo valor seja muito alto, ou muito baixo, frente ao valor dos vizinhos e valores médios nas imagens. Após o corte, o filtro aplica uma transformada reversa pra retomar a imagem com a remoção de pontos espúrios. Os pontos removidos são substituídos por um valor suavizado, condizente com os pontos adjacentes. Essa etapa é importante para aumentar a razão sinal ruído dos *spaxels*, permitindo o tratamento de dados mais confiável. Para uma descrição mais detalhada do filtro ver Riffel et al. (2016).

Após essa etapa, utilizamos os mapas de extinção de Schlegel (Schlegel et al., 1998), aplicando a lei de avermelhamento de CCM (Cardelli et al., 1989b), para remover o avermelhamento Galático introduzido em cada espectro integrado da galáxia. Outro fator de correção considerado foi o tratamento do deslocamento do espectro por efeito doppler (*redshift*).

O último passo desse módulo exclui espectros com baixa razão sinal-ruído (RSR), calculado na janela espectral desejada. Conforme Cid Fernandes et al. (2004), um RSR menor que 20 começa a afetar a confiança nos resultados da síntese. Inicialmente, utilizamos esse limite de corte, mas o número de espectros excluídos era alto demais para qualquer tipo de análise (algumas vezes, excluindo a galáxia inteira) e, para garantir um quantidade significativa de pontos, nos comprometemos com um corte de $RSR = 10$.

4.3.2 Módulo: Encapsulamento do STARLIGHT

Para que o programa possa utilizar o código de síntese de populações estelares, STARLIGHT, criamos um módulo que encapsula a chamada do programa executável. Esse encapsulamento é dividido em cinco etapas: extração dos espectros de um cubo de dados, criação de arquivos de configuração, execução do software encapsulado, montagem de um cubo de dados com os resultados da síntese e limpeza de dados temporários.

A primeira etapa do módulo extrai os dados de um cubo de dados (conforme especificações do usuário) para gerar arquivos texto (ASCII) contendo os espectros de luz de cada *spaxel*. O caminho de cada arquivo ASCII gerado é mantido em uma matriz bidimensional para que o cubo final, com os resultados da síntese, possa ser montado conforme o formato do cubo original. A segunda etapa utiliza a lista de arquivos e parâmetros escolhidos pelo usuário para gerar o arquivo de configuração do STARLIGHT, responsável por coordenar os caminhos dos dados e parâmetros principais durante a execução do programa.

A terceira etapa consiste em rodar o programa encapsulado com os dados extraídos. Essa etapa também é responsável verificar os dados gerados pelo STARLIGHT, excluindo quaisquer arquivos cuja síntese tenha falhado. Para mais detalhes de como o STARLIGHT funciona, ver seção 3.3 ou Cid Fernandes et al. (2004).

A quarta etapa faz a leitura dos dados gerados pelo STARLIGHT e gera um cubo de dados com os resultados. Esse cubo de dados contém diversos elementos, dentre eles: mapas de propriedades e sinal ruído, espectros utilizados e sintetizados e lista de SSPs. Após a montagem do cubo com os resultados, a quinta etapa (opcional) remove todos os arquivos temporários gerados durante a execução do módulo: espectros extraídos, arquivo de configuração e dados de saída do STARLIGHT.

Capítulo 5

Métodos de Análise do cubos de dados

Utilizamos os cubos de dados produzidos pelo URUTAU para fazer a análise da amostra e gerar as figuras descritas nesse capítulo.

5.1 Comparação das AGNs e suas Controles: Trio de Galáxias

Para cada trio de galáxias, AGN e suas respectivas galáxias de controles, foi gerado um painel mostrando as propriedades mais relevantes para o trabalho: imagem da galáxia, mapas RGB e de propriedades, perfis radiais e seus gradientes. A figura 5.1 exemplifica uma dessas imagens, cujos elementos descrevemos abaixo.

5.1.1 Imagens SDSS e Mapas RGB

Colocamos na figura as imagens obtidas do catálogo do SDSS mostrando o campo de observação do MaNGA e mapas RGB (*red*, *green* & *blue*) que geramos para retratar, de forma visual e qualitativa, a distribuição de idades das galáxias da nossa amostra. Cada cor representa um agrupamento de idades para as populações estelares – vermelho para populações velhas, verde para populações de idade intermediária e azul para populações jovens.

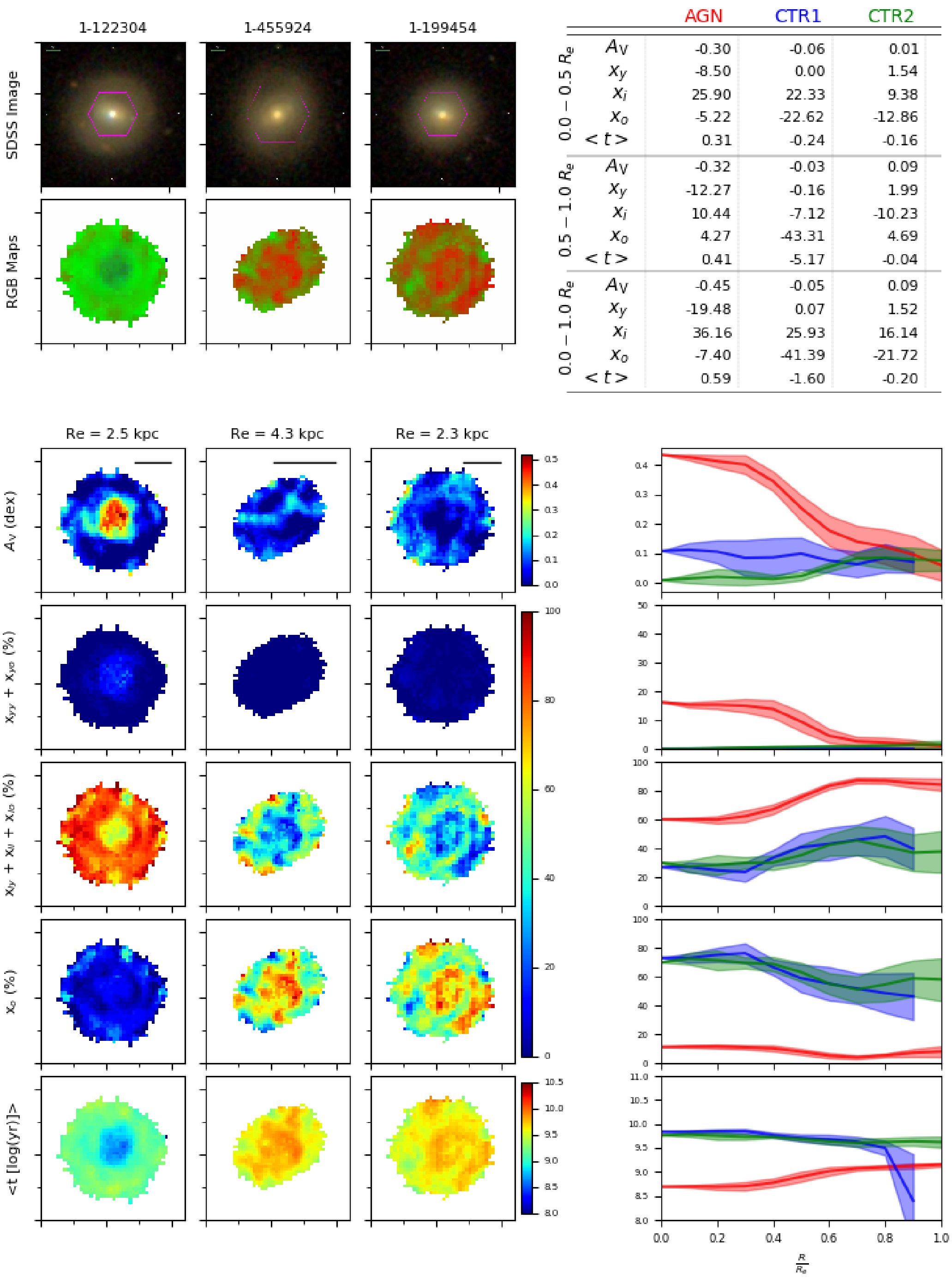

		AGN	CTR1	CTR2
$0.0-0.5\ R_e$	A_V	-0.30	-0.06	0.01
	x_y	-8.50	0.00	1.54
	x_i	25.90	22.33	9.38
	x_o	-5.22	-22.62	-12.86
	$<t>$	0.31	-0.24	-0.16
$0.5-1.0\ R_e$	A_V	-0.32	-0.03	0.09
	x_y	-12.27	-0.16	1.99
	x_i	10.44	-7.12	-10.23
	x_o	4.27	-43.31	4.69
	$<t>$	0.41	-5.17	-0.04
$0.0-1.0\ R_e$	A_V	-0.45	-0.05	0.09
	x_y	-19.48	0.07	1.52
	x_i	36.16	25.93	16.14
	x_o	-7.40	-41.39	-21.72
	$<t>$	0.59	-1.60	-0.20

Figura 5.1: Figura comparando AGN (coluna da esquerda e perfis de cor vermelha) com as sua dupla de galáxias de controle (colunas 2 e 3 e cores azul e verde dos perfis respectivamente). DESCREVER AS PARTES.

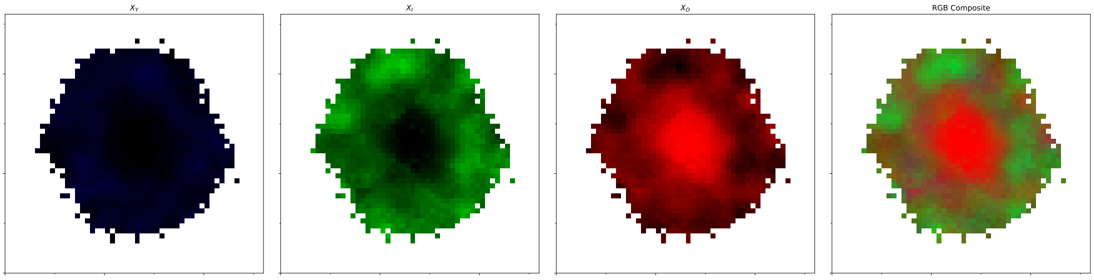

Figura 5.2: Cada cor representa populações com um intervalo de idades específico. Azul são jovens ($\mathrm{X_Y}$: t $\leq$ 40 Myr); verdes são de idade intermediária ($\mathrm{X_I}$: 40 $\leq$ 2.5 Gyr); vermelhas são velhas ($\mathrm{X_O}$: $t > 2.5\,Gyr$). A composição dos três mapas forma a imagem RGB (à direita), que representa de forma qualitativa as três populações.

5.1.2 Mapas de Populações

Agrupamos a contribuição luminosa de populações estelares em 3 grupos conforme a idade: populações jovens ($\mathrm{X_Y}$: t $\leq$ 40 Myr), populações de idade intermediária ($\mathrm{X_I}$: 40 $\leq$ 2.5 Gyr) e populações velhas ($\mathrm{X_O}$: $t > 2.5\,Gyr$). A razão por trás dessa classificação é devida à sensibilidade da síntese de populações estelares à pequenos desvios e incertezas durante o processamento, resultando em pequenas flutuações nas contribuições de populações estelares de idades ou metalicidades próximas umas das outras (Cid Fernandes et al., 2005).

Esses mapas são centrais a este trabalho e é deles que derivamos os perfis radiais utilizados para comparar a produção estelar em galáxias com e sem núcleos ativos.

5.1.3 Perfis Radiais Deprojetados e Gradientes

Para cada mapa de propriedades gerado, geramos perfis radiais médios (em raio efetivo, incluindo seus gradientes), utilizando a seguinte fórmula (aplicada pra cada ponto da galáxia):

$$P(R_{eff}) = K\sqrt{cos(\theta)^2 + \left(\frac{Asin(\theta)}{B}\right)^2} \tag{5.1}$$

onde K é um escalar para converter o perfil de unidades de pixel para unidades de R_{eff}, A e B são os semi-eixos (maior e menor) da galáxia, θ é o ângulo entre o semi-eixo maior e o eixo horizontal da imagem. Esse cálculo assume simetria circular na deprojeção.

Com os perfis radiais, geramos valores de gradientes para três intervalos de

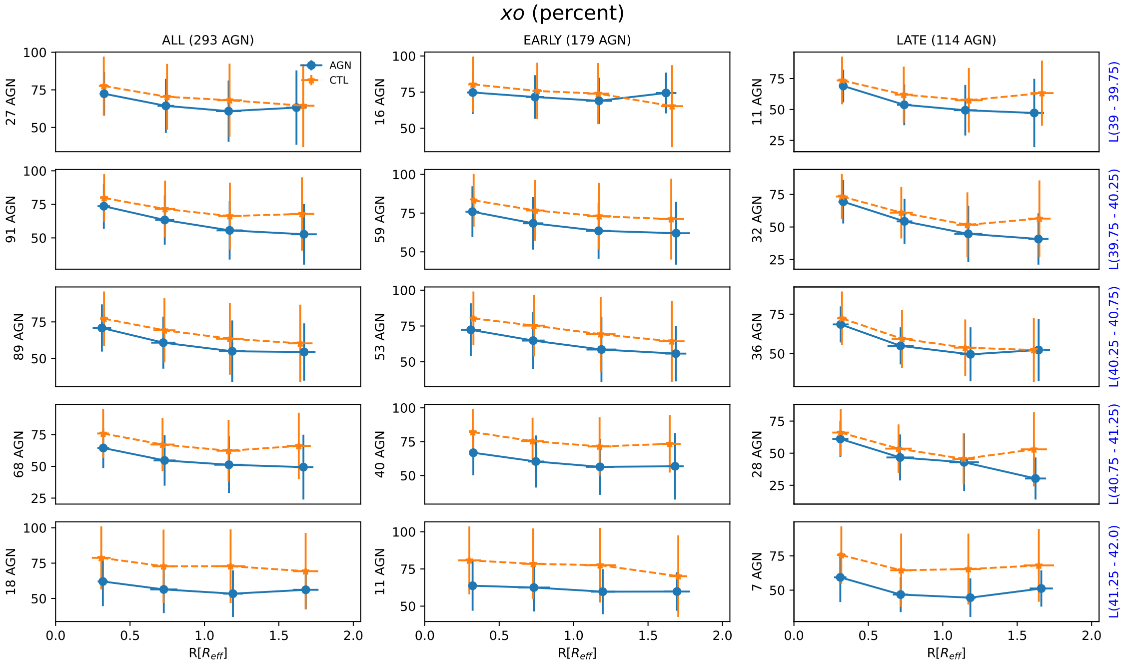

Figura 5.3: Série de perfis médios comparando AGNs com suas respectivas galáxias de controles. Linhas representam intervalos de luminosidade do O III(valores à direita da figura) e colunas representam os tipos morfológicos ("all", "early" e "late" respectivamente). Cada perfil representa a média dos valores radiais de todas as AGNs (com suas respectivas galáxias de controle) contidas dentro da classificação morfológica e do intervalo de luminosidade indicado.

distância: 0.0 a $0.5\,R_{eff}$, 0.5 a $1.0\,R_{eff}$ e 0.0 a $1.0\,R_{eff}$. Para tal, assumimos linearidade e aplicamos regressão linear pra cada um dos intervalos definidos.

Exemplos de perfis e gradientes se encontram a direita da figura 5.1 para os mapas de avermelhamento, populações estelares e idade média.

5.2 Perfis Médios em Função da Luminosidade do AGN

A luminosidade no [O III] ($L_{[\text{O III}]}$) é um forte indicativo de atividade nuclear. É por esse motivo que agrupamos a amostra de AGNs desse trabalho conforme a luminosidade em [O III] λ5007. Para cada grupo, geramos perfis médios das propriedades estudadas – incluindo as diferenças entre perfis de AGNs e suas respectivas galáxias de controle. Esse estudo também inclui a análise conforme o tipo morfológico das galáxias: precoces (*early-type*) e tardias (*late-type*). A figura 5.3 mostra o resultado para as populações velhas da nossa amostra.

Capítulo 6

Medindo a Taxa Formação estelar em Galáxias ativas usando síntese de população estelar

Neste capítulo apresento uma análise comparando as taxas de formação estelar nos spaxels classificados via BPT como dominados por formação estelar derivadas via linhas de recombinação do hidrogênio e via ajuste da população estelar. Os resultados formam publicados na revista Monthly Notices of the Royal Astronomical Society, Volume 501, Issue 3, pp.4064-4079 em 2021.

MNRAS **000**, 1–13 (2020) Preprint 16 December 2020 Compiled using MNRAS LATEX style file v3.0

Determining star-formation rates in Active Galactic Nuclei hosts via stellar population synthesis

Rogério Riffel[1,2★], Nicolas D. Mallmann[1,2], Gabriele S. Ilha[2,3], Thaisa Storchi-Bergmann[1,2],
Rogemar A. Riffel[2,3], Sandro B. Rembold[2,3], Dmitry Bizyaev[4,5], Janaina C. do Nascimento[1,2],
Jaderson S. Schimoia[2,3], Luiz N. da Costa,[2,6] Nicholas Fraser Boardman [7],
Médéric Boquien[8], Guilherme S. Couto[8],
[1] *Departamento de Astronomia, Instituto de Física, Universidade Federal do Rio Grande do Sul, CP 15051, 91501-970, Porto Alegre, RS, Brazil*
[2] *Laboratório Interinstitucional de e-Astronomia - LIneA, Rua Gal. José Cristino 77, Rio de Janeiro, RJ - 20921-400, Brazil*
[3] *Departamento de Física, Centro de Ciências Naturais e Exatas, Universidade Federal de Santa Maria, 97105-900, Santa Maria, RS, Brazil*
[4] *Apache Point Observatory and New Mexico State University, P.O. Box 59, Sunspot, NM, 88349-0059, USA*
[5] *Sternberg Astronomical Institute, Moscow State University, Moscow, Russia*
[6] *Observatório Nacional - MCT, Rua General José Cristino 77, Rio de Janeiro, RJ - 20921-400, Brazil*
[7] *Department of Physics & Astronomy, University of Utah, Salt Lake City, UT, 84112, USA*
[8] *Centro de Astronomía (CITEVA), Universidad de Antofagasta, Avenida Angamos 601, Antofagasta, Chile.*

Accepted XXX. Received YYY; in original form ZZZ

ABSTRACT

The effect of active galactic nuclei (AGN) feedback on the host galaxy, and its role in quenching or enhancing star-formation, is still uncertain due to the fact that usual star-formation rate (SFR) indicators – emission-line luminosities based on the assumption of photoionisation by young stars – cannot be used for active galaxies as the ionising source is the AGN. We thus investigate the use of SFR derived from the stellar population and its relation with that derived from the gas for a sample of 170 AGN hosts and a matched control sample of 291 galaxies. We compare the values of SFR densities obtained via the Hα emission line ($\Sigma\mathrm{SFR_{Gas}}$) for regions ionised by hot stars according to diagnostic diagrams with those obtained from stellar population synthesis ($\Sigma\mathrm{SFR}_\star$) over the last 1 to 100 Myr. We find that the $\Sigma\mathrm{SFR}_\star$over the last 20 Myrs closely reproduces the $\Sigma\mathrm{SFR_{Gas}}$, although a better match is obtained via the transformation: $\log(\Sigma\mathrm{SFR}_\star) = (0.872 \pm 0.004)\log(\Sigma\mathrm{SFR_{Gas}}) - (0.075 \pm 0.006)$ (or $\log(\Sigma\mathrm{SFR_{Gas}}) = (1.147 \pm 0.005)\log(\Sigma\mathrm{SFR}_\star) + (0.086 \pm 0.080)$), which is valid for both AGN hosts and non-active galaxies. We also compare the reddening obtained via the gas Hα/Hβ ratio with that derived via the full spectral fitting in the stellar population synthesis. We find that the ratio between the gas and stellar extinction is in the range $2.64 \leq A_{V\,g}/A_{V\star} \leq 2.85$, in approximate agreement with previous results from the literature, obtained for smaller samples. We interpret the difference as being due to the fact that the reddening of the stars is dominated by that affecting the less obscured underlying older population, while the reddening of the gas is larger as it is associated to a younger stellar population buried deeper in the dust.

Key words: galaxies: active – galaxies: evolution – galaxies: ISM – galaxies: star formation –galaxies: stellar content

1 INTRODUCTION

Present day galaxies display a wide range of luminosities, sizes, stellar population properties, structure, kinematics, and gas content, being the endpoint of a ~13.8 Gyr long process (Aghanim et al. 2020). These properties have been shaped by a series of processes, and, according to them, galaxies can roughly be divided in passive and star-forming. The passive galaxies are not actively forming stars and host a red and old stellar population, while the star-forming galaxies are blue, hosting large fractions of young stellar populations. Such bi-modal behaviour is observed even at high redshifts ($z > 2.5$) where populations of passive galaxies are observed (e.g. Muzzin et al. 2013; Brammer et al. 2009).

The bi-modality of galaxies has been verified in a number of studies over the years (e.g. Baldry et al. 2004; Wetzel et al. 2012; Kauffmann et al. 2003a; Noeske et al. 2007; van der Wel et al. 2014). However, it is not yet clear which mechanisms are driving the shutting down of star formation and transforming the blue star-forming spiral galaxies into *red-and-dead* galaxies. A major challenge in modern astrophysics is to determine the nature of the physical mechanism quenching star formation in galaxies.

One mechanism that has been invoked by a number of studies is the feedback of active galactic nuclei (AGN). AGN feedback can quench star formation by heating and/or (re)moving the gas. AGN outflows are often considered as negative feedback processes that suppress star-formation (e.g. Granato et al. 2004; Fabian 2012; King & Pounds 2015; Zubovas & Bourne 2017; Trussler et al. 2020, and references therein). On the other hand, some models and simulations

---

★ E-mail: riffel@ufrgs.br

suggest that these outflows and jets can in some cases compress the galactic gas, and therefore act as a catalyzer and boosting the star-formation (e.g. Rees 1989; Hopkins 2012; Nayakshin & Zubovas 2012; Bieri et al. 2016; Zubovas et al. 2013; Zubovas & Bourne 2017) and even form stars inside the outflow (e.g. Ishibashi & Fabian 2012; Zubovas et al. 2013; El-Badry et al. 2016; Wang & Loeb 2018, for an observational example see Gallagher et al. (2019), and references therein).

Cosmological simulations (e.g. Springel et al. 2005; Vogelsberger et al. 2014; Crain et al. 2015) performed without the inclusion of feedback effects are not able to reproduce the galaxy luminosity function (at both the low and high-luminosity ends), and also underestimate the ages of the most massive galaxies (see Figs. 8 and 10 of Croton et al. 2006). It thus seems that effective feedback is required to reproduce the galaxy properties, but simulations can only provide limited insight into the nature and source of the feedback processes (e.g. AGN or SN dominated Schaye et al. 2015). This is because there are still not enough observational constraints on these processes, and in particular, in the case of AGN, in order to verify how quenched is the star formation it is necessary to robustly quantify the star formation rates (SFR) of the hosts in the vicinity of the AGN. Both AGN activity and star-formation (SF) are regulated by the amount of available gas in the host galaxy. The relation between the gas and SF is relatively well-characterised by previous studies (e.g. Kennicutt & Evans 2012; Barrera-Ballesteros et al. 2020; Lin et al. 2019; Zhuang & Ho 2020). Simulations should be able to correctly reproduce the observed SF; this, however, will depend on the efficiency of feedback processes in the interstellar medium (ISM). But resolving such processes is not yet possible in simulations of cosmological volumes (Schaye et al. 2015). In addition, in current models, the feedback processes are included in an *ad-hoc* manner (Weinberger et al. 2017; Nelson et al. 2019), being activated by a threshold luminosity.

While there are many calibrators to determine the SFR for non-active galaxies (for a review see Kennicutt 1998; Kennicutt & Evans 2012), in the case of AGN this is a very difficult task, since the emitting gas is ionised by the AGN radiation. Therefore, SFR indicators and equations calibrated with stellar photoionization prescriptions can not be used in this context. Efforts have been made using far infrared luminosities as star formation indicators (e.g. Kennicutt et al. 2009; Rosario et al. 2013, 2016, 2018, and references therein) or mid-infrared neon ([Ne II] 12.81μm and [Ne III] 15.56μm) emission lines (Zhuang et al. 2019). The infrared observations used in these works are obtained using large apertures, including the whole galaxy emission. As discussed in Rosario et al. (2016) despite finding a good correlation between Far-infrared emission and SFR (which can be attributed to leaking of the SF regions to the whole galaxy or that the SF is constant over several hundreds of Myr) a substantial component of the cold dust luminosity that is associated with a diffuse interstellar radiation field can come from evolved stars. Even if the contribution from an old age stellar population is not dominant, the far-infrared may not be a good tracer of SF since dust can be heated by stars that are older than a few hundred Myr (Kennicutt et al. 2009; Hao et al. 2011; Rosario et al. 2016). Other recent effort on the bluer part of the spectrum has been made using a re-calibration [O II] λ3727 emission line (Zhuang et al. 2020, 2019), which is metallicity and electron density dependent.

From the above it is clear that it is thus necessary to find an independent way to obtain SFRs in AGN hosts. A powerful technique to disentangle the components summing up to a galaxy spectral energy distribution (SED) is stellar populations synthesis (e.g. Cid Fernandes et al. 2004, 2005; Riffel et al. 2009, 2008; Walcher et al. 2011; Cid Fernandes 2018; Baldwin et al. 2018; Salim et al. 2018; Peterken et al. 2020, and references therein). The synthesis is based on the simultaneous fit of different proportions of composite or simple stellar populations (SSPs) templates from a base of such spectra to the observed spectrum. In the case of the STARLIGHT fitting code (Cid Fernandes et al. 2004, 2005; Cid Fernandes 2018), it returns the values of the gas mass rate that has been converted into stars throughout the galaxy life as well as this rate for each single SSP included in the base. These values can, therefore, be used to compute the SFR via stellar population synthesis, SFR$_\star$. In fact, this was already applied in Asari et al. (2007) using single fiber Sloan Digital Sky Survey (SDSS) data and older stellar population models generations (they used Bruzual & Charlot 2003, models).

From the discussion above it is clear that it is of utmost importance to characterise the SFR of AGN hosts – in particular in the narrow-line region (NLR) and extended narrow-line region (ENLR), that are photoionised by the AGN. And in order to verify the actual role of the AGN on the SFR it is necessary to compare the SFR values obtained for the NLR and ENLR with those obtained for a matched control sample of non-active galaxies at similar distances from the nucleus, as well as with predictions from simulations. In Rembold et al. (2017) we described the method we have used to select our sample of AGN and a matched control galaxy sample from the Mapping Nearby Galaxies at APO (MaNGA, Bundy et al. 2015) survey. Here, we have used an updated sample of 170 AGN and 291 controls (Deconto-Machado, *in preparation*), selected as in Rembold et al. (2017) to compute SFR indicators from the gas – using diagnostic diagrams to separate gas ionised by AGN and by hot stars – and from the stellar population synthesis and investigate the relation between them. We propose equations to relate the SFR densities obtained via emission lines, $\Sigma\mathrm{SFR}_{\mathrm{Gas}}$ with that obtained via stellar population synthesis, $\Sigma\mathrm{SFR}_\star$, allowing to obtain one from the other.

This paper is structured as follows: in section 2 we present the updated samples. The methods used to determine the SFR are described in section 3. The results are presented and discussed in section 4 and conclusions are made in section 5. We have used throughout the paper $H_0 = 67.7\,\mathrm{km\,s^{-1}\,Mpc^{-1}}$, $\Omega_m = 0.31$ Aghanim et al. (2020).

2 DATA

The data used here were obtained from the Mapping Nearby Galaxies at Apache Point Observatory (MaNGA) survey (Bundy et al. 2015). MaNGA is part of the fourth generation Sloan Digital Sky Survey (SDSS IV). The survey has provided optical spectroscopy (3600 Å-10400 Å) of $\sim$ 10,000 nearby galaxies (with $\langle z\rangle \approx 0.03$). The observations were carried out with fiber bundles of different sizes (19-127 fibers) covering a field of 12″ to 32″ in diameter. MaNGA observations are divided into "primary" and "secondary" targets, the former are observed up to 1.5 effective radius (R_e) while the latter is observed up to 2.5 R_e. For more details, see Drory et al. (2015); Law et al. (2015); Yan et al. (2016a,b).

The sample used in this work is an update of our previous MaNGA AGN hosts and matched non-active control galaxies (Rembold et al. 2017). The control sample was selected in order to match the AGN hosts in terms of stellar mass, redshift, visual morphology and inclination (for details see Rembold et al. 2017). After the release of the MaNGA Product Launch 8 (MPL-8, Aguado et al. 2019; Blanton et al. 2017; Bundy et al. 2015; Belfiore et al. 2019; Westfall et al. 2019; Cherinka et al. 2019; Wake et al. 2017; Law et al. 2015, 2016; Yan et al. 2016b,a; Drory et al. 2015; Gunn et al. 2006; Smee et al. 2013), the number of observed AGN with MaNGA has grown to

170 AGNs using the same criteria as in Rembold et al. (2017). For each AGN, we have also selected two control galaxies. Since more than one AGN host can share the same control galaxy, this inactive sample is composed by 291 sources. Both AGN and control samples are located in the redshift range $0.02 \lesssim z \lesssim 0.15$, and their typical stellar masses are of the order $10^{10.5} - 10^{11} M_\odot$. Most AGN in our sample (64%) are low-luminosity, presenting [O III] $\lambda5007$Å luminosities below 3.8×10^{40} erg s^{-1}.

Analysis of the morphological classification of galaxies in our sample with the Galaxy Zoo database (Lintott et al. 2008, 2011) reveals that our updated AGN sample contains 57 early-type (33.5 percent), 87 late-type (51.2 percent), 3 merger galaxies (1.8 percent), and 23 objects (13.5 percent) without classification. The control sample is composed of 125 early-type (36.8 percent), 182 late-type (53.5 percent), 4 merger galaxies (1.2 percent), and 29 objects (8.5 percent) whose classifications are uncertain. Regarding nuclear activity, 63.6 percent of the AGN host sample presents Seyfert nuclei, while the other 36.4 percent are Low-ionization nuclear emission-line region (LINER) sources. For more details on the updated sample properties see Deconto-Machado (*in preparation*).

For all galaxies in our sample, gas and stellar population parameters have been derived from the MaNGA IFU optical spectra datacubes. We refer to Bundy et al. (2015) for details on the MaNGA spectroscopic data, like spectral resolution, spatial coverage and pixel scale.

3 STAR-FORMATION RATES

We have obtained the star-formation rate surface densities for the gas $\Sigma\mathrm{SFR}_{\mathrm{Gas}}$ and for the stars $\Sigma\mathrm{SFR}_\star$ for each spaxel of the datacubes dividing the corresponding SFR values in units of solar masses per year ($M_\odot$ yr^{-1}) by the area of each spaxel in kpc^2.

Our goal is to compare SFR values obtained from the gas emission lines to those obtained from stellar population synthesis. As the prescriptions for the gas are based on the assumption that it is photoionised by young, hot stars, this comparison needs to be done only for spaxels in which the gas is indeed ionised by stars. We have thus used optical diagnostic diagrams (see § 3.1) to isolate the spaxels whose emission is produced by photoionisation by the radiation of young stars.

We also need to be sure that the signal-to-noise ratio of the data from each spaxel is high enough to allow reliable measurements. In summary, in order to ensure that the measurements are accurate, we have subjected the results obtained for each spaxel to the validation criteria listed below.

3.1 Spaxels validation

We considered results from a spaxel to be valid only if they match the following criteria:

- The mean value of the signal-to-noise ratio (SNR) in the continuum window between 5650Å and 5750Å is ≥ 10. This was applied in order to ensure that the stellar population fits are reliable (Cid Fernandes et al. 2004, 2005; Riffel et al. 2009);
- The Hα Equivalent width (EW) is larger than 10 Å and the Hβ EW is larger than 3 Å. This is necessary in order to avoid spaxels that could have large contribution from other ionising sources such as post-AGB stars;
- The following relation between line ratios is obeyed: $\log([\mathrm{O\,III}]\lambda5007/\mathrm{H}\beta) < 0.61/(\log([\mathrm{N\,II}]\lambda6583/\mathrm{H}\alpha) - 0.05) + 1.3$ (Kauffmann et al. 2003b). This is based on diagnostic diagrams to ensure that only star-forming emission spaxels are being used in the calculation of the SFR.

By using these selection criteria we make sure that we are only using results obtained for spaxels that have a good stellar population fit and the gas is photoionised by hot young stars.

3.2 SFR from stellar population synthesis

Our first step was to perform a full spectral fitting stellar population synthesis on our datacubes. We used the STARLIGHT fitting code (Cid Fernandes et al. 2005; Cid Fernandes 2018) which combines the spectra of a base of $N_\star$ simple stellar population (SSP) template spectra $b_{j,\lambda}$, in different proportions, in order to reproduce the observed spectrum O_λ. For this comparison the modelled spectra M_λ are normalised at an user defined wavelength (λ_0). The reddening is given by the term $r_\lambda = 10^{-0.4(A_\lambda - A_{\lambda_0})}$, weighted by the population vector x_j (which represents the fractional contribution of the jth SSP to the light at the normalisation wavelength λ_0), and convolved with a Gaussian distribution $G(v_\star, \sigma_\star)$ to account for velocity shifts $v_\star$, and velocity dispersion $\sigma_\star$.

Each model spectrum can be expressed as:

$$M_\lambda = M_{\lambda_0}\left[\sum_{n=1}^{N_\star} x_j\, b_{j,\lambda}\, r_\lambda\right] \otimes G(v_\star, \sigma_\star), \qquad (1)$$

where M_{λ_0} is the flux of the synthetic spectrum at the wavelength λ_0. To find the best parameters for the fit, the code searches for the minimum of $\chi^2 = \sum_{\lambda_i}^{\lambda_f} [(O_\lambda - M_\lambda)\omega_\lambda]^2$, where ω_λ is the inverse of the error, using a simulated annealing plus Metropolis scheme. We normalised our data at λ_0, adopted to be the mean value between 5650Å and 5750Å. The reddening law we have used was that of Cardelli et al. (1989) and the synthesis was performed for the spectral range from 3700 Å to 6900 Å.

The SSPs base set we use is the *GM* described in Cid Fernandes et al. (2013, 2014) that is constructed using the MILES (Vazdekis et al. 2010) and González Delgado et al. (2005) models. We have updated it with the MILES V11 models (Vazdekis et al. 2016). We used 21 ages (t= 0.001, 0.006, 0.010, 0.014, 0.020, 0.032, 0.056, 0.1, 0.2, 0.316, 0.398, 0.501 0.631, 0.708, 0.794, 0.891, 1.0, 2.0, 5.01, 8.91 and 12.6 Gyr) and four metallicities (Z= 0.19, 0.40, 1.00 and 1.66 Z$_\odot$). We have also added to the specgral base a power law of the form $F_\nu \propto \nu^{-1.5}$ to account for the contribution of a possible AGN continuum (observed directly or as scattered light).

Since STARLIGHT is not prepared to handle with datacubes we have used our in house software MEGACUBE (Mallmann et al. 2018). This code wraps STARLIGHT to deal with its numerous input and output files involved with IFU data. Each spaxel requires an ASCII file and generates another one. For each galaxy, thousands of files are organised and extracted to a coherent data-cube to be subsequently analysed. The code can also be used for a multitude of functions since it was developed with modular capabilities, i.e., parts of the software can be changed, swapped or removed depending on the scientific goals. Besides allowing us to easily prepare and fit the stellar populations in datacubes its modular approach allows to use MEGACUBE to generate maps for the direct and indirect STARLIGHT fitting products. See Mallmann et al. (2018) for further details.

One of the data products computed by MEGACUBE is the star formation rate obtained from the stellar fit ($SFR_\star$) over an user-defined age interval ($\Delta t = t_{j_f} - t_{j_i}$). This can be computed since the SSPs model spectra are in units of L$_\odot$ Å^{-1} $M_\odot^{-1}$, and the observed spectra (O_λ) are in units of erg/s/cm^2/Å (for details see the STARLIGHT manual[1]). The SFR$_\star$ over the chosen Δt can be computed assuming that the mass of each base component (j) which has been processed into stars can be obtained as:

$$M^{\rm ini}_{\star,j} = \mu^{\rm ini}_j \times \frac{4\pi d^2}{3.826\times 10^{33}}, \tag{2}$$

where $M^{\rm ini}_{\star,j}$ is given in $M_\odot$, $\mu^{\rm ini}_j$ represents the mass that has been converted into stars for the j-th element and its flux. This parameter is given in $M_\odot$ ergs^{-1}cm^{-2}; d is the distance to the galaxy in cm and 3.826×10^{33} is the Sun's luminosity in erg s^{-1}. Thus, the SFR over the Δt as defined above can be obtained from the equation:

$$\mathrm{SFR}_\star = \frac{\sum_{j_i}^{j_f} M^{\rm ini}_{\star,j}}{\Delta t}. \tag{3}$$

For more details, see the STARLIGHT manual[1], and for an application example see Asari et al. (2007); Riffel et al. (2020).

3.3 SFR from Hα emission-line fluxes

A very common approach to determine SFR from the gas emission (SFR$_{\rm Gas}$) is using hydrogen recombination emission-line fluxes (see, Kennicutt 1998; Kennicutt & Evans 2012, for a review). Therefore, we have used the MEGACUBE absorption free emission-line datacubes to fit the emission lines. This procedure was done using the IFSCUBE[2] tool: a python package designed to perform analysis tasks in data cubes. This code allows to fit emission lines with Gaussian functions (among other options), allowing to constraint kinematics and line fluxes ratios in a very robust and easy way (Ruschel-Dutra 2020).

We use the IFSCUBE Python package to fit the emission-line profiles of Hβ, [O III]$\lambda\lambda$4959,5007, He Iλ5876, [O I]λ6300, Hα [N II]$\lambda\lambda$6548,6583 and [S II]$\lambda\lambda$6716,6731. We fit the spectra after the subtraction of the underlying stellar population contribution derived in the previous section. The line profiles are fitted with Gaussian curves by adopting the following constraints: (i) the width and centroid velocities of emission lines from the same parent ion are tied; (ii) the [O III]λ5007/λ4959 and [N II]λ6583/λ6548 flux ratios are fixed to their theoretical values of 2.98 and 3.06, respectively; (iii) the centroid velocity is allowed to vary from –300 to 300 km s^{-1} for [S II] lines and –350 to 350 km s^{-1} for the other lines relative to the velocity obtained from the redshift of each galaxy (listed in the MaNGA Data Analysis Pipeline - DAP); and (iv) the observed velocity dispersion of all lines is limited to the range 40–300 km s^{-1}. In addition, we include a first order polynomial to reproduce the local continuum.

Since emission lines effectively re-emit the photons absorbed from the integrated stellar Lyman continuum, they provide a direct probe of the population of young, massive stars. Maps for the SFR$_{\rm Gas}$ were obtained with the following equation from Kennicutt (1998):

$$\mathrm{SFR}_{\rm Gas}(M_\odot/\mathrm{yr}) = 7.9\times10^{-42} L(\mathrm{H}\alpha)(\mathrm{ergs/s}), \tag{4}$$

were $L(\mathrm{H}\alpha)$ is the reddening corrected Hα luminosity.

3.4 Stellar population and nebular reddening

STARLIGHT models the reddening of the integrated stellar continuum as a foreground dust screen and it is parameterized by the extinction in the V-band, A_V using the reddening law of Cardelli et al. (CCM 1989).

The gas reddening was obtained considering Case B recombination at T$_{\rm e}$ = 10000 K (Kennicutt 1998), and the corresponding color excess $E(B-V)$ can be obtained as follows (see Calzetti et al. 2000; Domínguez et al. 2013):

$$\begin{aligned} E(B-V) &= \frac{E(\mathrm{H}\beta-\mathrm{H}\alpha)}{f_\lambda(\mathrm{H}\beta)-f_\lambda(\mathrm{H}\alpha)} && (5)\\ &= \frac{2.5}{R_\lambda\,(f_\lambda(\mathrm{H}\beta)-f_\lambda(\mathrm{H}\alpha))}\left[\frac{(F_{\mathrm{H}\alpha}/F_{\mathrm{H}\beta})^{obs}}{(F_{\mathrm{H}\alpha}/F_{\mathrm{H}\beta})^{int}}\right], && (6)\end{aligned}$$

where $f_\lambda(\mathrm{H}\alpha)$ and $f_\lambda(\mathrm{H}\beta)$ are the reddening curve values at the Hα and Hβ wavelengths, which for the CCM's reddening law are $f_\lambda(\mathrm{H}\alpha) = 0.818$ and $f_\lambda(\mathrm{H}_\beta) = 1.164$.

Adopting $R_\lambda = R_V = 3.1$ and the theoretical line ratio of $F_{H\alpha}/F_{H\beta} = 2.86$ for case B H I recombination for an electron temperature of T_e = 10 000 K and electron density of N_e = 100 cm^{-3} (Osterbrock & Ferland 2006), we obtain:

$$A_V = 7.22\,\log\left(\frac{(F_{\mathrm{H}\alpha}/F_{\mathrm{H}\beta})^{obs}}{2.86}\right). \tag{7}$$

The intrinsic flux ($F^\lambda_{\rm int}$) of an emission line is then related to the observed one ($F^\lambda_{\rm obs}$) by the following equation:

$$\begin{aligned} F^\lambda_{\rm int} &= F^\lambda_{\rm obs}\,10^{0.4A_\lambda} && (8)\\ &= F^\lambda_{\rm obs}\,10^{0.4R_\lambda E(B-V)}, && (9)\end{aligned}$$

where A_λ is the extinction at wavelength λ and R_λ is the extinction curve index from Cardelli et al. (1989). The equation above was used to correct the Hα emission-line flux used in the calculation of the Hα luminosity and SFR$_{Gas}$.

4 RESULTS AND DISCUSSION

4.1 Comparison between SFR_{Gas} and SFR_*

In order to compare the SFR values obtained for all galaxies that are at different distances, we have calculated the SFR surface densities ΣSFR$_\star$ and ΣSFR$_{\rm Gas}$ by dividing the obtained SFRs values for each spaxel by its area in kpc^2. The resulting values are in units of M$_\odot$ yr^{-1} kpc^{-2}.

The ΣSFR$_\star$ values were calculated over different age bins, comprising values over the last 1, 5, 10, 14, 20, 30, 56 and 100 Myr, each age bin corresponding to the added contribution of all younger age bins. These ΣSFR$_\star$ values are compared to the ΣSFR$_{\rm Gas}$ ones in Fig. 1 for the total sample (sum of AGN and control samples) and in Fig. 2 for the SF spaxels only in the AGN hosts. We also present the identity line (e.g. x=y; dotted blue) together with a linear fit to the data points (solid red line) obtained using bootstrap realisations (Davison & Hinkley 1997) with Huber Regressor model that is robust to outliers (Owen 2007). The Spearman's correlation coefficient (r) and the number of spaxels are also included in the panels showing the plots.

What emerges from this exercise is that the best correlation (r = 0.62 for SF of the control+AGN samples and r = 0.80 if only SF spaxels in the AGN sample are considered) is obtained when comparing the ΣSFR$_\star$ over the last 20 Myr with that obtained with ΣSFR$_{\rm Gas}$ (from the Hα emission line). Also, their

---

[1] http://www.starlight.ufsc.br/

[2] https://ifscube.readthedocs.io/en/latest/

values are close to a one to one relation, with $\log(\Sigma\mathrm{SFR}_\star) = (0.79 \pm 0.006)\log(\Sigma\mathrm{SFR}_\mathrm{Gas}) - (0.22 \pm 0.009)$. This is also the stellar population age range that shows the smallest scatter of the points compared with the $\Sigma\mathrm{SFR}_\star$ derived over the other Δt's. This result is not surprising since the good agreement between the $\Sigma\mathrm{SFR}_\mathrm{Gas}$ and $\Sigma\mathrm{SFR}_\star$ over the last 20 Myr is related to the fact that the stars which dominate the total ionising photons budget are the hot, massive ($M > 10M_\odot$) and short-lived ($t < 20$ Myr) stars. Thus, as the emission-line fluxes provide an 'instantaneous' measure of the SFR (Kennicutt 1998), the corresponding SFR values should be more similar to those obtained from recent $\mathrm{SFR}_\star$. In fact, our results are in agreement with the previous findings of Asari et al. (2007) who found that the $\mathrm{SFR}_\star$ of the last 25 Myr correlates well with that derived via nebular emission when using SDSS single fibber observations.

The above finding shows that one can use the $\Sigma\mathrm{SFR}_\star$ over the last 20 Myr as a probe of the recent, instantaneous SFR that a galaxy is experiencing.

In order to investigate any possible difference in behaviour between the spaxels from the AGN host galaxies and those from the control galaxies, we have plotted in Fig. 3 the $\Sigma\mathrm{SFR}_\mathrm{Gas}$ *versus* $\Sigma\mathrm{SFR}_\star$ over the last 20 Myr (for spaxels with SF line ratios) as grey plus symbols for the control sample and as light blue circles for the AGN hosts. We also plot the mean values, with standard deviations, considering all the spaxels (both from control and AGN galaxies) divided in 20 linearly spaced bins over $\Sigma\mathrm{SFR}_\mathrm{Gas}$. Values below the 0.5th percentile and above the 99.5th percentile were removed to better display the results. The identity line (dotted black) is shown, as well as separate regressions for the two samples (AGN and control) and for their combined sample. We also show histograms for the density distribution[3] of $\Sigma\mathrm{SFR}_\mathrm{Gas}$ and $\Sigma\mathrm{SFR}_\star$ for both samples, as well as an histogram showing the $\Delta\Sigma = \log(\Sigma\mathrm{SFR}_\mathrm{Gas}) - \log(\Sigma\mathrm{SFR}_\star)$ together with the mean (μ) and median ($\tilde{x}$) values of this difference.

Besides obtaining the linear regressions to the data, as described above, we derived the Spearman's correlation coefficients, that are also listed within the Figs. 1 and 3 panels. These figures show that: (i) when considering only SF spaxels from the control sample we found $\log(\Sigma\mathrm{SFR}_\star) = (0.792 \pm 0.006)\log(\Sigma\mathrm{SFR}_\mathrm{Gas}) - (0.224 \pm 0.010)$ with $r = 0.62$; (ii) when using the SF spaxels from the AGN hosts we found $\log(\Sigma\mathrm{SFR}_\star) = (0.957 \pm 0.006)\log(\Sigma\mathrm{SFR}_\mathrm{Gas}) + (0.080 \pm 0.009)$ with $r = 0.80$; and (iii) finally when combining both samples we find $\log(\Sigma\mathrm{SFR}_\star) = (0.872 \pm 0.004)\log(\Sigma\mathrm{SFR}_\mathrm{Gas}) - (0.075 \pm 0.006)$ with $r = 0.70$. The three best-fit lines in Fig. 3 show a very similar slope, and a nearly one to one correlation is found. The difference histogram ($\Delta\Sigma\mathrm{SFR}$) confirms that both ΣSFRs are very similar, with the bulk of the differences being concentrated around ~0. This result suggests that the $\Sigma\mathrm{SFR}_\star$over the last 20 Myrs can be directly used as a measure of the $\Sigma\mathrm{SFR}_\mathrm{Gas}$, for both star forming and AGN hosts (when the spaxel line ratios indicate SF excitation).

At the highest $\Sigma\mathrm{SFR}_\mathrm{Gas}$ and $\Sigma\mathrm{SFR}_\star$ values, there is a clear excess of AGN SF spaxels relative to those from the control ones (histograms in Fig. 3). In order to understand the origin of this excess, our first step was to remove the strong AGNs, defined as the sources with $L([\mathrm{OIII}]\lambda5007) \geq 3.8 \times 10^{40}\,\mathrm{erg\,s^{-1}}$ (Rembold et al. 2017; Mallmann et al. 2018,) from our sample, since, if both the AGN activity and the SF would be driven by the same mechanism (e.g. larger gas reservoirs both forming stars and feeding the AGN) this could explain this excess. However, after the removal of these objects the same trend remains and the excess is still observed. In order to identify the galaxies responsible for the excess, we applied a cut for high ΣSFRs. Selecting only spaxels with $\log(\Sigma\mathrm{SFR}_\mathrm{Gas}) > -1.0$ and $\log(\Sigma\mathrm{SFR}_\star) > -0.75$, we found that all the spaxels presenting these high values come from only four AGN hosts identified by the following MaNGA-IDs: 1-189584, 1-604022, 1-258373,1-229731 (Figs. A1 – A4). Of these, only objects 1-258373 and 1-229731 are strong AGNs. This result shows that not only strong AGNs are producing the high ΣSFRs in Fig. 3.

Since a tight correlation between the SFR and the stellar mass of galaxies is expected, and indeed observed in the form of the so-called *star formation Main Sequence* (MS) of galaxies (Brinchmann et al. 2004; Noeske et al. 2007; Daddi et al. 2007; Speagle et al. 2014, it is also observed when considering individual spaxels, e.g. Lin et al. 2019), we decided to normalise the ΣSFRs to the stellar mass, $M_\star$, of each spaxel. The result of this normalisation is shown in Fig. 4, where one clearly sees that the spaxels contributing to the tail observed in the distributions of the AGN spaxels in the previous histograms are those with the highest $\Sigma\mathrm{SFR/M}_\star$, and they clearly populate a separate region in this figure.

In order to investigate the origin of these high $\Sigma\mathrm{SFR}/M_\star$'s, we have tracked them back to the sources originating such spaxels. Therefore, using Fig. 4 we defined the limits of the high-$\Sigma\mathrm{SFR}/M_\star$ "cloud" as $\log(\Sigma\mathrm{SFR}_\mathrm{Gas}/M_\star) > -8.2$ and $\log(\Sigma\mathrm{SFR}_\star/M_\star) > -7.8$ (cyan rectangle). The spaxels located in this region are from four AGNs, identified by the MANGAIDs: 1-189584, 1-604022 (these two being also identified as producing the high values in Figs. 1 and 3, plus 1-603941, 1-420924, none of which is classified as strong AGNs.

This result suggests that these sources are somewhat particular in the sense of having a significantly larger star-forming gas reservoir leading to a higher star-formation rate than the other sources in our sample. Interestingly, all these sources present companions or satellite galaxies at projected distances smaller than 70 kpc. In addition, objects 1-189584, 1-604022 and 1-603941 are members of galaxy groups (Fouque et al. 1992; White et al. 1999; Von Der Linden et al. 2007). This suggests that the higher star formation efficiencies shown by these objects relative to other galaxies of similar masses is due to interactions with nearby galaxies. A definitive answer to this question requires a complete statistics of the environment of all galaxies in the sample, which is beyond the scope of this work but will be addressed in a forthcoming publication.

The results presented here clearly show that we can use the transformation equation:

$$\log(\Sigma\mathrm{SFR}_\star) = (0.872 \pm 0.004)\log(\Sigma\mathrm{SFR}_\mathrm{Gas}) - (0.075 \pm 0.006) \quad (10)$$

or

$$\log(\Sigma\mathrm{SFR}_\mathrm{Gas}) = (1.147 \pm 0.005)\log(\Sigma\mathrm{SFR}_\star) + (0.086 \pm 0.080)$$

to obtain the gas ΣSFR from the stellar one.

The above result is particularly useful for obtaining SFR values in the narrow-line region (NLR) or extended NLR (ENLR) of AGN hosts. Since the synthesis technique allows to fit the stellar populations disentangling it from the AGN featureless continuum, it is possible to use it to obtain the SFRs that one would derive from the gas emission, even in regions dominated by the AGN excitation, such as the NLR and ENLR, for which HI emission cannot be used as a star-formation indicator.

These results can thus be used to investigate if there is, for example, SF quenching (or SF enhancement) in the vicinity of AGN,

---

[3] The counts are normalised to form a probability density, i.e. the integral under the histogram is 1. This is achieved by dividing the count by the number of observations times the bin width and not dividing by the total number of observations. The density histograms were obtained setting `density=True` in Python's MATPLOTLIB.PYPLOT.HIST routine.

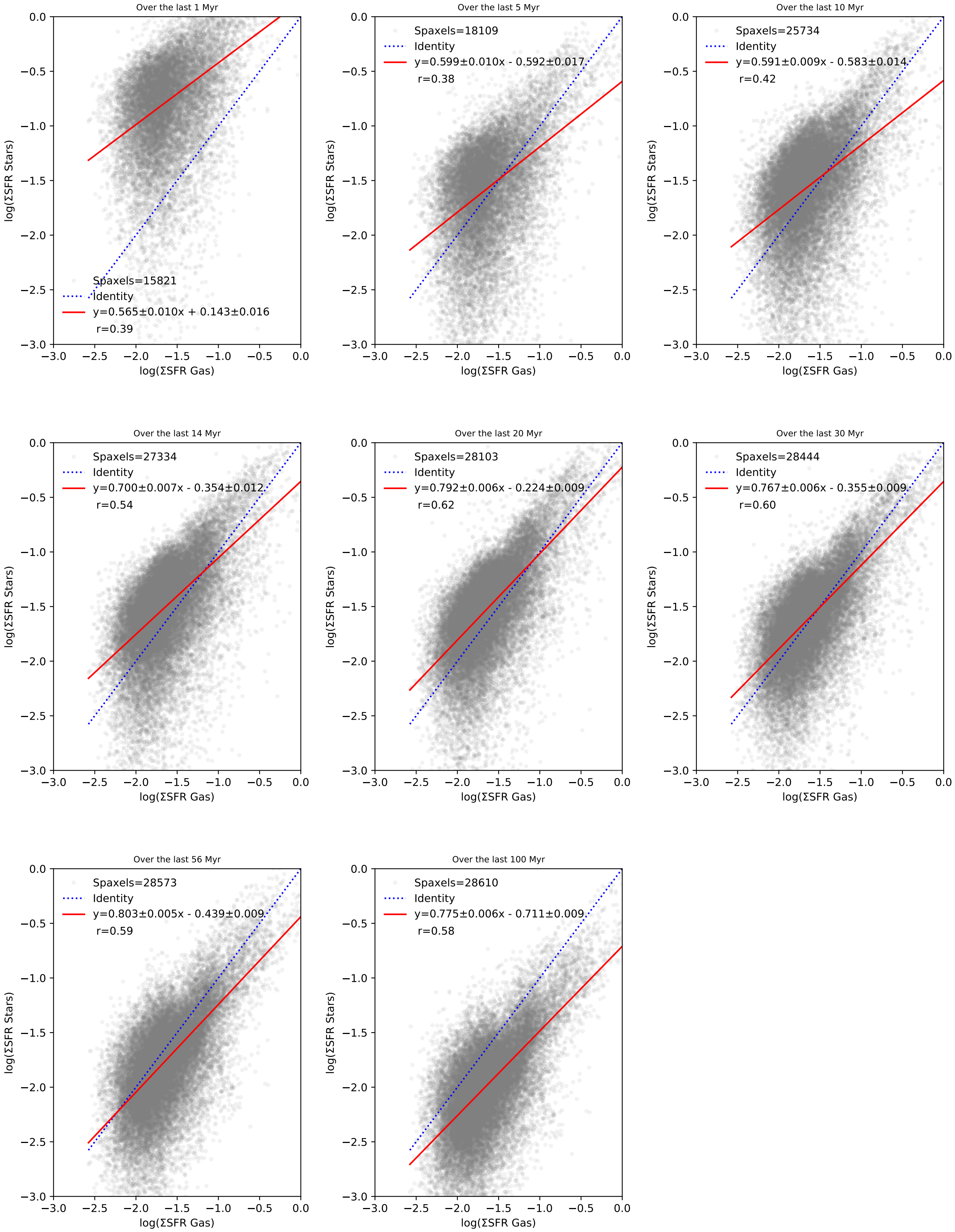

Figure 1. Comparison of $\Sigma\mathrm{SFR}_{\mathrm{Gas}}$ with $\Sigma\mathrm{SFR}_{\star}$ in logarithm units of $\mathrm{M}\odot\ \mathrm{yr}^{-1}\ \mathrm{kpc}^{-2}$ over the last 1, 5, 10, 14, 20, 30, 56 and 100 Myr, for all spaxels of the AGN and control samples obeying the criteria of Sec. 3.1. The red line is the linear relation of a robust fit between $\log(\Sigma\mathrm{SFR}_{\mathrm{Gas}})$ and $\log(\Sigma\mathrm{SFR}_{\star})$ given inside the panels. We also list the number of spaxels and the Spearman's correlation coefficient (r) of the relation. For more details see text.

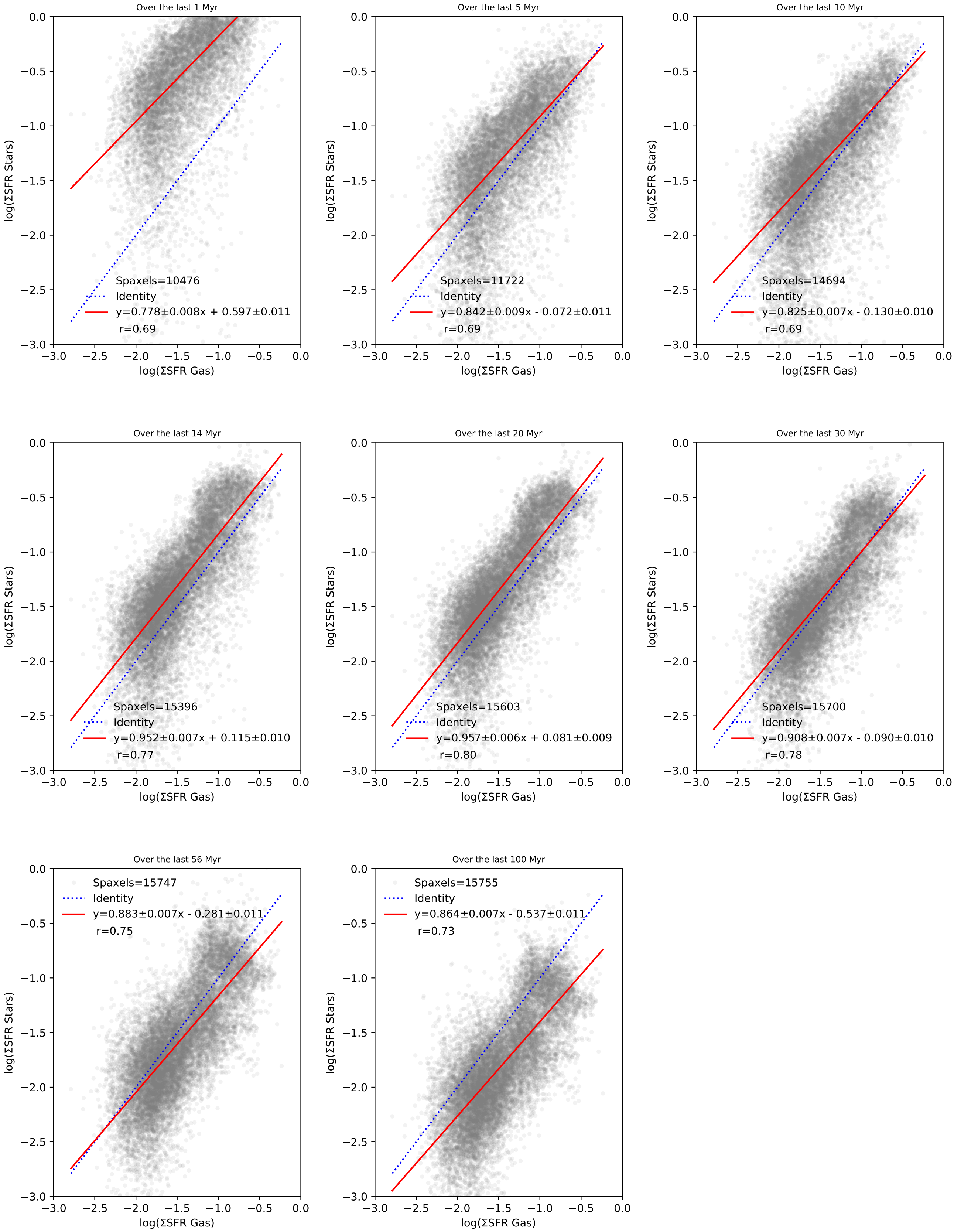

Figure 2. Same as Fig. 1 but only for the star-forming spaxels in the AGN sample.

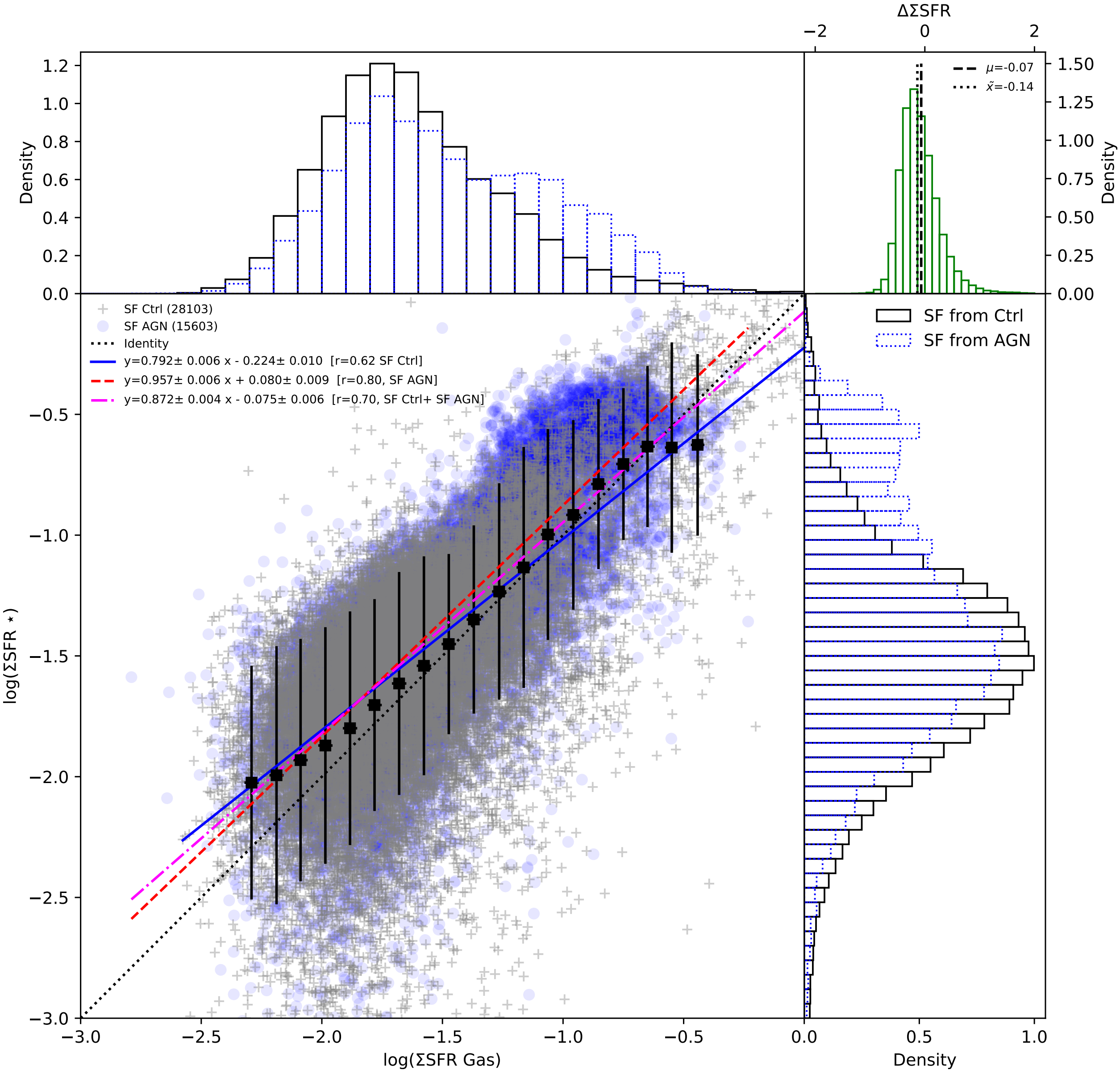

Figure 3. $\Sigma\mathrm{SFR}_{\star}$ *versus* $\Sigma\mathrm{SFR}_{\mathrm{Gas}}$ over the last 20 Myrs in log scale. Spaxels with SF line ratios taken from the control sample ("Ctrl") are represented as grey plus symbols, SF spaxels taken from AGN hosts as light blue circles. Regressions for each data set are labelled. Squares represent the mean value with standard deviations of 20 linearly spaced bins over $\log(\Sigma\mathrm{SFR}_{\mathrm{Gas}})$ (values below 0.5 and 99.5 of the q-th percentile were removed) considering all spaxels (SF Ctrl and SF AGN). Density histograms for $\Sigma\mathrm{SFR}_{\mathrm{Gas}}$ and $\Sigma\mathrm{SFR}_{\star}$ of both samples are also shown. The top right histogram shows the $\Delta\Sigma = \log(\Sigma\mathrm{SFR}_{\mathrm{Gas}}) - \log(\Sigma\mathrm{SFR}_{\star})$ as well as the mean (μ) and median ($\tilde{x}$) values of this difference.

comparing the results with the predictions of AGN feedback effects in cosmological simulations (e.g. Nelson et al. 2015; McAlpine et al. 2016). In a forthcoming publication we intend to apply the relation of eq. 10 in order to compare the ΣSFR we obtain in regions dominated by AGNs excitation to those obtained at similar distances from the nucleus for control galaxies in order to investigate any difference related to the AGN. The results will then be compared to those of cosmological simulations predictions (Schimoia et al. *in preparation*). In addition, we will extend the investigation previously done for a smaller sample (Mallmann et al. 2018) on the systematic stellar population differences between AGN hosts and controls for the updated sample used here (Mallmann et al. *in preparation*).

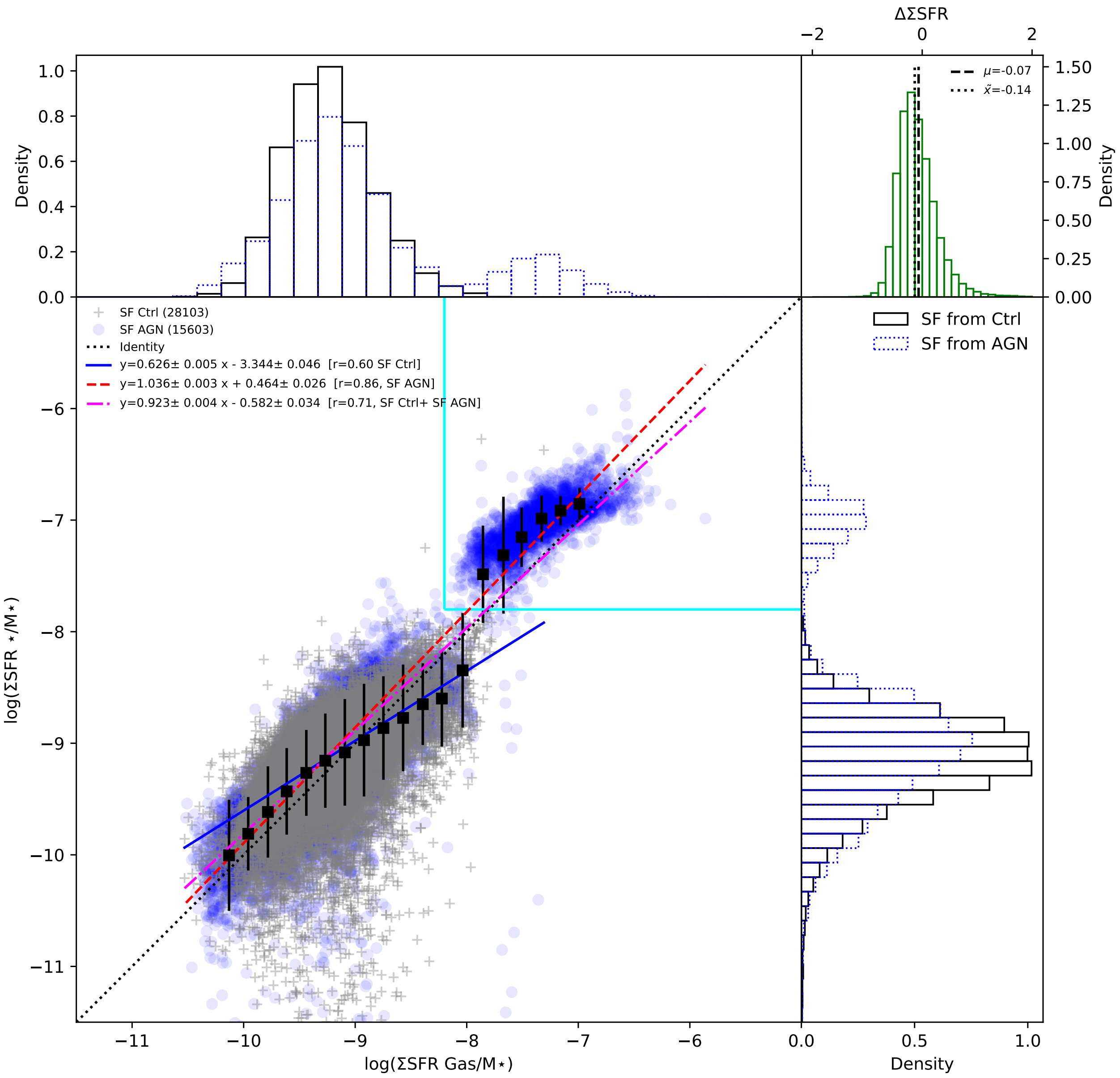

Figure 4. $\Sigma\mathrm{SFR}_{\mathrm{Gas}}$ *versus* $\Sigma\mathrm{SFR}_{\star}$over the last 20 Myrs normalized by stellar mass. Spaxels with SF line ratios taken from the control sample are grey plus symbols, SF spaxels taken from AGN hosts are light blue circles. Regressions over each data set are labelled. Squares represent the mean value with standard deviations of 20 linearly spaced bins over $\Sigma\mathrm{SFR}_{\mathrm{Gas}}$(values below 0.5 and 99.5 of the q-th percentile were removed) considering all spaxels (SF from Ctrl and SF AGNs). Density histograms of both samples are also shown. The cyan rectangle represents the high $\Sigma\mathrm{SFR}/M_{\star}$ region, namely: $\log(\Sigma\mathrm{SFR}_g/M_{\star}) > -8.2$ and $\log(\Sigma\mathrm{SFR}_{\star}/M_{\star}) > -7.8$.

4.2 Comparing the nebular and stellar population reddening

A comparison between the A_V values obtained via Hα/Hβ line ratios and that from the full spectral fitting of the stellar population is shown in Fig. 5. We fitted linear regressions to the data and derived the Spearman's correlation coefficients. We found that: (i) when considering only SF spaxels from the control sample $A_{V,\star} = (0.379 \pm 0.003)A_{V,g} - (0.050 \pm 0.004)$, with $r = 0.60$; (ii) when using the SF spaxels from the AGN hosts, $A_{V,\star} = (0.352 \pm 0.005)A_{V,g} - (0.015 \pm 0.006)$, with $r = 0.55$; and (iii) when considering the combined samples of AGN and controls we find $A_{V,\star} = (0.370 \pm 0.003)A_{V,g} - (0.039 \pm 0.003)$, with $r = 0.58$.

This result suggests that the reddening derived via stellar population full spectral fitting is consistent for both samples and that the extinction derived for the gas $A_{V,g}$ is consistently larger than $A_{V,\star}$

by a multiplicative factor ranging from 2.64 to 2.85, depending on the sample. The larger values obtained for the gas extinction than those of the stars is in agreement with the similar finding of Calzetti et al. (1994), who have analysed IUE UV and optical spectra of 39 starburst and blue compact galaxies and studied the average properties of dust extinction. They found that the optical depth obtained via Balmer emission lines is about twice that obtained via the underlying continuum around these lines. They interpret this difference as a consequence of the fact that the hot ionising stars are associated with dustier regions than that of older (colder) stars that contribute also to the continuum.

We thus interpret the difference we found for the extinction of the stellar population via full spectral fitting and that of the gas as being due to the fact that STARLIGHT works with a single reddening for all the population components (e.g. the final mix is reddened). Since the old component contributes significantly ($\gtrsim$ 60 per cent) to the integrated light in almost all spaxels (see Fig.1 of Mallmann et al. 2018), its reddening dominates the reddening of the final integrated model spectrum. The reddening of this older and cooler underlying population is therefore lower than that of the younger components, that are buried deeper in the dust (and are responsible to ionise the line-emitting gas).

5 CONCLUSIONS

We have presented a comparison between star-formation rate surface densities obtained from spectral synthesis of the stellar population $\Sigma\mathrm{SFR}_\star$ and from the Hα gas emission $\Sigma\mathrm{SFR}_\mathrm{Gas}$ for an updated sample of 170 AGN and 291 control galaxies relative to our initial sample defined by Rembold et al. (2017). We have used the corresponding MaNGA datacubes selecting only spaxels high SNR continuum, with strong emission lines and showing star-forming line ratios as obtained from diagnostic diagrams. Our main results can be summarised as follows.

- The $\Sigma\mathrm{SFR}_\star$ over the last 20 Myrs and $\Sigma\mathrm{SFR}_\mathrm{Gas}$ shows the best correlation among all tested age bins, both including in the analysis the SF spaxels from AGN hosts or only those from control galaxies. The transformation equation is $\log(\Sigma\mathrm{SFR}_\star) = (0.872\pm0.004)\log(\Sigma\mathrm{SFR}_\mathrm{Gas}) - (0.075\pm0.006)$ or $\log(\Sigma\mathrm{SFR}_\mathrm{Gas}) = (1.147\pm0.005)\log(\Sigma\mathrm{SFR}_\star) + (0.086\pm0.080)$. This result opens a new way to obtain the SFRs in AGN hosts, even in the NLR and ENLR, were the AGN dominates the excitation of the emission lines and the SFR cannot be obtained directly from the HI line fluxes.
- A few AGN hosts show an excess of ΣSFR relative to the rest of the sample which we tentatively attribute to a larger gas reservoir and star formation efficiency. Coincidentally, these AGNs seem to have close neighbours, thus the interaction could have boosted the star formation (to be further investigated due to the small size of the sample).
- We found that the visual extinction $A_{V,g}$ derived from the Balmer decrement is 2.63 to 2.86 times larger than the extinction derived from the stellar population synthesis, $A_{V,star}$. This result is in agreement with previous literature results based on much smaller samples. We interpret the difference as being due to the fact that STARLIGHT works with a single reddening for all populations, and the reddening of the stellar content is dominated by the older population that is less extincted than the young stellar population that would be similarly extincted as the star-forming gas.

The transformation equation presented here (Eq. 10) can be used to obtain the gas ΣSFR in AGN hosts via stellar population synthesis using the full spectral fitting. Since the synthesis allows disentangling the contributions of the stellar populations from that of the AGN featureless continuum, it is possible to obtain the ΣSFRs that one would derive for the gas emission, even in regions dominated by AGN excitation. The obtained SFRs in AGN hosts can then be compared with those obtained for control galaxies to investigate the effect of AGN on the surrounding stellar population as well as be compared (and incorporated) with the SFR values predicted as due to AGN feedback effects on the host galaxies in cosmological simulations.

ACKNOWLEDGEMENTS

We thank an anonymous referee for comments and suggestions that have helped improving the text. R.R. Thanks CNPq, CAPES and FAPERGS for financial support, as well as to Marina Trevisan for useful discussions of the present results. RAR thanks partial financial support from Conselho Nacional de Desenvolvimento Científico e Tecnológico (202582/2018-3 and 302280/2019-7) and Fundação de Amparo à pesquisa do Estado do Rio Grande do Sul (17/2551-0001144-9 and 16/2551-0000251-7). MB acknowledges support from FONDECYT regular grant 1170618. GSC acknowledges the support from CONICYT FONDECYT project No. 3190561.

SDSS is managed by the Astrophysical Research Consortium for the Participating Institutions of the SDSS Collaboration including the Brazilian Participation Group, the Carnegie Institution for Science, Carnegie Mellon University, the Chilean Participation Group, the French Participation Group, Harvard-Smithsonian Center for Astrophysics, Instituto de Astrofisica de Canarias, The Johns Hopkins University, Kavli Institute for the Physics and Mathematics of the Universe (IPMU) / University of Tokyo, the Korean Participation Group, Lawrence Berkeley National Laboratory, Leibniz Institut für Astrophysik Potsdam (AIP), Max-Planck-Institut für Astronomie (MPIA Heidelberg), Max-Planck-Institut für Astrophysik (MPA Garching), Max-Planck-Institut für Extraterrestrische Physik (MPE), National Astronomical Observatories of China, New Mexico State University, New York University, University of Notre Dame, Observatório Nacional / MCTI, The Ohio State University, Pennsylvania State University, Shanghai Astronomical Observatory, United Kingdom Participation Group, Universidad Nacional Autónoma de México, University of Arizona, University of Colorado Boulder, University of Oxford, University of Portsmouth, University of Utah, University of Virginia, University of Washington, University of Wisconsin, Vanderbilt University, and Yale University.

This research made use of Astropy,[4] a community-developed core Python package for Astronomy (Astropy Collaboration et al. 2013, 2018).

DATA AVAILABILITY

The data underlying this article are available under SDSS collaboration rules, and the by products will be shared on reasonable request to the corresponding author.

REFERENCES

Aghanim N., et al., 2020, Astronomy & Astrophysics, 641, A6

---

[4] http://www.astropy.org

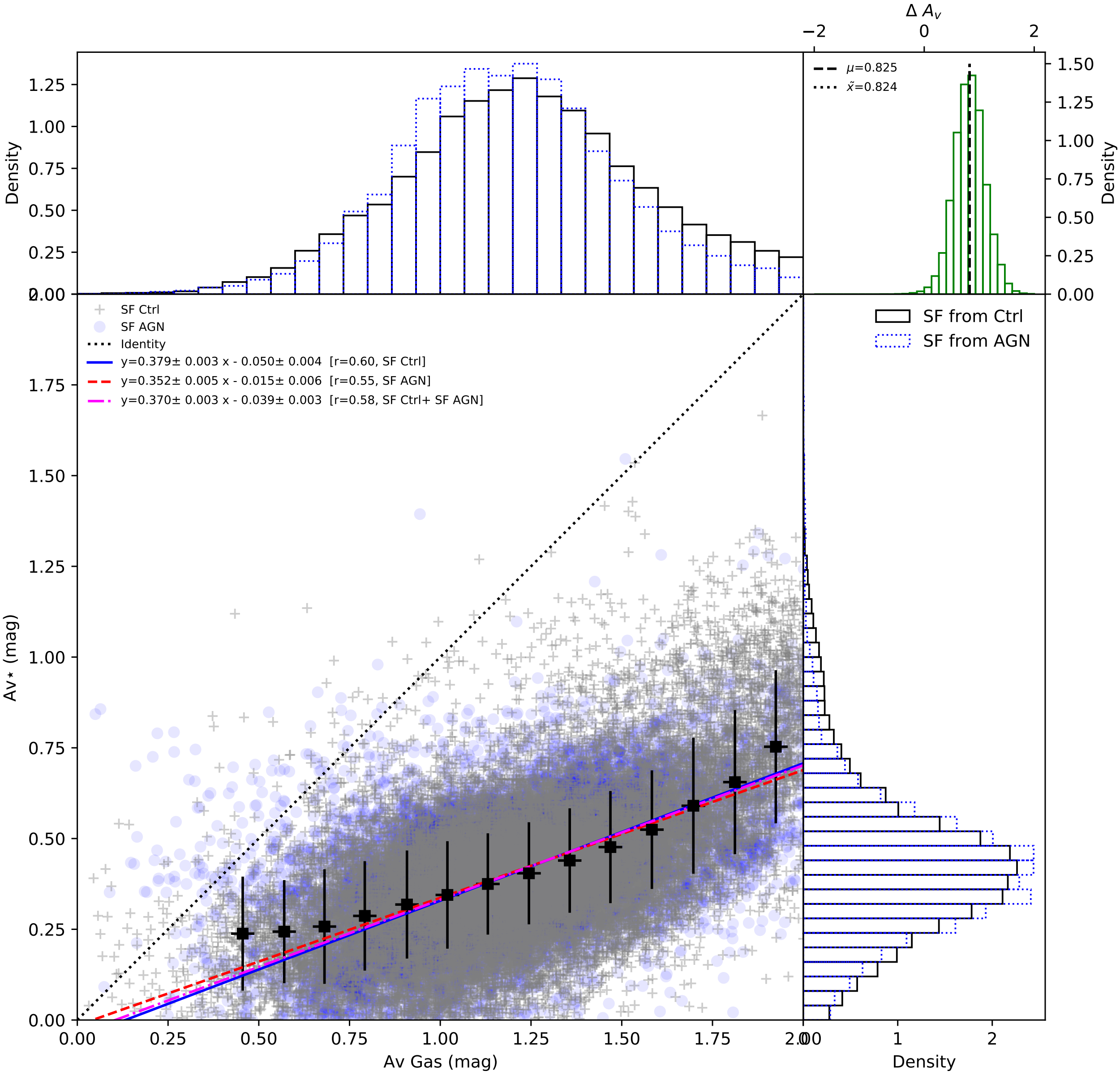

Figure 5. Gas reddening *versus* full spectral fitting reddening. Spaxels with SF line ratios taken from the control sample are grey plus symbols, SF spaxels taken from AGN hosts are light blue circles. Regressions over each data set are labelled. Squares represent the mean value with standard deviations of 20 linearly spaced bins over $\Sigma\mathrm{SFR}_{\mathrm{Gas}}$(values below 0.5 and 99.5 of the q-th percentile were removed) considering all spaxels (SF from Ctrl and SF AGNs). Density histograms of both samples are also shown.

Aguado D. S., et al., 2019, The Astrophysical Journal Supplement Series, 240, 23

Asari N. V., Cid Fernandes R., Stasińska G., Torres-Papaqui J. P., Mateus A., Sodré L., Schoenell W., Gomes J. M., 2007, Monthly Notices of the Royal Astronomical Society, 381, 263

Astropy Collaboration et al., 2013, Astronomy and Astrophysics, 558, A33

Astropy Collaboration et al., 2018, The Astronomical Journal, 156, 123

Baldry I. K., Glazebrook K., Brinkmann J., Ivezić Ž., Lupton R. H., Nichol R. C., Szalay A. S., 2004, The Astrophysical Journal, 600, 681

Baldwin C., McDermid R. M., Kuntschner H., Maraston C., Conroy C., 2018, Monthly Notices of the Royal Astronomical Society, 473, 4698

Barrera-Ballesteros J. K., et al., 2020, Monthly Notices of the Royal Astronomical Society, 492, 2651

Belfiore F., et al., 2019, The Astronomical Journal, 158, 160

Bieri R., Dubois Y., Silk J., Mamon G. A., Gaibler V., 2016, Monthly Notices of the Royal Astronomical Society, 455, 4166

Blanton M. R., et al., 2017, The Astronomical Journal, 154, 28

Brammer G. B., et al., 2009, The Astrophysical Journal, 706, L173

Brinchmann J., Charlot S., White S. D. M., Tremonti C., Kauffmann G., Heckman T., Brinkmann J., 2004, Monthly Notices of the Royal Astronomical Society, 351, 1151

Bruzual G., Charlot S., 2003, Monthly Notices of the RAS, 344, 1000

Bundy K., et al., 2015, Astrophysical Journal, 798, 7

Calzetti D., Kinney A. L., Storchi-Bergmann T., 1994, The Astrophysical Journal, 429, 582

Calzetti D., Armus L., Bohlin R. C., Kinney A. L., Koornneef J., Storchi-Bergmann T., 2000, The Astrophysical Journal, 533, 682

Cardelli J. A., Clayton G. C., Mathis J. S., 1989, Astrophysical Journal, 345, 245

Cherinka B., et al., 2019, The Astronomical Journal, 158, 74

Cid Fernandes R., 2018, Monthly Notices of the Royal Astronomical Society, 480, 4480

Cid Fernandes R., Gu Q., Melnick J., Terlevich E., Terlevich R., Kunth D., Rodrigues Lacerda R., Joguet B., 2004, Monthly Notices of the RAS, 355, 273

Cid Fernandes R., Mateus A., Sodré L., Stasińska G., Gomes J. M., 2005, Monthly Notices of the RAS, 358, 363

Cid Fernandes R., et al., 2013, Astronomy and Astrophysics, 557, A86

Cid Fernandes R., et al., 2014, Astronomy and Astrophysics, 561, A130

Crain R. A., et al., 2015, Monthly Notices of The Royal Astronomical Society, 450, 1937

Croton D. J., et al., 2006, Monthly Notices of The Royal Astronomical Society, 365, 11

Daddi E., et al., 2007, The Astrophysical Journal, 670, 156

Davison A. C., Hinkley D. V., 1997, Bootstrap Methods and Their Application, /core/books/bootstrap-methods-and-their-application/ED2FD043579F27952363566DC09CBD6A, doi:10.1017/CBO9780511802843

Domínguez A., et al., 2013, The Astrophysical Journal, 763, 145

Drory N., et al., 2015, The Astronomical Journal, 149, 77

El-Badry K., Wetzel A., Geha M., Hopkins P. F., Kereš D., Chan T. K., Faucher-Giguère C.-A., 2016, The Astrophysical Journal, 820, 131

Fabian A. C., 2012, Annual Review of Astronomy and Astrophysics, 50, 455

Fouque P., Gourgoulhon E., Chamaraux P., Paturel G., 1992, Astronomy and Astrophysics Supplement Series, 93, 211

Gallagher R., Maiolino R., Belfiore F., Drory N., Riffel R., Riffel R. A., 2019, Monthly Notices of the Royal Astronomical Society, 485, 3409

González Delgado R. M., Cerviño M., Martins L. P., Leitherer C., Hauschildt P. H., 2005, Monthly Notices of the Royal Astronomical Society, 357, 945

Granato G. L., De Zotti G., Silva L., Bressan A., Danese L., 2004, The Astrophysical Journal, 600, 580

Gunn J. E., et al., 2006, The Astronomical Journal, 131, 2332

Hao C.-N., Kennicutt R. C., Johnson B. D., Calzetti D., Dale D. A., Moustakas J., 2011, The Astrophysical Journal, 741, 124

Hopkins P. F., 2012, Monthly Notices of the RAS, 420, L8

Ishibashi W., Fabian A. C., 2012, Monthly Notices of the Royal Astronomical Society, 427, 2998

Kauffmann G., et al., 2003a, Monthly Notices of the Royal Astronomical Society, 341, 54

Kauffmann G., et al., 2003b, Monthly Notices of the RAS, 346, 1055

Kennicutt Jr. R. C., 1998, Annual Review of Astron and Astrophys, 36, 189

Kennicutt R. C., Evans N. J., 2012, Annual Review of Astronomy and Astrophysics, 50, 531

Kennicutt Jr. R. C., et al., 2009, The Astrophysical Journal, 703, 1672

King A., Pounds K., 2015, Annual Review of Astronomy and Astrophysics, 53, 115

Law D. R., et al., 2015, The Astronomical Journal, 150, 19

Law D. R., et al., 2016, The Astronomical Journal, 152, 83

Lin L., et al., 2019, The Astrophysical Journal Letters, 884, L33

Lintott C. J., et al., 2008, Monthly Notices of the Royal Astronomical Society, 389, 1179

Lintott C., et al., 2011, Monthly Notices of the Royal Astronomical Society, 410, 166

Mallmann N. D., et al., 2018, Monthly Notices of the RAS, 478, 5491

McAlpine S., et al., 2016, Astronomy and Computing, 15, 72

Muzzin A., et al., 2013, The Astrophysical Journal, 777, 18

Nayakshin S., Zubovas K., 2012, Monthly Notices of the Royal Astronomical Society, 427, 372

Nelson D., et al., 2015, Astronomy and Computing, 13, 12

Nelson D., et al., 2019, Monthly Notices of the Royal Astronomical Society, 490, 3234

Noeske K. G., et al., 2007, The Astrophysical Journal Letters, 660, L47

Osterbrock D. E., Ferland G. J., 2006, Astrophysics of gaseous nebulae and active galactic nuclei, 2nd. ed. by D.E. Osterbrock and G.J. Ferland. Sausalito, CA: University Science Books, 2006

Owen A., 2007, Contemp. Math., 443

Peterken T., Merrifield M., Aragón-Salamanca A., Fraser-McKelvie A., Avila-Reese V., Riffel R., Knapen J., Drory N., 2020, Monthly Notices of the Royal Astronomical Society, 495, 3387

Rees M. J., 1989, Monthly Notices of the Royal Astronomical Society, 239, 1P

Rembold S. B., et al., 2017, Monthly Notices of the Royal Astronomical Society, 472, 4382

Riffel R., Pastoriza M. G., Rodríguez-Ardila A., Maraston C., 2008, Monthly Notices of the RAS, 388, 803

Riffel R., Pastoriza M. G., Rodríguez-Ardila A., Bonatto C., 2009, Monthly Notices of the RAS, 400, 273

Riffel R. A., Zakamska N. L., Riffel R., 2020, Monthly Notices of the Royal Astronomical Society, 491, 1518

Rosario D. J., Burtscher L., Davies R., Genzel R., Lutz D., Tacconi L. J., 2013, The Astrophysical Journal, 778, 94

Rosario D. J., Mendel J. T., Ellison S. L., Lutz D., Trump J. R., 2016, Monthly Notices of the Royal Astronomical Society, 457, 2703

Rosario D. J., et al., 2018, Monthly Notices of the Royal Astronomical Society, 473, 5658

Ruschel-Dutra 2020, Danielrd6/Ifscube v1.0, Zenodo, doi:10.5281/zenodo.3945237

Salim S., Boquien M., Lee J. C., 2018, The Astrophysical Journal, 859, 11

Schaye J., et al., 2015, Monthly Notices of the Royal Astronomical Society, 446, 521

Smee S. A., et al., 2013, The Astronomical Journal, 146, 32

Speagle J. S., Steinhardt C. L., Capak P. L., Silverman J. D., 2014, The Astrophysical Journal Supplement Series, 214, 15

Springel V., et al., 2005, Nature, 435, 629

Trussler J., Maiolino R., Maraston C., Peng Y., Thomas D., Goddard D., Lian J., 2020, Monthly Notices of the Royal Astronomical Society, 491, 5406

Vazdekis A., Sánchez-Blázquez P., Falcón-Barroso J., Cenarro A. J., Beasley M. A., Cardiel N., Gorgas J., Peletier R. F., 2010, Monthly Notices of the Royal Astronomical Society, 404, 1639

Vazdekis A., Koleva M., Ricciardelli E., Röck B., Falcón-Barroso J., 2016, Monthly Notices of the RAS, 463, 3409

Vogelsberger M., et al., 2014, Nature, 509, 177

Von Der Linden A., Best P. N., Kauffmann G., White S. D. M., 2007, Monthly Notices of the Royal Astronomical Society, 379, 867

Wake D. A., et al., 2017, The Astronomical Journal, 154, 86

Walcher J., Groves B., Budavári T., Dale D., 2011, Astrophysics and Space Science, 331, 1

Wang X., Loeb A., 2018, New Astronomy, 61, 95

Weinberger R., et al., 2017, Monthly Notices of the Royal Astronomical Society, 465, 3291

Westfall K. B., et al., 2019, The Astronomical Journal, 158, 231

Wetzel A. R., Tinker J. L., Conroy C., 2012, Monthly Notices of the Royal Astronomical Society, 424, 232

White R. A., Bliton M., Bhavsar S. P., Bornmann P., Burns J. O., Ledlow M. J., Loken C., 1999, The Astronomical Journal, 118, 2014

Yan R., et al., 2016a, The Astronomical Journal, 151, 8

Yan R., et al., 2016b, The Astronomical Journal, 152, 197

Zhuang M.-Y., Ho L. C., 2020, The Astrophysical Journal, 896, 108

Zhuang M.-Y., Ho L. C., Shangguan J., 2019, The Astrophysical Journal, 873, 103

Zhuang M.-Y., Ho L. C., Shangguan J., 2020, arXiv e-prints, 2007, arXiv:2007.11285

Zubovas K., Bourne M. A., 2017, Monthly Notices of the RAS, 468, 4956

Zubovas K., Nayakshin S., King A., Wilkinson M., 2013, Monthly Notices of the Royal Astronomical Society, 433, 3079
van der Wel A., et al., 2014, The Astrophysical Journal, 788, 28

APPENDIX A: INDIVIDUAL MAPS

Here we present individual maps for the four high ΣSFR/M$_\star$ ratio, in left from top to bottom Av$_{gas}$, Av$_\star$, Av$_{gas}$/ Av$_\star$ and in right side from top to bottom SFR$_{gas}$, SFR$_\star$, SFR$_{gas}$/ SFR$_\star$ note that a direct comparison of both quantities in individual galaxies is possible because the spaxels have the same area and that the ratio is showing how both quantities compare.

This paper has been typeset from a TEX/LATEX file prepared by the author.

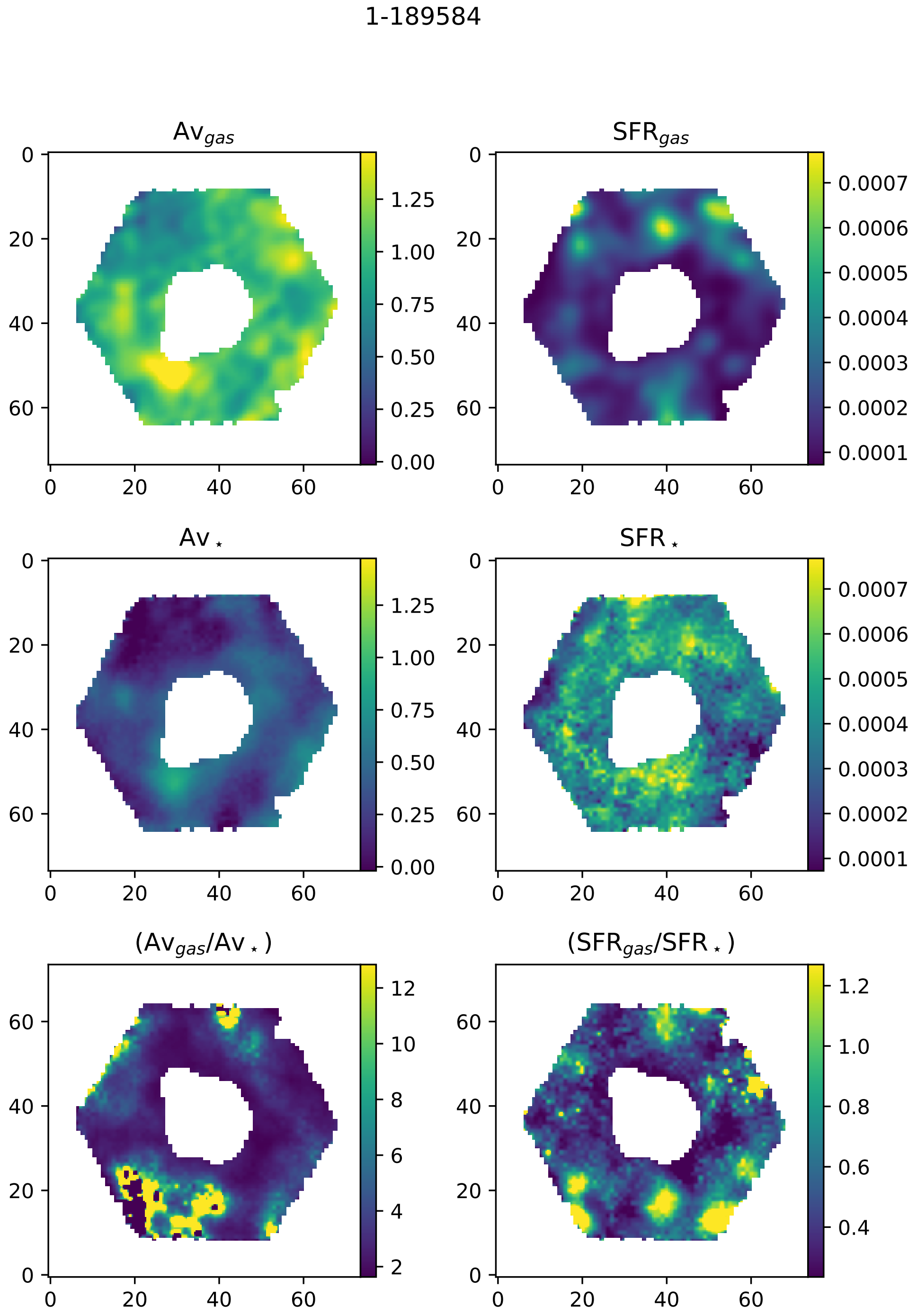

Figure A1. Individual maps for the four high ΣSFR/M$_\star$ for MANGAID 1-189584. Left side: from top to bottom A$_{Vg}$, A$_{V\star}$, Av$_{gas}$/ Av$_\star$. Right side: from top to bottom SFR$_g$, SFR$_\star$, SFR$_g$/ SFR$_\star$. SFR are givens in $M_\odot yr^{-1}$ and A$_V$ in mag.

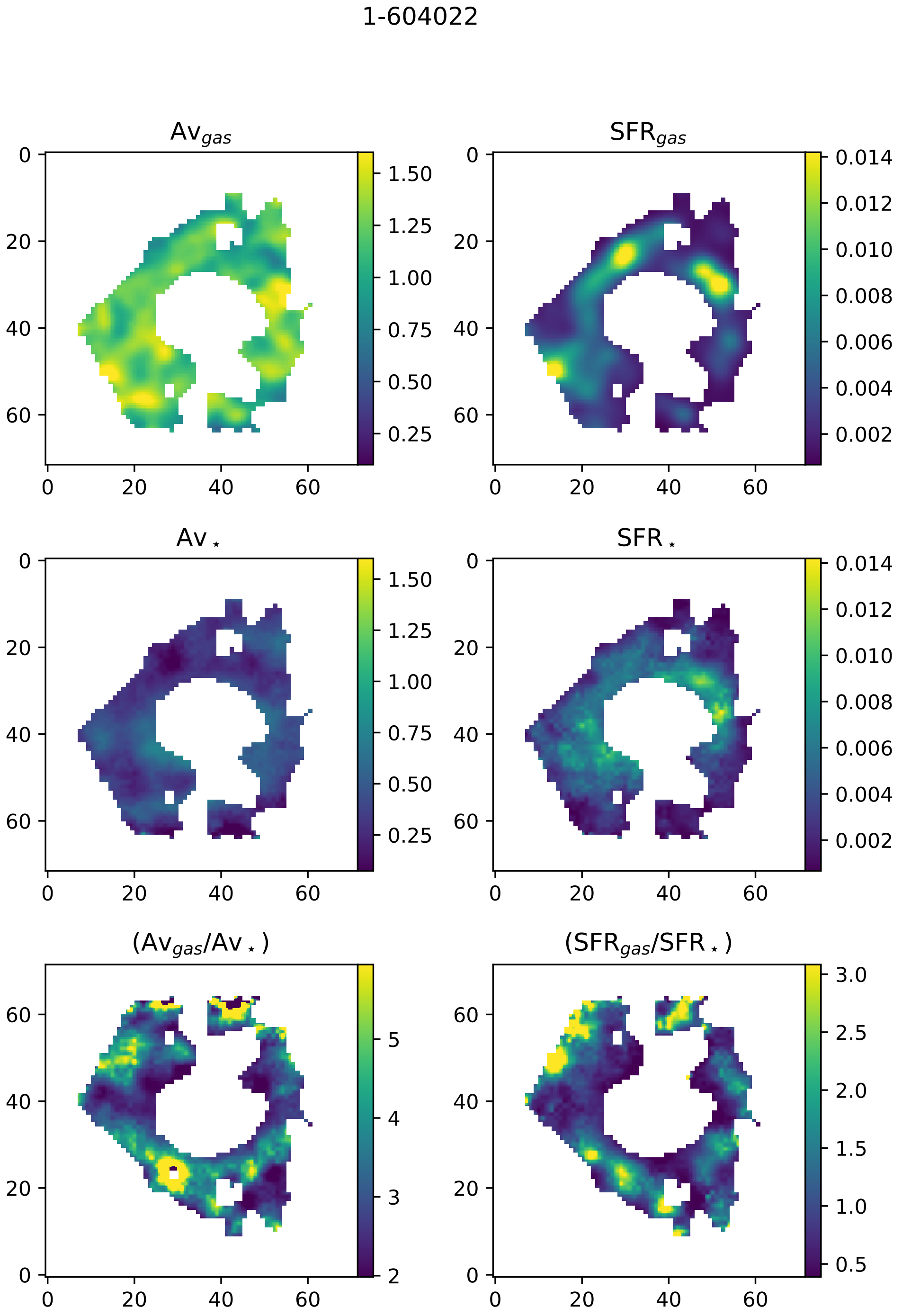

Figure A2. Same as Fig. A1 but for 1-604022

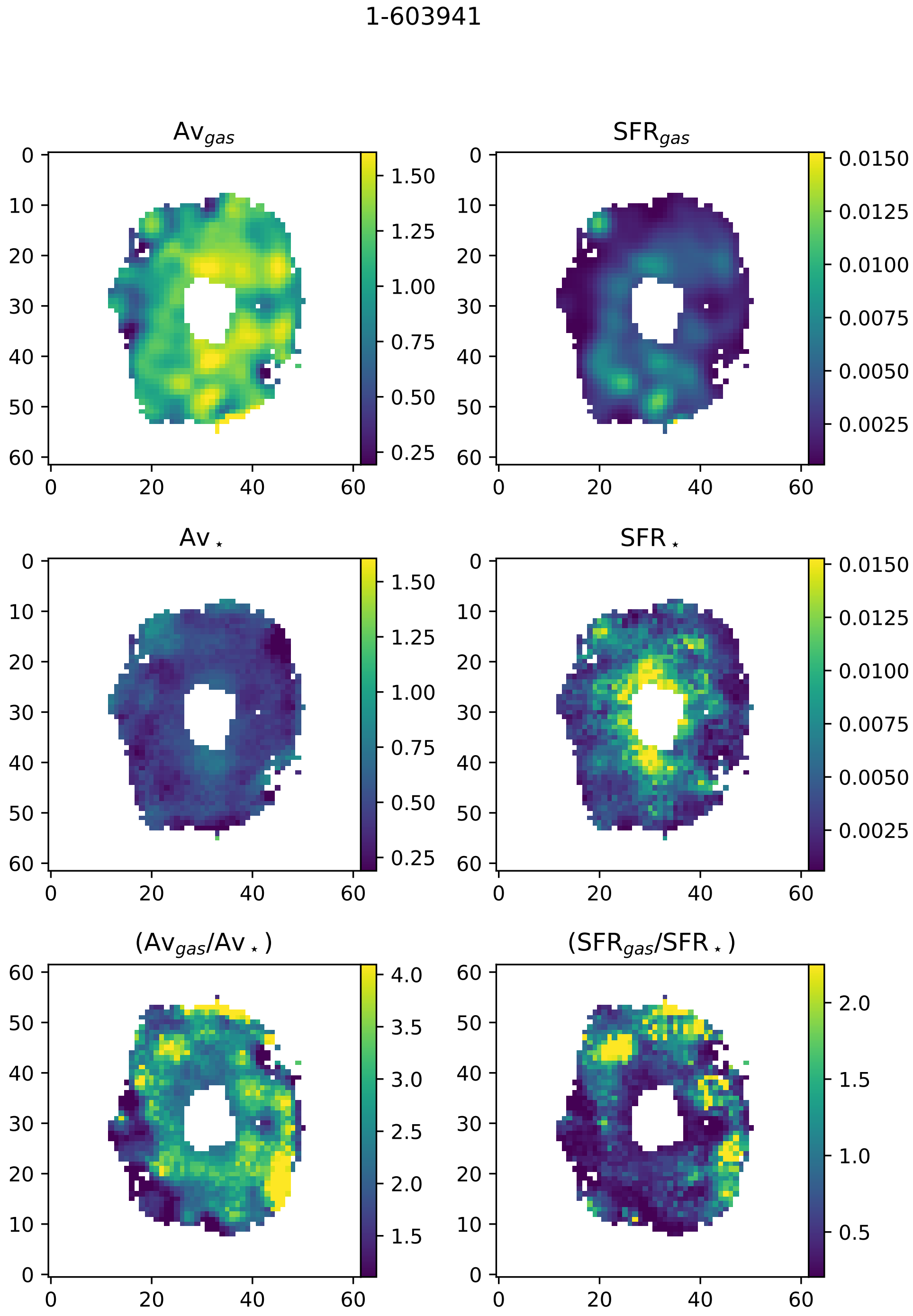

Figure A3. Same as Fig. A1 but for 1-603941

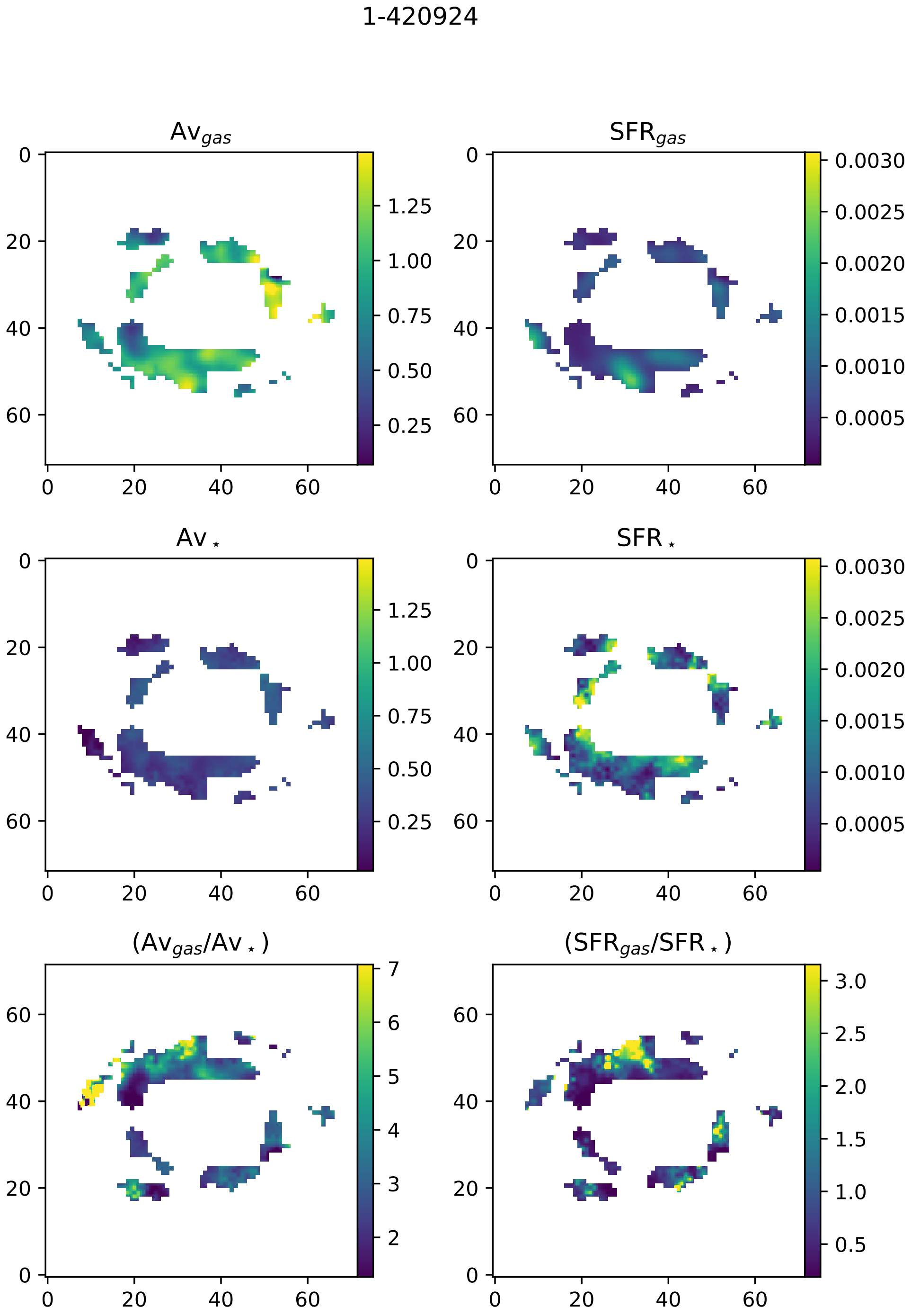

Figure A4. Same as Fig. A1 but for 1-420924

Capítulo 7

Mapeando a população estelar e excitação do gás das galáxias do MaNGA usando MEGACUBES. Resultados para AGNS versus Controles

Neste capitulo apresentaremos os MEGACUBES para as mais de 10 mil galáxias do survey MaNGA e analisaremos a formação estelar na amostra final de AGNs e compararemos com as galáxias controle, bem como faremos uma análise espacial do mecanismo dominante na excitação do gás em ambas as amostras (AGNs e controles). Os resultados deste capítulo foram submetidos para revista Monthly Notices of the Royal Astronomical Society.

MNRAS **000**, 1–?? (2023) Preprint 8 August 2023 Compiled using MNRAS LaTeX style file v3.0

arXiv:2307.11474v2 [astro-ph.GA] 4 Aug 2023

Mapping the stellar population and gas excitation of MaNGA galaxies with MEGACUBES. Results for AGN versus control sample

Rogério Riffel[1,2,4]★, Nicolas D. Mallmann[1,2], Sandro B. Rembold[3,2], Gabriele S. Ilha[3,2,7], Rogemar A. Riffel[3,2], Thaisa Storchi-Bergmann[1,2], Daniel Ruschel-Dutra[5], Alexandre Vazdekis [4,6], Ignacio Martín-Navarro[4,6], Jaderson S. Schimoia[3,2], Cristina Ramos Almeida[4,6], Luiz N. da Costa[2], Glauber C. Vila-Verde[2], Lara Gatto[1,2]

[1] *Departamento de Astronomia, Instituto de Física, Universidade Federal do Rio Grande do Sul, CP 15051, 91501-970, Porto Alegre, RS, Brazil*
[2] *Laboratório Interinstitucional de e-Astronomia - LIneA, Rua Gal. José Cristino 77, Rio de Janeiro, RJ - 20921-400, Brazil*
[3] *Departamento de Física, Centro de Ciências Naturais e Exatas, Universidade Federal de Santa Maria, 97105-900, Santa Maria, RS, Brazil*
[4] *Instituto de Astrofísica de Canarias, Calle Vía Láctea s/n, E-38205 La Laguna, Tenerife, Spain*
[5] *Departamento de Física, Universidade Federal de Santa Catarina, P.O. Box 476, 88040-900, Florianópolis, SC, Brazil*
[6] *Departamento de Astrofísica, Universidad de La Laguna, E-38205, Tenerife, Spain* [7] *Universidade do Vale do Paraíba. Av. Shishima Hifumi, 2911, CEP: 12244-000, São J*

Accepted XXX. Received YYY; in original form ZZZ

ABSTRACT

We present spaxel-by-spaxel stellar population fits for the ~10 thousand MaNGA datacubes. We provide multiple extension fits files, nominated as MEGACUBES, with maps of several properties as well as emission-line profiles that are provided for each spaxel. All the MEGACUBES are available through a web interface (`https://manga.linea.org.br/` or `http://www.if.ufrgs.br/~riffel/software/megacubes/`). We also defined a final Active Galactic Nuclei (AGN) sample, as well as a control sample matching the AGN host galaxy properties. We have analysed the stellar populations and spatially resolved emission-line diagnostic diagrams of these AGNs and compared them with the control galaxies sample. We find that the relative fractions of young ($t \leq 56$ Myr) and intermediate-age (100 Myr $\leq t \leq$ 2 Gyr) show predominantly a positive gradient for both AGNs and controls. The relative fraction of intermediate-age stellar population is higher in AGN hosts when compared to the control sample, and this difference becomes larger for higher [O III] luminosity AGNs. We attribute this to the fact that extra gas is available in these more luminous sources and that it most likely originates from mass-loss from the intermediate-age stars. The spatially resolved diagnostic diagrams reveal that the AGN emission is concentrated in the inner 0.5 R_e (effective radius) region of the galaxies, showing that the AGN classification is aperture dependent and that emission-line ratios have to be taken together with the Hα equivalent width for proper activity classification. We present a composite "BPT+WHAN" diagram that produces a more comprehensive mapping of the gas excitation.

Key words: galaxies: active – galaxies: evolution – galaxies: ISM – galaxies: star formation –galaxies: stellar content

1 INTRODUCTION

The evolution of the present-day galaxies during cosmic time is the result of the transformation of molecular gas into stars, the production (and release) of metals by stellar evolution, and the interaction among these processes and their environments (e.g. internal and external processes). All these evolution/transformation processes leave signatures in the observed properties of galaxies that we can analyze and thus reconstruct the galaxies' star formation histories (SFHs). The study of this fossil record is key to our understanding of the structure, composition, and evolution of galaxies (e.g. Cid Fernandes et al. 2004, 2005; Conselice 2014; Tacconi et al. 2020; Sánchez 2020; Sánchez et al. 2021, and references therein).

Significant improvement in the understanding of galaxy evolution processes has been reached in the last decades, primarily due to new results based on large spectroscopic and imaging surveys such as the Sloan Digital Sky Survey (SDSS, York et al. 2000). These studies have shown that galaxies can roughly be divided into passive and star-forming. The passive galaxies are not forming (or forming at a very low rate) stars and host a red and old stellar population (e.g. the red-and-dead galaxies), while the star-forming galaxies are blue, hosting large fractions of young stellar populations. Such bi-modal behaviour has been observed in a number of studies over the years (e.g. Baldry et al. 2004; Wetzel et al. 2012; Kauffmann et al. 2003a; Noeske et al. 2007; van der Wel et al. 2014; Muzzin et al. 2013; Brammer et al. 2009). However, so far it is not yet clear which mechanisms are stopping the star formation process and transforming the blue star-forming spiral galaxies into *red-and-dead* galaxies, being thus a major challenge in modern astrophysics to understand the nature of the physical mechanisms quenching star formation in galaxies.

★ E-mail: riffel@ufrgs.br

One mechanism that a number of studies have invoked to explain the suppression of the star-formation in galaxies is the active galactic nuclei (AGN) feedback. It can quench star formation by (re)moving and/or heating the gas. In this context, AGN outflows are considered a process that suppresses star-formation (e.g. as negative feedback, see Fabian 2012; King & Pounds 2015; Zubovas & Bourne 2017; Trussler et al. 2020, and references therein). On the other hand, some models and simulations suggest that these outflows and jets can in some cases compress the galactic gas, and therefore enhance/trigger the star-formation (e.g. Rees 1989; Hopkins 2012; Nayakshin & Zubovas 2012; Ishibashi & Fabian 2012; Zubovas et al. 2013; El-Badry et al. 2016; Bieri et al. 2016; Zubovas et al. 2013; Zubovas & Bourne 2017; Wang & Loeb 2018; Gallagher et al. 2019; Bessiere & Ramos Almeida 2022). Additionally, cosmological simulations (e.g. Springel et al. 2005; Vogelsberger et al. 2014; Crain et al. 2015) without the inclusion of feedback effects effects do not reproduce the galaxies luminosity function, underestimate the ages of the most massive galaxies (see Figs. 8 and 10 of Croton et al. 2006) and do provide a limited insight into the nature and source of the feedback processes (e.g. AGN or SN dominated Schaye et al. 2015).

To better understand this kind of process it is very important to study the galaxies' properties in a spatially resolved way so that the AGN effects can be probed at different locations in the host galaxies. This can be done via the use of Integral Field Units (IFUs), which allow the study of ionization sources across the galaxies, the interplay among the global/integrated properties of galaxies with the local (spatially resolved) ones, and the link between these two types of relations as well as the spatial (radial) distribution of such properties (Sánchez 2020; Sánchez et al. 2021).

However, extracting information from IFU data can be complex (Steiner et al. 2009), and hence the analysis of such data with different techniques is desirable. Over the years, our AGNIFS team has developed a series of studies analysing IFU data (e.g. Storchi-Bergmann et al. 2009, 2012; Mallmann et al. 2018; Schnorr-Müller et al. 2021; Riffel et al. 2011, 2017, 2018, 2021a,b,c, 2022; Ilha et al. 2022) and methods to analyze this type of data.

In the present paper, we present MEGACUBES (Mallmann et al. 2018) with our fitting procedures for the ∼ 10 000 datacubes of the Mapping Nearby Galaxies at Apache Point Observatory (MaNGA) survey (Bundy et al. 2015), as well as an analysis of the stellar content of the final AGN sample and a matched control sample (Rembold et al. 2017). This paper is structured as follows: in section 2 we present the updated samples. The fitting procedures and the MEGACUBES are described in section 3. The results are presented and discussed in section 4 and final remarks are made in section 5. We have used throughout the paper $H_0 = 73\,\mathrm{km\,s^{-1}\,Mpc^{-1}}$ (Riess et al. 2022).

2 DATA

The data used here are those provided by the fourth-generation Sloan Digital Sky Survey (SDSS IV) sub-project Mapping Nearby Galaxies at Apache Point Observatory (MaNGA, Bundy et al. 2015). The survey has provided optical IFU spectroscopy (3600 Å-10400 Å), high quality data, of ∼ 10,010 nearby galaxies (with $\langle z \rangle \approx 0.03$). The observations were carried out with fiber bundles of different sizes (19-127 fibers) covering a field of 12″ to 32″ in diameter. MaNGA observations are divided into "primary" and "secondary" targets, the former was observed up to 1.5 effective radius (R_e) while the latter was observed up to 2.5 R_e. For more details, see Drory et al. (2015); Law et al. (2015); Yan et al. (2016a,b).

We have fitted the stellar population and emission lines for the 10 010 high quality unique[1] data cubes available in the MaNGA final data release (DR17, Abdurro'uf et al. 2022; Aguado et al. 2019; Blanton et al. 2017; Bundy et al. 2015; Belfiore et al. 2019; Westfall et al. 2019; Cherinka et al. 2019; Wake et al. 2017; Law et al. 2015, 2016, 2021; Yan et al. 2016b,a; Drory et al. 2015; Gunn et al. 2006; Smee et al. 2013).

2.1 Active Galactic Nuclei and Control Samples in MaNGA

In this work, we update and expand the sample of AGN hosts optically identified in the MaNGA survey by Rembold et al. (2017). We have cross-matched all galaxy data cubes observed in DR17 with the SDSS-III spectroscopic data from DR12 (Alam et al. 2015). The fluxes and equivalent widths of the emission lines Hβ, [O III]λ5007, Hα and [N II]λ6583, measured in the SDSS-III integrated nuclear spectrum, were drawn from Thomas et al. (2013). We then classified the galaxies according to the ionizing source of the gas using both the [N II] based Baldwin et al. (1981, BPT) diagram[2]. and the WHAN diagram (Cid Fernandes et al. 2010), following Rembold et al. (2017). A galaxy is confirmed as an optical AGN host if it is located simultaneously in the Seyfert/LINER region of both the BPT and the WHAN diagrams. We refer to Rembold et al. (2017) for more details on the selection of AGN hosts. This methodology results in 298 confirmed optical AGN hosts in MaNGA.

As in Rembold et al. (2017), we have defined a sample of non-active control galaxies comparable to the AGN hosts in terms of redshift, stellar mass and morphology. We selected from DR17, as potential control galaxies, those presenting or not detectable emission lines in their SDSS-III fiber spectra, except those already classified as AGN hosts (see above). Besides the objects lacking detectable emission lines altogether, potential control galaxies are those located, within the uncertainties, in the star-forming region of the BPT diagram, or in other regions of the BPT diagram if the WHAN diagram discards ionization from an AGN. These comprise therefore objects ionized by young stars or by hot, low-mass evolved stars (HOLMES). For each AGN host, we then select a preliminary subsample of galaxies from the list of potential control objects that match their redshifts and stellar masses at deviations lower than 30 percent deviation. Such preliminary galaxies (typically a couple hundred for each AGN host) were then visually inspected, and the two objects that best match the morphology and axial ratio of the AGN host were selected as their control "partners". For five AGN hosts (MaNGA id 1-37440, 1-189584, 31-115, 1-641156 and 1-300461), no control "partners" were selected, either because their redshifts are too close to the redshift limits of the MaNGA survey (e.g. 1-189584 at $z = 0.0037$) or because their morphologies are not reproduced by other objects in the survey (e.g. 1-641156).

Our final sample is therefore composed of 293 AGN hosts paired with two non-active control galaxies each. The control sample comprises 492 unique objects, less than the expected 586, due to multiple occurrences of the same control galaxy as control "partners" of more than one AGN host. Table 1 and Table 2 list relevant parameters of the AGN hosts and control galaxies respectively.

As a verification of the quality of the control sample selection

---

[1] We have discounted the Coma, IC342, M31, and globular cluster targets, and cubes with "UNUSUAL" or "CRITICAL" data quality flags, as well as repeated observations.

[2] It is worth mentioning that this diagram identify LINERs that would be missed by other diagrams (Agostino et al. 2021)

process, we confirmed using the Kolmogorov-Smirnov test that the distributions of stellar mass and redshift are indistinguishable between AGN hosts and control galaxies. We show the distribution of redshift, stellar mass, stellar velocity dispersion, and [O III] luminosity in Fig. 1. Also, according to the Galaxy Zoo project (Lintott et al. 2011), 32%, 60% and 5% of our AGN hosts are elliptical, spiral, and merging galaxies respectively. This morphological distribution is well matched by the control sample, comprised of 35%, 61% and 2% of elliptical, spiral and merging galaxies respectively. We have also compared the numerical T-Type between AGN hosts and control galaxies from Vázquez-Mata et al. (2022) and found that both distributions are very similar (and indistinguishable as verified using the Kolmogorov-Smirnov test). For more details on the control sample selection see Rembold et al. (2017).

3 FITTING PROCEDURES

3.1 Stellar Population

In this section, we describe the procedures adopted in the stellar population fits.

3.1.1 *Starlight*

To perform a full spectral fitting stellar population synthesis on our datacubes we employed the STARLIGHT code (Cid Fernandes et al. 2005; Cid Fernandes 2018) which combines the spectra of a *base of elements* of $N_\star$ simple stellar population (SSP) template spectra $b_{j,\lambda}$, weighted in different proportions, in order to reproduce the observed spectrum O_λ. For this modeling, the observed and modeled spectra M_λ are normalized at a user-defined wavelength λ_0. The reddening is given by the term $r_\lambda = 10^{-0.4(A_\lambda - A_{\lambda_0})}$, weighted by the population vector x_j (which represents the fractional contribution of the jth SSP to the light at the normalisation wavelength λ_0), and convolved with a Gaussian distribution $G(v_\star, \sigma_\star)$ to account for velocity shifts $v_\star$, and velocity dispersion $\sigma_\star$. Each model spectra can be expressed as:

$$M_\lambda = M_{\lambda_0}\left[\sum_{n=1}^{N_\star} x_j\, b_{j,\lambda}\, r_\lambda\right] \otimes G(v_\star, \sigma_\star), \qquad (1)$$

where M_{λ_0} is the flux of the synthetic spectrum at the wavelength λ_0. To find the best parameters for the fit, the code searches for the minimum of $\chi^2 = \sum_{\lambda_i}^{\lambda_f}[(O_\lambda - M_\lambda)\omega_\lambda]^2$, where ω_λ is the inverse of the error, using a simulated annealing plus Metropolis scheme.

The *base of elements* we use is the GM described in Cid Fernandes et al. (2013, 2014) that is constructed using the MILES (Vazdekis et al. 2010) and González Delgado et al. (2005) models. We have updated it with the MILES V11 models (Vazdekis et al. 2016). We used 21 ages (t= 0.001, 0.006, 0.010, 0.014, 0.020, 0.032, 0.056, 0.1, 0.2, 0.316, 0.398, 0.501 0.631, 0.708, 0.794, 0.891, 1.0, 2.0, 5.01, 8.91 and 12.6 Gyr) and four metallicities (Z= 0.19, 0.40, 1.00 and 1.66 $Z_\odot$). Following Cid Fernandes et al. (2004) we have also added to the *base of elements* a power law of the form $F_\nu \propto \nu^{-1.5}$ to account for the contribution of a possible AGN featureless continuum (FC), observed directly or as scattered light (see also Koski 1978; Cid Fernandes et al. 2005; Martins et al. 2013; Riffel et al. 2009, 2021a, 2022, for discussion on the FC contribution). It is worth mentioning that FC is only considered in the light fractions being removed from the calculations of stellar properties (e.g. mean ages and metallicities, see § 3.1.3).

Finally, the normalization flux at λ_0 was adopted to be the mean value between 5650Å and 5750Å. The reddening law we used was that of Cardelli et al. (1989) and the synthesis was performed in the spectral range from 3700 Å to 6900 Å.

3.1.2 *Urutau*

STARLIGHT is not developed to work with datacubes or *fits* files, therefore we have developed an in house software: URUTAU. It was developed in Python to handle input and output data from multiple sources via a modular pipeline execution. The modules of the pipeline can be swapped depending on the user case (such as datacube extraction method, spectral fitting software, desired scientific result, etc.). URUTAU was also planned with parallel processing capability in order to execute many instances of a closed source executable (such as STARLIGHT) for different sets of data. The code is available at: `https://github.com/ndmallmann/urutau`.

3.1.3 *Stellar population* MEGACUBE *modules*

To improve the management of the STARLIGHT inputs and outputs, the organization of the results and the analysis, we developed a series of modules to run under URUTAU and appended the data-products to the original datacube. These modules are as follows:

a) LIBMANGA: This library is used to prepare and convert the MaNGA datacubes to the format expected by STARLIGHT. The main steps are as follows (Mallmann et al. 2018) :

(i) Filtering of the datacubes using a two-dimensional butterworth filter to remove spurious data and increase the signal-to-noise ratio. It does not require any addition of adjacent spaxel, thus allowing to a better exploration of the spatial resolution. A better description of this technique can be found in Riffel et al. (2016);

(ii) Correct each spaxel for Galactic reddening using the Schlegel et al. (1998) extinction maps and the Cardelli et al. (1989) reddening law;

(iii) Correct for redshift using the SDSS-III redshift values available in the *drpall* tables of the MaNGA database;

(iv) Estimation of the signal-to-noise ratio (SNR) maps in the wavelength range 5650-5750 Å for every spaxel. We provide masks with cuts of SNR values of 3, 5, and 10, as well as the SNR map. We have performed our fits for spaxels with SNR≥1. Note, however, that any cutoff in SNR larger than 1 can be applied by the user since we provide the SNR maps.

b) LIBSTARLIGHTCALLER: This module is used to actually run STARLIGHT with the configuration listed in § 3.1.1. In other words, it sets up all the configuration files needed for the fits and runs STARLIGHT for each individual spaxel.

c) LIBCREATEMEGACUBE: With this function we derive additional parameters like: mean ages and metallicities, star formation rates, and binned population vectors from the starlight output as follows:

Binned population vectors: Since small differences in ages are washed away due to noise effects, one coarser, but more robust way is to define binned population vectors (e.g. Cid Fernandes et al. 2005; Riffel et al. 2009). We included in our MEGACUBES the following binned population vectors (where y=young, i=intermediate, and o=old):

FC1.50: The percent contribution (at λ_0) of a featureless component of the form $F_\nu \sim \nu^{-1.5}$;

xyy_light (mass): Light (mass) binned population vector in the age range $t \leq 10$ Myr;

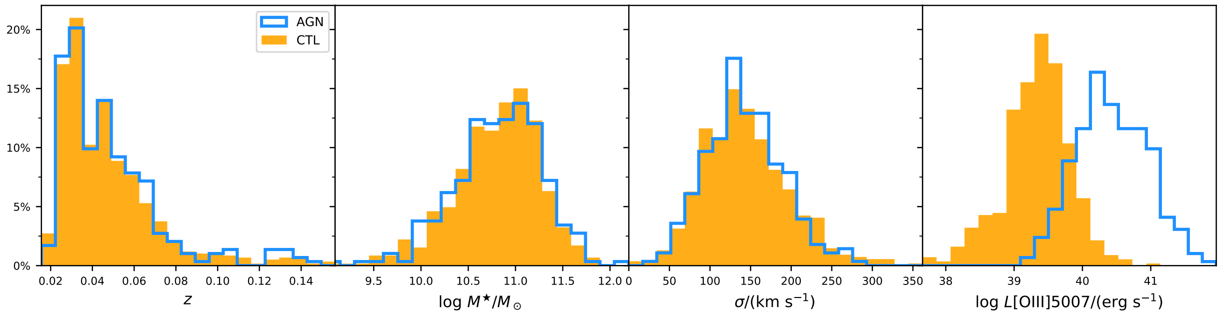

Figure 1. Distributions of redshift, stellar mass, stellar velocity dispersion, and [O III] luminosity of the AGN host sample (blue) and the control sample (orange). These properties are from SDSS single fiber observations. The AGN and the control sample present markedly different distributions of L([O III]), which is expected (see Rembold et al. 2017, for a discussion), but have other parameters similar between the two samples.

Table 1. Parameters of AGN in MaNGA-DR17. (1) galaxy identification in the MaNGA survey; (2)-(3): RA/DEC (2000) in degrees; (4) spectroscopic redshift from SDSS-III; (5): integrated absolute r-band magnitude from SDSS-III; (6): logarithmic stellar mass in units of $M_\odot$; (7)-(8) morphological classification in the Hubble scheme and numerical T-Type from Vázquez-Mata et al. (2022); (9): [OIII] luminosity in units of 10^{40} erg s^{-1}. We only present here the first 6 lines of this table; the full version is available with the electronic version of the paper.

mangaID (1)	RA (2)	DEC (3)	z (4)	M_r (5)	log $M^\star/M_\odot$ (6)	Type (7)	T-Type (8)	$L([\text{OIII}])$ (9)
1-558912	166.129410	42.624554	0.1261	-20.46	11.25	E	-5	56.82±1.25
1-150947	183.263992	51.648598	0.0849	-20.23	10.96	Sb	3	53.82±1.75
1-39376	11.999101	13.742678	0.0567	-19.76	10.92	SBb	3	43.88±0.65
1-295542	246.255981	24.263155	0.0503	-19.34	10.73	Edc	-5	39.10±0.87
1-458092	203.190094	26.580376	0.0470	-18.08	9.64	E	-5	35.30±1.04
1-211165	248.628647	37.695442	0.0991	-21.04	11.24	S0	-2	33.83±0.57

Table 2. Control sample parameters. (1) identification of the AGN host associated to the control galaxy; (2)-(10) same as (1)-(9) of Table 1 for the control sample. We only present here the first 12 lines of this table; the full version is available with the electronic version of the paper.

AGN mangaID (1)	mangaID (2)	RA (3)	DEC (4)	z (5)	M_r (6)	log $M^\star/M_\odot$ (7)	Type (8)	T-Type (9)	$L([\text{OIII}])$ (10)
1-558912	1-71481	117.456001	34.883911	0.1312	-20.95	11.70	E	-5	0.10±0.20
	1-72928	127.256485	45.016773	0.1270	-20.62	11.52	E	-5	0.09±0.23
1-150947	1-338555	114.374146	41.737232	0.0893	-17.42	8.99	E	-5	2.05±0.39
	1-248214	240.347031	43.085041	0.0600	-19.80	10.97	Edc	-5	0.41±0.14
1-39376	1-285052	199.061493	47.599365	0.0573	-19.77	10.85	SBab	2	0.11±0.03
	1-283662	191.217728	42.422195	0.0536	-19.27	10.66	SB0a	0	0.00±0.00
1-295542	1-94228	248.018265	47.764759	0.0494	-19.19	10.58	Sa	1	0.30±0.06
	1-92774	243.407715	49.069408	0.0552	-19.28	10.75	Edc	-5	0.39±0.23
1-458092	1-38319	51.609463	-0.311706	0.0376	-17.24	9.76	Edc	-5	0.00±0.00
	1-323888	245.686630	32.659161	0.0410	-18.64	9.54	S0	-2	11.66±0.31
1-211165	1-55272	146.661270	2.658917	0.0933	-20.90	11.49	S0	-2	1.24±0.27
	1-262966	229.138367	32.243935	0.0913	-20.79	11.22	Edc	-5	0.16±0.16

xyo_light (mass): Light (mass) binned population vector in the age range 14 Myr < $t \leq$ 56 Myr;

xiy_light (mass): Light (mass) binned population vector in the age range 100 Myr < $t \leq$ 500 Myr;

xii_light (mass): Light (mass) binned population vector in the age range 630 Myr < $t \leq$ 800 Myr;

xio_light (mass): Light (mass) binned population vector in the age range 890 Myr < $t \leq$ 2.0 Gyr;

xo_light (mass): Light (mass) binned population vector in the age range 5.0 Gyr < $t \leq$ 13 Gyr;

Star Formation Rates via stellar population fit: the star formation rate obtained from the stellar population fit ($SFR_\star$) over an user-defined age interval ($\Delta t = t_{j_f} - t_{j_i}$) is also computed in this module. This can be computed since the SSPs model spectra are in units of L$_\odot$ Å$^{-1}M_\odot^{-1}$, and the observed spectra (O_λ) are in units of erg/s/cm^2/Å. The SFR$_\star$ over the chosen Δt can be computed assuming that the mass of each base component (j) which has been processed into stars can be obtained as:

$$M^{\text{ini}}_{\star,j} = \mu^{\text{ini}}_j \times \frac{4\pi d^2}{3.826 \times 10^{33}}, \tag{2}$$

where $M^{\text{ini}}_{\star,j}$ is given in $M_\odot$, μ^{ini}_j is associated with the mass that has been converted into stars for the j-th element and its flux. This parameter is given in $M_\odot$ $\mathrm{ergs}^{-1}\mathrm{cm}^{-2}$; d is the luminosity distance to the galaxy in cm and 3.826×10^{33} is the Sun's luminosity in $\mathrm{erg\,s}^{-1}$. Thus, the SFR over the Δt as defined above can be obtained from the equation:

$$\mathrm{SFR}_\star = \frac{\sum_{j_i}^{j_f} M^{\mathrm{ini}}_{\star,j}}{\Delta t}. \tag{3}$$

For more details see Riffel et al. (2021a). Here we computed the $\mathrm{SFR}_\star$ over the last (Δt) 1 Myr, 5.6 Myr, 10 Myr, 14 Myr, 20 Myr, 32 Myr, 56 Myr, 100 Myr, and 200 Myr (they were labelled as SFR_1, SFR_5, SFR_10, SFR_14, SFR_20, SFR_30, SFR_56, SFR_100, and SFR_200, respectively).

Mean ages and metallicities: Following Cid Fernandes et al. (2005) we have computed the mean ages (the logarithm of the age, actually) for each spaxel weighted by the stellar light

$$\langle \log t_\star \rangle_L = \sum_{j=1}^{N_\star} x_j \log t_j, \tag{4}$$

and weighted by the stellar mass,

$$\langle \log t_\star \rangle_M = \sum_{j=1}^{N_\star} \mu_j \log t_j. \tag{5}$$

The light-weighted mean metallicity is defined as

$$\langle Z_\star \rangle_L = \sum_{j=1}^{N_\star} x_j Z_j, \tag{6}$$

and the mass-weighted mean metallicity is defined by:

$$\langle Z_\star \rangle_M = \sum_{j=1}^{N_\star} \mu_j Z_j. \tag{7}$$

Note that both definitions are limited by the age and metallicities range used in our elements base. They are presented under the *Mage_L, Mage_M, MZ_L,* and *MZ_M* keywords.

Additional parameters: we also present a set of additional fitting parameters that are included in the MEGACUBES, such as optical extinction (Av), the present mass in stars (M*), masses processed in stars (M*in), normalisation flux (F_Norm), stellar dispersion velocity (Sigma_star), stellar rotation velocity (vrot_star), percentage mean deviation (Adev), reduced χ^2 (ChiSqrt), and signal-to-noise ratio on normalisation window (SNR).

The final product after the procedures described above is a complete set of Flexible Image Transport System (FITS) files for the entire MaNGA sample; this constitutes what we refer to as MEGACUBES. The results obtained after our fitting are appended as multiple extensions into the original MaNGA datacubes. The additional extensions added are as follows:

BaseAgeMetal: The ages and metallicities of the SSPs used in the base of elements.

PopBins: In this extension we store the synthesis parameters directly computed by STARLIGHT as well as properties derived in the LIBCREATEMEGACUBE module (see § 3.1.3)

PoPVecsL (M): Original (e.g. not binned) population vectors in light fractions (mass fractions).

The STARLIGHT output observed flux (FLXOBS), synthetic flux (FLXSYN), and weights (WEIGHT), as well as continuum signal-to-noise ratio masks, are also stored on the MEGACUBES.

3.2 Emission line fitting

Our MEGACUBES, by construction, include absorption-free emission-line datacubes. We have used these datacubes to fit the most common emission lines in the optical region. To this purpose we use the IFSCUBE[3] Python package (Ruschel-Dutra 2020; Ruschel-Dutra et al. 2021) to fit the profiles of the most prominent emission-line, namely: Hβ, [O III]$\lambda\lambda$4959,5007, He Iλ5876, [O I]λ6300, Hα [N II]$\lambda\lambda$6548,6583 and [S II]$\lambda\lambda$6716,6731. The line profiles are fitted with Gaussian curves by adopting the following constraints: (i) the width and centroid velocities of emission lines from the same parent ion are constrained to the same value, just He Iλ5876 and [O I]λ6300 are kept free during the fit; (ii) the [O III]λ5007/λ4959 and [N II]λ6583/λ6548 flux ratios are fixed to their theoretical values of 2.98 and 3.06, respectively; (iii) the centroid velocity is allowed to vary from –300 to 300 $\mathrm{km\,s}^{-1}$ for [S II] lines and –350 to 350 $\mathrm{km\,s}^{-1}$ for the other lines relative to the velocity obtained from the redshift of each galaxy (listed in the MaNGA Data Analysis Pipeline - DAP); and (iv) the observed velocity dispersion of all lines is limited to the range 40–300 $\mathrm{km\,s}^{-1}$. In a few sources better fits of the observed profiles are obtained when including a broad component for Hα and Hβ[4]. In addition, we include a first-order polynomial to reproduce the local continuum.

Instead of relying on the minimization of a residual function, kinematic constraints were enforced by construction, as each emission line in the same kinematic group inherits the same exact parameter for line width and centroid velocity, see Ruschel-Dutra et al. (2021) for additional details. Additionally, all the lines have been fitted with a single Gaussian. This approach has the advantage of reducing the number of free parameters that are perceived by the fitting algorithm.

The output of IFSCube is in the form of a Multi-Extension FITS file (MEF), with each extension storing a different result from the fitting process, a copy of the input, or software-specific parameters for later reference. The first four extensions are in the same shape of the input data, "FITSPEC" representing the observed spectra (restricted to the requested wavelength window), the result of the pseudo continuum fit is in "FITCONT", "STELLAR" stores the given stellar spectra and "MODEL" stores the modelled emission spectrum. If no stellar spectra were given as input, the corresponding extension is filled with zeros.

Next there is the "SOLUTION" extension which stores the best parameters for all the emission lines considered, and also the reduced chi-squared of the model as a whole. The shape is that of the input data for the spatial part, with each parameter occupying a different plane. For instance, if three Gaussian curves were fit to a 50x50 data cube, then there should be 9 independent parameters for the whole model, and another plane for the chi-squared, resulting in a 50x50x10 array.

The initial guess for each parameter is stored in the "INIGUESS" extension, also in the form of a three-dimensional array, with a set of parameters for each spaxel. This is useful only when using the option to update the initial guess based on results from previous spaxels. Extensions 7 through 10 ("FLUX_D", "FLUX_M", "EQW_M" and "EQW_D") store the fluxes and equivalent widths of each line, using two different approaches. The first one is a direct trapezoidal

---

[3] https://github.com/danielrd6/ifscube

[4] No changes in the activity classification are found when a broad component is included since, even in cases where a broad component is evident, the line fluxes are well represented by a single component. For completeness, we have made available the MEGACUBES for these sources with and without the broad component.

integration of the observed spectra, minus the stellar component and pseudo-continuum, while the second is an integration over the modelled emission line. The final status of each spaxel is specified by an integer code and stored in the "STATUS" extension. A bi-dimensional mask, which combines both the input mask and IFSCube's internal assessment of the spaxel quality, is stored in the extension "MASK2D".

The last three extensions are tables, as opposed to all the previous ones which consist of images. Extension "SPECIDX" stores the sequence in which the spaxels were processed. Parameter names in the exact order that they apper in the "SOLUTION" extension are specified by the table in the "PARNAMES" extension. Finally, the "FITCONFIG" extensions keeps a copy of the input configuration.

All these extensions regarding the emission line fitting have been appended to the MEGACUBES.

4 RESULTS AND DISCUSSION

4.1 MEGACUBES

As described in the previous sections we have fitted the stellar population and derived their properties for $\sim 10\,000$ galaxies, being thus the main purpose of this paper to make available for the community, in an easy-to-use way, the maps of the stellar population and emission lines of all spaxels on the ~10 thousand MaNGA datacubes. This final product is what we call MEGACUBES.

In order to facilitate the inspection of the large number of properties that can be derived from the analysis of the spectra available in the IFU data cube, a customized viewer was developed in collaboration with LIneA's IT team. All the MEGACUBES are available through a web interface (`https://manga.linea.org.br/` or `http://www.if.ufrgs.br/~riffel/software/megacubes/`), where each one of them can be downloaded and/or inspected via a number of different plots, which can be interacted with. Additionally, we do also provide a table with the mean or integrated values (integrated for $M\star$ and emission-line fluxes) of the circularised maps for many properties for all the galaxies for different radial values as follows[5]: R_INT_0 = R< $0.5\,R_e$; R_INT_1 = $0.5\,R_e$ $\leq$ R< $1.0\,R_e$; R_INT_2 = $1.0\,R_e$ $\leq$ R< $1.5\,R_e$, R_INT_3 = $1.5\,R_e$ $\leq$ R< $2.0\,R_e$; R_INT_4 = R< 0.5 kpc; R_INT_5 = 0.5 kpc $\leq$ R< 1.0 kpc; R_INT_6 = 1.0 kpc $\leq$ R< 2.0 kpc; R_INT_7 = 2.0 kpc $\leq$ R< 5.0 kpc, and R_INT_8 = 5.0 kpc $\leq$ R< 10.0 kpc. These mean/integrated properties have been derived considering the values where the continuum SNR$\geq$10 (SN_MASKS_10) and, for the emission-line related properties we have considered an additional threshold of $\geq 3\sigma$ detection.

As a highlight of the science that can be done with these MEGACUBES, we analyze here the stellar populations and the spatially resolved emission-line diagnostic diagrams of the final set of AGNs on the MaNGA survey and compare them with the results obtained for the control sample we have described in § 2.1.

4.2 Mapping the stellar populations in MaNGA AGNs

The MEGACUBES have a large number of output parameters, but here we are mostly interested in x_j – the fractional contribution of each SSP to the total light at λ_{norm} – as they represent the star formation history of the galaxy. Following Mallmann et al. (2018), we show example maps of these parameters, together with the mean age and the reddening maps in Fig. 2 (late-type AGN) and Fig. 3 (early-type AGN). It is worth mentioning that we have changed the methodology applied in Mallmann et al. (2018) for the computation of the profiles using a circularized deprojection over the entire FoV, instead of only a region along the major axis of the galaxies as in Mallmann et al. (2018).

4.2.1 2D maps analysis

In order to show in a qualitative way how the different stellar population components are distributed along the FoV we have constructed RGB images (Figs. 2 and 3) of the galaxies that were created by assigning three colors (Red, Green, and Blue) to the binned population vectors: Red represents the old (xo: 5 Gyr $< t \leq$ 13 Gyr), green the intermediate age (xiy+xii+xio = xi: 100 Myr $< t \leq$ 2 Gyr), and blue the young (xyy+xyo = xy: $t \leq$56Myr) stellar populations (see § 3.1.3 for the age bin definitions). We also show (left side) the maps for the mean properties and the radial profiles (right side) of these properties. In addition, we show the mean gradient values in 3 different radial steps (0.0 to 0.5R$_e$, 0.5 to 1.0R$_e$, and 0.0 to 1.0 R$_e$). These gradients have been computed by linear regression over the points within the radial steps and the values quoted are the angular coefficients for the AGN and for the two controls galaxies.

From this exercise, one can see that the old population is more centrally concentrated in the late-type sources, while the gradient is shallower in the early-type ones, but in both cases, a decreasing value is observed with increasing radius. In addition, both types show significant contributions of the intermediate age with an outwards increasing gradient, while the young component is distributed along the full FoV. This behavior is seen for almost all sources in our sample (see supplementary material for the figures for the other galaxies).

4.2.2 Gradients

The quantitative comparison of individual sources is very difficult, and therefore we show the general behaviour of the stellar population parameters along the galaxies and the comparison between AGN and controls. We show their variations with radii and with [O III] luminosity from Fig. 4 to Fig. 8. The L([O III]) bins where taken from Rembold et al. (2017). We have also separated the sample into early- and late-type galaxies. The Hubble types were taken from Vázquez-Mata et al. (2022) and are listed in Tab. 1. We have classified the sources with the parameter T-Type $\leq$ 2 as early-type and with 2< T-Type < 10 as late-type, while objects with T-Type $\geq$ 10 were classified as Irregular and are not used in our analysis.

What clearly emerges from this choice is that for the younger ages (t <56 Myr) no differences are detected when comparing AGNs hosts and control galaxies. However, when focusing on R < 0.5 R$_e$ the values for this component seem to be biased towards a slight increase on the mean values for AGN hosts with higher [O III] luminosity, when compared to their corresponding control galaxy counterparts. In addition, this component's contribution is generally low ($\lesssim$ 10 percent) with the possible difference between AGNs and controls being around 2 percent and within the uncertainties. For the less luminous AGNs a positive gradient is seen, while a slightly negative

---

[5] We call attention to the equivalent width values since they are the mean value of the different strengths measured over the field. They should be taken as an upper limit: spaxels containing emission lines below the detectability limit contribute only to the continuum, thus reducing the total line flux, while in an integrated spectrum over the same field these "spaxels" contribute also to the line flux.

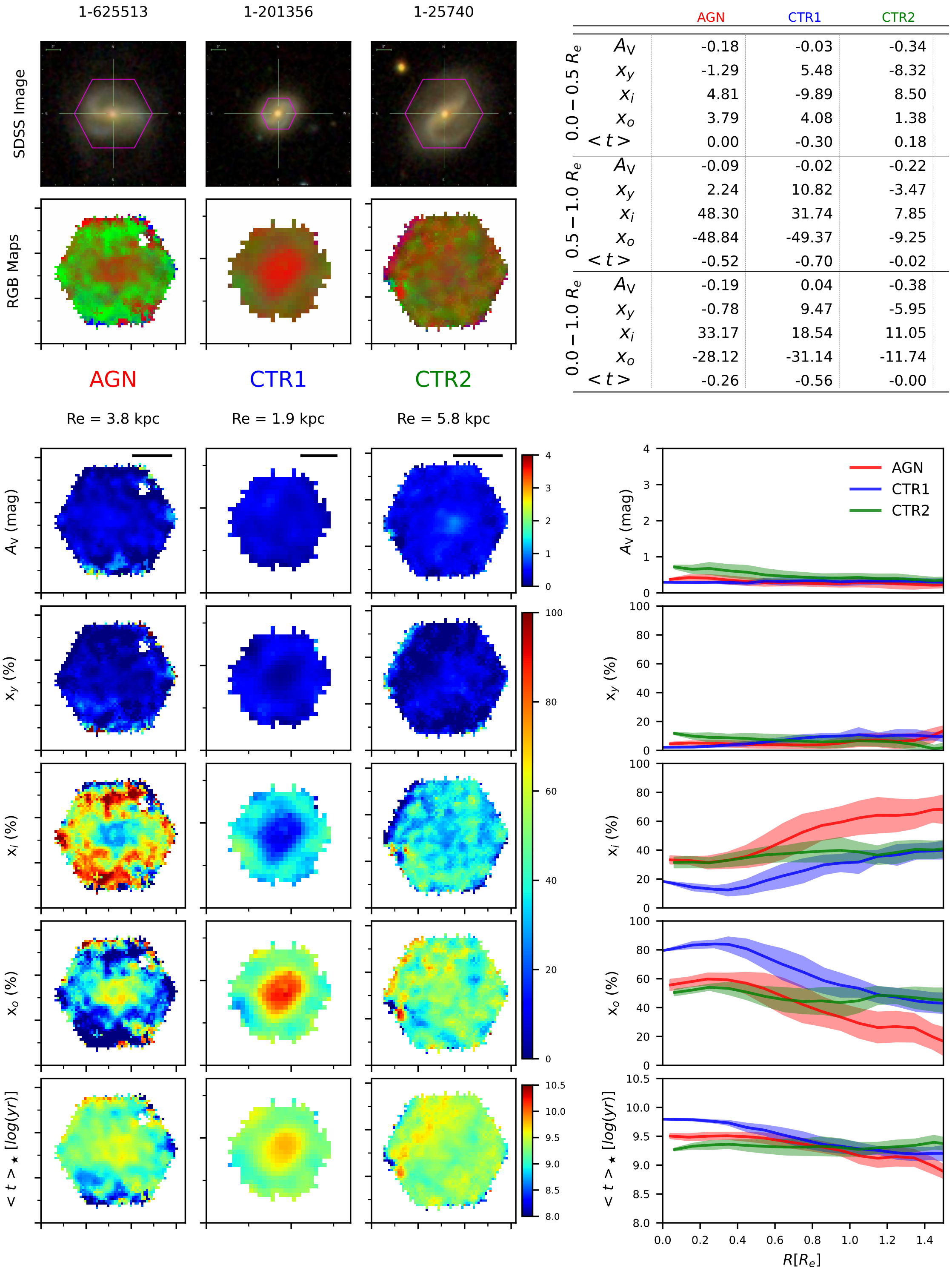

		AGN	CTR1	CTR2
$0.0 - 0.5\ R_e$	A_V	-0.18	-0.03	-0.34
	x_y	-1.29	5.48	-8.32
	x_i	4.81	-9.89	8.50
	x_o	3.79	4.08	1.38
	$< t >$	0.00	-0.30	0.18
$0.5 - 1.0\ R_e$	A_V	-0.09	-0.02	-0.22
	x_y	2.24	10.82	-3.47
	x_i	48.30	31.74	7.85
	x_o	-48.84	-49.37	-9.25
	$< t >$	-0.52	-0.70	-0.02
$0.0 - 1.0\ R_e$	A_V	-0.19	0.04	-0.38
	x_y	-0.78	9.47	-5.95
	x_i	33.17	18.54	11.05
	x_o	-28.12	-31.14	-11.74
	$< t >$	-0.26	-0.56	-0.00

Figure 2. Comparison of the stellar population properties between a late-type AGN and its controls. **Left side panels -** *Top set of panels:* SDSS image (the MaNGA field is indicated in magenta). Second row: RGB image using a composition of the binned population vectors [blue: young (xyy+xyo = xy); green: intermediate age (xiy+xii+xio = xi); red: old (xo)]. *Bottom set of panels:* From top to bottom: visual extinction (A_V), X_Y, X_I, X_O and mean age ($< t >$) maps. For display purposes, we used tick marks separated by 5”. The solid horizontal line in the A_V maps represents 1 R_e. **Right side panels -** *Top:* summary table with the mean gradient values for each property in 3 different R_e ranges. *Bottom:* average radial profiles for AGN hosts (red) and control galaxies (blue and green). The units of these profiles are the same as in the maps on the left side. The shaded area represents 1 σ standard deviation. This figure is similar to those of Mallmann et al. (2018), but the profiles presented here have been calculated using new circularised deprojected maps.

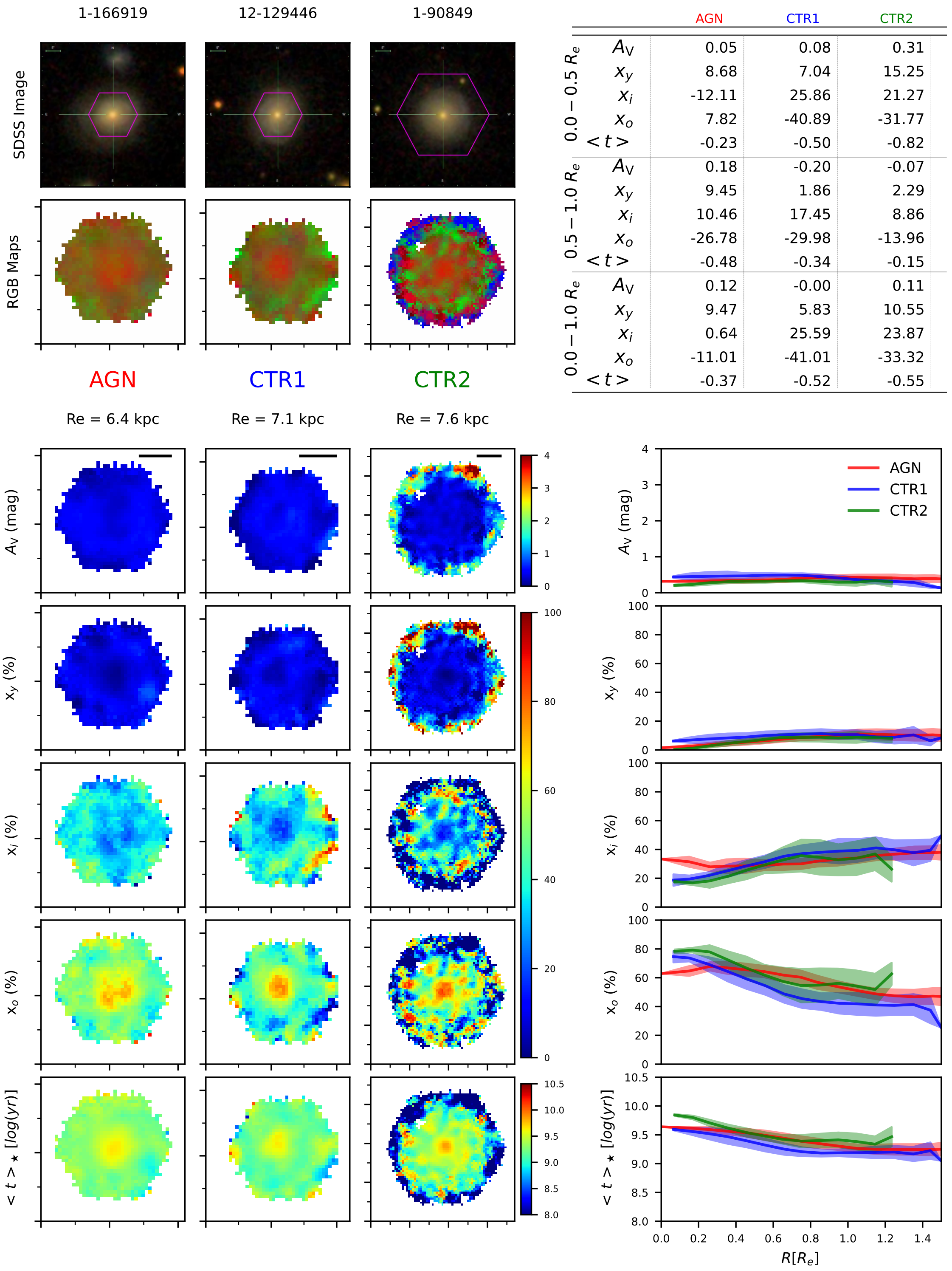

		AGN	CTR1	CTR2
$0.0-0.5\ R_e$	A_V	0.05	0.08	0.31
	x_y	8.68	7.04	15.25
	x_i	-12.11	25.86	21.27
	x_o	7.82	-40.89	-31.77
	$< t >$	-0.23	-0.50	-0.82
$0.5-1.0\ R_e$	A_V	0.18	-0.20	-0.07
	x_y	9.45	1.86	2.29
	x_i	10.46	17.45	8.86
	x_o	-26.78	-29.98	-13.96
	$< t >$	-0.48	-0.34	-0.15
$0.0-1.0\ R_e$	A_V	0.12	-0.00	0.11
	x_y	9.47	5.83	10.55
	x_i	0.64	25.59	23.87
	x_o	-11.01	-41.01	-33.32
	$< t >$	-0.37	-0.52	-0.55

Figure 3. Same as Fig. 2 but for an early-type AGN and its control galaxies.

gradient is seen for the higher luminosity ones. This suggests that the more luminous AGNs may be facing a rejuvenation when compared with the less luminous ones. However, we call attention to the fact that a reddened young SP can mimic an AGN featureless continuum component (see Cid Fernandes et al. 2004, 2005; Riffel et al. 2009, 2022, for more details), thus, this young component has to be analyzed together whit the FC. In Fig. 5 we show the behavior of the FC component as a function of R and L([O III]). In general, the values are very small ($\lesssim$5 percent), and slightly increase outwards[6]. For the two higher luminosity bins a higher value for FC (of ~10 percent) is seen for R<0.5 R_e , and it becomes quite different than the contributions found for the control sample (~2 percent), which we interpret as due to a true AGN FC contribution, while for the remaining luminosity bins and for larger radii we interpret it as due to a reddened young stellar population.

From Fig. 6 it is clear that there is a significant difference for the intermediate age (100 Myr $< t \leq 2$ Gyr) population between AGN hosts and control galaxies. This difference increases with luminosity and is seen for both early and late-type galaxies. Also, a positive gradient is seen with the contribution of the intermediate population increasing outwards.

When looking at the old component ($t \geq 5$ Gyr), a clear difference between the AGN hosts and their controls is seen, becoming more evident for higher luminosities. A slightly steeper gradient, with the fraction of the old population decreasing with R, is seen in the case of AGN hosts when compared with controls.

The above results can be summarised when we looking how the light-weighed mean age ($< t >_L$, Fig. 8) changes with R. What becomes clear when looking for R$\lesssim$0.5 R_e, is that AGN hosts become younger as the AGN luminosity increases (for both, Early and Late-type sources), but, the mean ages are smaller for AGN hosts over R values up to 1.75 R_e, indicating that the stellar population of the host galaxies is affected by the nuclear activity. In addition, a negative gradient of $< t >_L$ with radius is also found, with a flattening for higher AGN [O III] luminosities.

As can be seen from Figs.4 to 8, in general, we observe that the fraction of young and intermediate-age stellar populations increases with the radius, while in the case of the old population, it decreases. These findings are in agreement with previous results (e.g. Sánchez et al. 2013; Ibarra-Medel et al. 2016; Goddard et al. 2017; Mallmann et al. 2018; Sánchez et al. 2021, and references therein). Our results are similar to the results we have obtained for the first 62 AGNs observed by MaNGA (Mallmann et al. 2018). When looking at controls and AGNs, separated between early- and late-type sources, the sense of our gradients are opposed to those found by Goddard et al. (2017). For early-types we derive negative gradients while theirs are slightly positive. The results presented here are in full agreement with those by Ibarra-Medel et al. (2016), who found that the radial stellar mass growth histories of early-type galaxies increase outward, though with a trend much less pronounced than that of their late-type galaxies. The decreasing gradient we observed for the old component suggests that the relative contribution of the more recent star formation increases going outward. Both, early and late-type sources present a significant contribution of the intermediate (~20/40 percent for Early/Late, respectively, for R<0.5 R_e, in light fractions) and young populations (~5/7 percent for Early/Late, respectively, for R<0.5 R_e, in light fractions). This indicates that even in early-type sources residual star-formation is taking place, suggesting that the galaxies are facing a rejuvenation process (e.g. Mallmann et al. 2018; Martín-Navarro et al. 2022) or still forming stars with the gas that they have still available (e.g. they have not finished their SF over cosmic time, see Eales et al. 2017; Dimauro et al. 2022; Paspaliaris et al. 2023, and references), thus they are in fact (predominantly) red and *not* dead sources (Salvador-Rusiñol et al. 2020, 2021; de Lorenzo-Cáceres et al. 2020; Benedetti et al. 2023).

4.2.3 Dependence on the AGN luminosity

In the case of the most luminous AGNs [log(L[O III]:41.25 - 42.00)] the young population contribution seems to rise to higher values for lower radii values. We interpret this as the fact that these AGNs are receiving an extra supply of gas and thus are more luminous. In fact, as shown in Riffel et al. (2022) using high angular resolution observations, found that the inner region of the AGNs is dominated by an intermediate age population ($< t >_L \lesssim$ 1.5 Gyr) and that a correlation between the bolometric luminosity of AGNs with the mean age of their stellar populations is observed in the sense that the more luminous AGNs have larger amounts of intermediate-age stars. This correlation was interpreted as due to a delay between the formation of new stars and the triggering/feeding of the AGN. These intermediate-age stars do provide (via mass loss through stellar evolution) an extra amount of gas that will reach the supermassive black hole (SMBH). Such gas has a low velocity (a few hundred km s^{-1}) and is accreted together with the gas that is already flowing towards the central region of the host galaxy (e.g. Cuadra et al. 2006; Hopkins 2012; Storchi-Bergmann & Schnorr-Müller 2019). In fact, young to intermediate-age populations are detected in the inner region of galaxies (e.g. Dottori et al. 2005; Davies et al. 2005; Riffel et al. 2007, 2015; Salvador-Rusiñol et al. 2020, 2021; de Lorenzo-Cáceres et al. 2020). Such population is dominated by short-lived stars ($t \simeq 0.2-2$ Gyr; $M \simeq 2-6\,M_\odot$) who do eject a significant amount of material to the nuclear environment. This recycled material can cool down forming new stars (e.g. Salvador-Rusiñol et al. 2020, 2021; de Lorenzo-Cáceres et al. 2020; Benedetti et al. 2023) and/or fuel the SMBH with an extra amount of gas, making the AGN brighter or triggering it. This would explain the fact that the most luminous AGNs in our sample do show larger fractions of this intermediate-age population when compared with their control sources.

4.2.4 The stellar Metallicity

In Fig. 9 we show the mean stellar metalicity. Overall, the trend for both the AGN hosts and control galaxies shows a decreasing gradient with increasing radius. A similar behaviour is found by Goddard et al. (2017) and Sánchez (2020), who found a negative gradient for the stellar metallicity for high mass galaxies and positive for low mass ones. For our sample, when all sources are taken together (e.g. left side pannel) the most luminous AGN hosts show a slightly shallower gradient when compared with the controls[7]. Additionally, for regions R $< 0.5\,R_e$ the AGN hosts metallicity is biased towards lower values when compared with the control galaxies and larger radii values. In fact, this is in agreement with the finding of do Nascimento et al. (2022) who derive the gas metallicity (traced by the O/H abundance) of 108 Seyfert galaxies from MaNGA, and found that the inner regions of these galaxies display lower abundances than their outer regions. Additionally, Armah et al. (2023) have shown that the more luminous Seyfert galaxies have lower gas metalicities. However, these results can not be straightforward compared since the gas metallicity is a recent picture of the chemical evolution of the galaxies, while the mean stellar metalicity is a mean over the galaxies'

---

[6] We attribute the increase in the value of FC with R, for both AGNs and controls, as due to an increase of the noise in the spaxels, such that the absorption features are washed away and the FC component becomes hardly distinguishable from the underlying stellar continuum (see Cid Fernandes et al. 2014; Cid Fernandes 2018, and references).

[7] This is in full agreement with the findings of Sánchez (2020), since the AGN luminosity can be taken as a proxy for the galaxy mass (thus the control galaxies for the most luminous AGNs would be more massive).

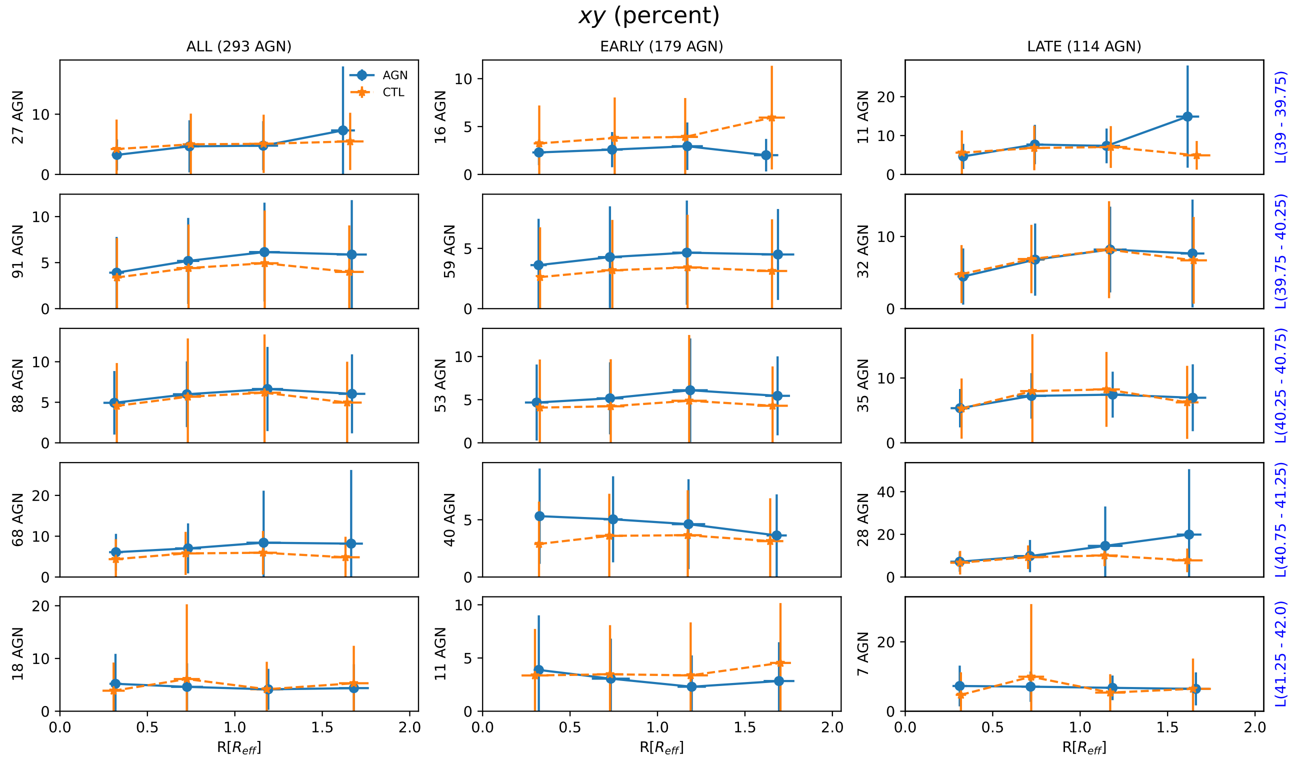

Figure 4. Comparison of the percent contribution to the light at λ_0=5700Å between AGN (blue) and controls (orange) of the young stellar population (xyy+xyo; $t \leq 56$ Myr) percent contribution (in light fractions) for five different luminosity bins (right side: 39-39.75, 39.75-40.25, 40.25-40.75, 40.75-41.25, 41.25-42.0) as a function of the radius expressed in units of R_e. The second and third columns show also the grouping of the galaxies in early and late-type hosts.

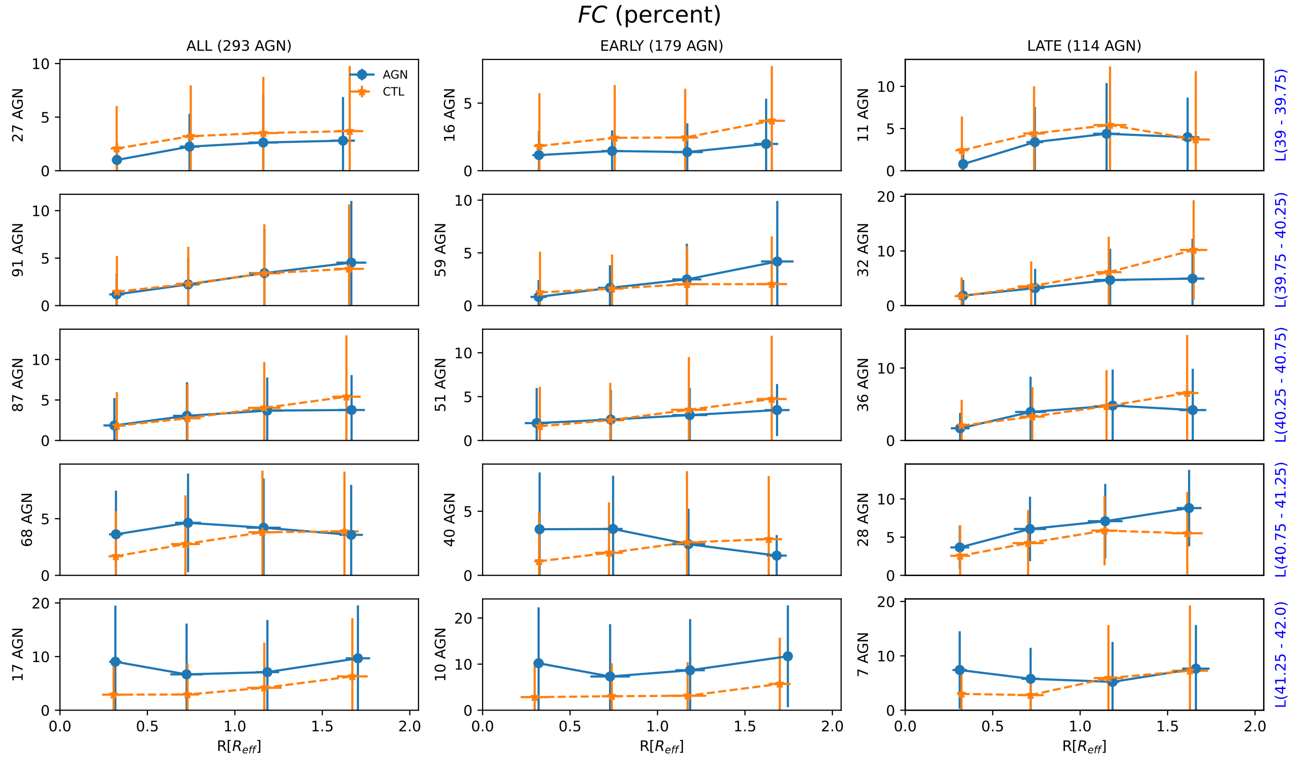

Figure 5. The same as in Fig. 4 but for the featureless continuum component.

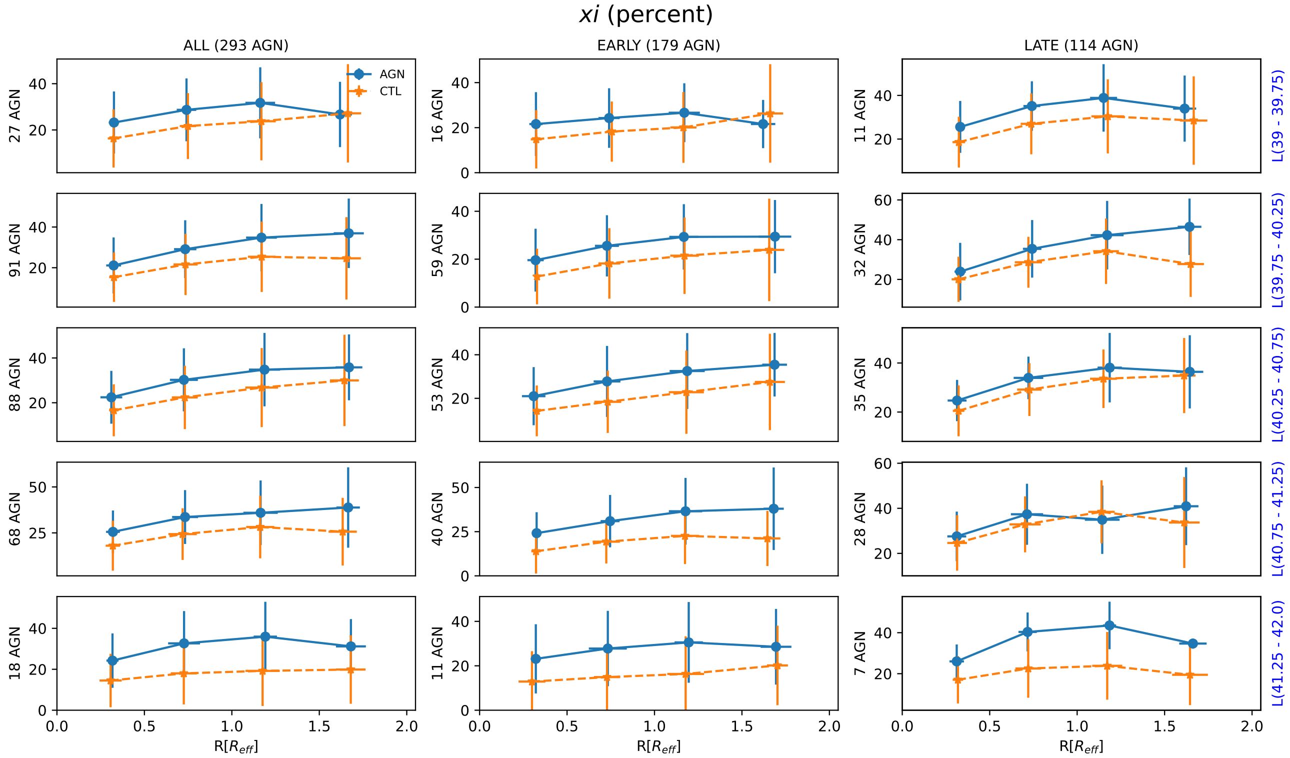

Figure 6. The same as in Fig. 4 but for the intermediate age stellar population (xiy+xii+xio; 100 Myr < t ≤ 2 Gyr) component.

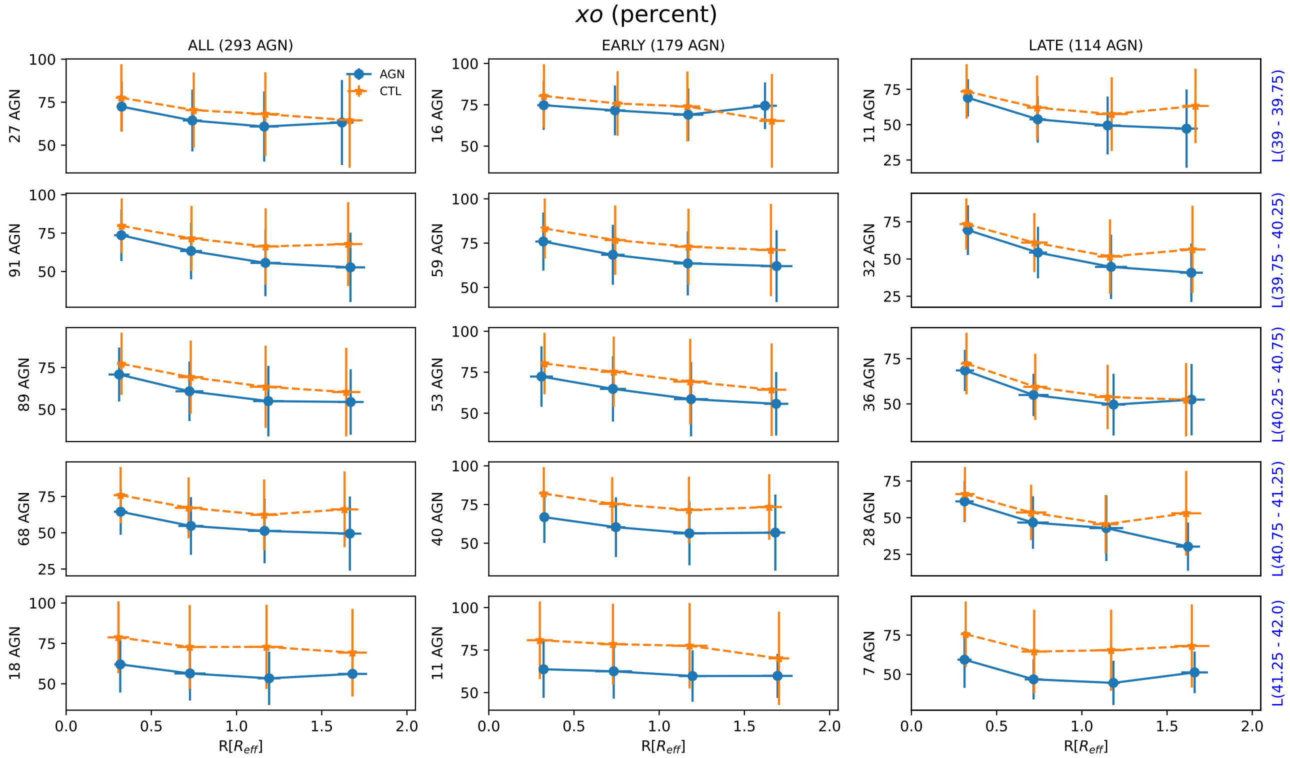

Figure 7. The same as in Fig. 4 but for the xo (5 Gyr < t ≤ 13 Gyr) stellar population component.

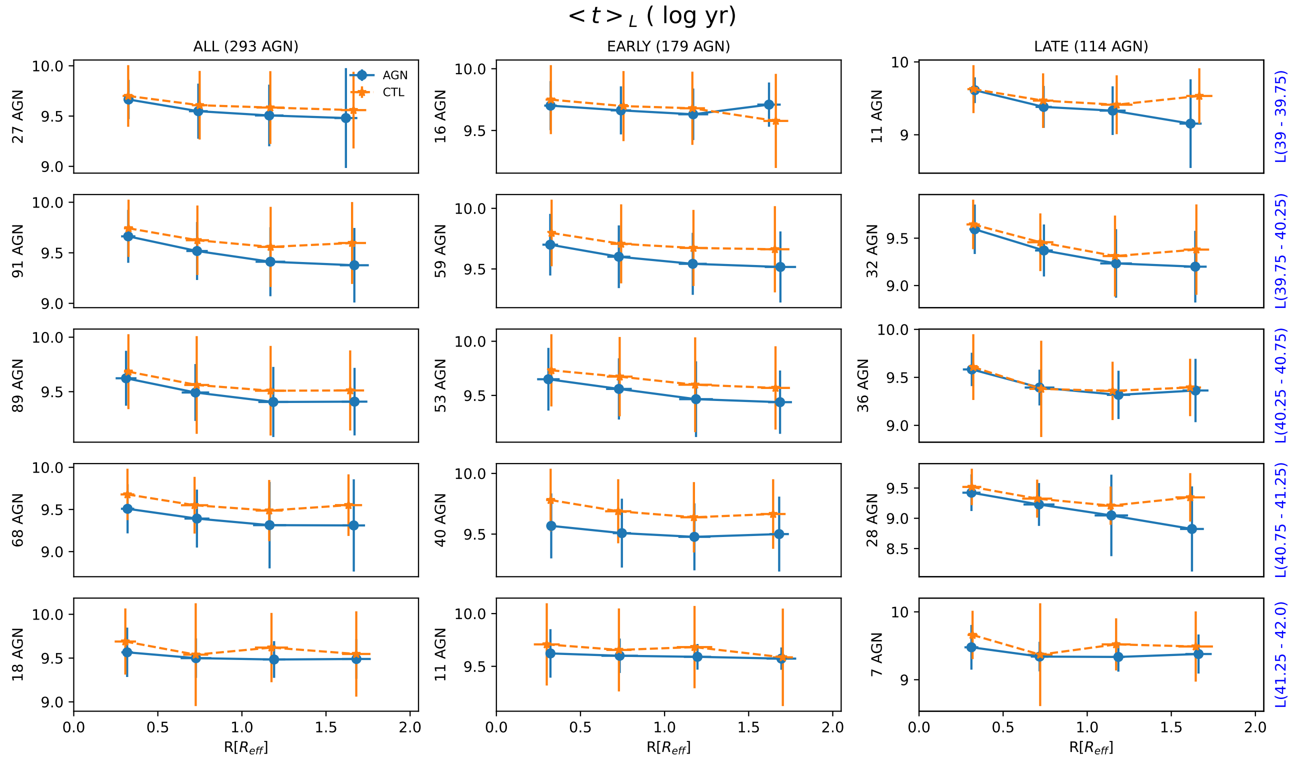

Figure 8. Light-weighted mean age *versus* radius. The labels are the same as in Fig. 4.

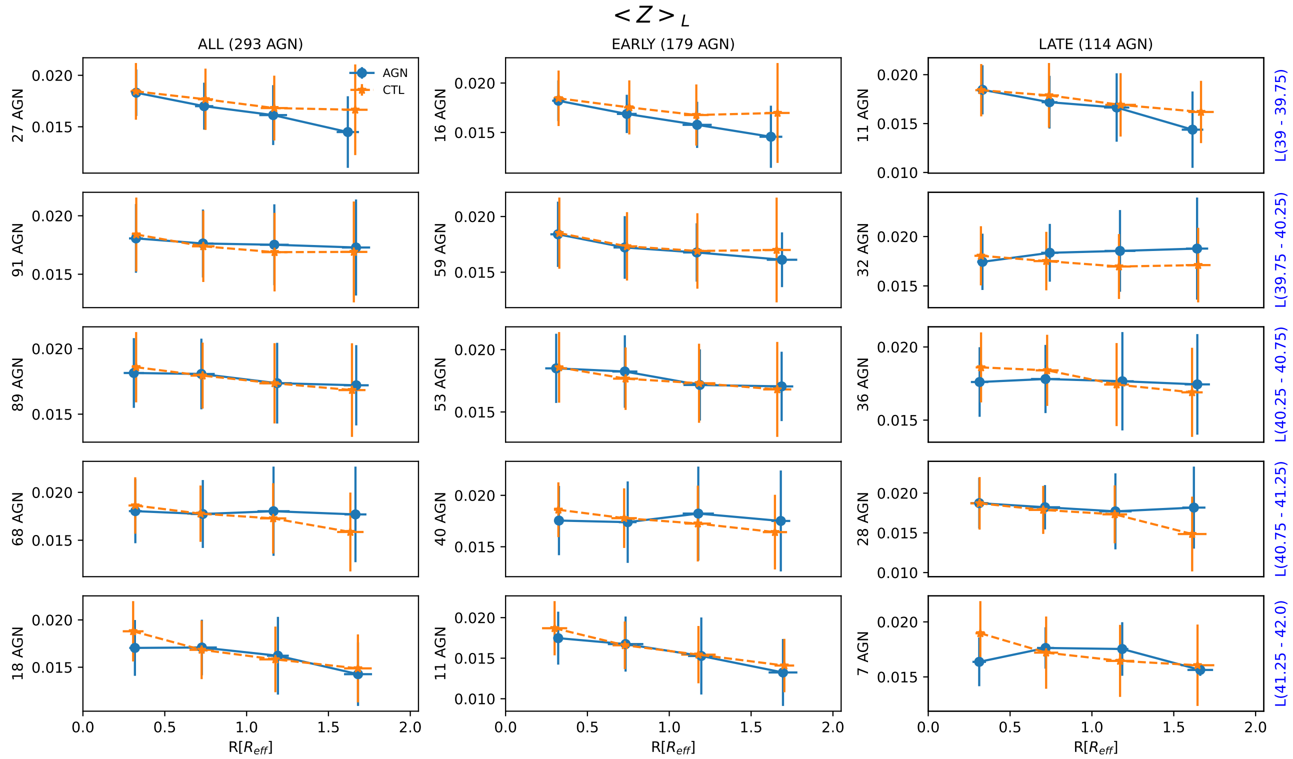

Figure 9. Light-weighted mean metallicity *versus* radius. The labels are the same as in Fig. 4.

lifetime (e.g. the mean over all the stellar generations). Nevertheless, our stellar metalicity estimates are in agreement with those obtained through the gas phase abundances.

4.3 Spatially resolved diagnostic diagrams: BPT and WHAN

It is known that AGN produces a much harder radiation field than main sequence stars. A widely used tool to identify and classify emission-line sources according to their dominant radiation field are the diagrams proposed by Baldwin et al. (1981, hereafter BPT) which are based on line ratios between high and low ionization potential species (e.g. [N II]/Hα × [O III]/Hβ). However, the BPT diagrams cannot discriminate between genuine low-ionization AGN and emission-line galaxies whose ionizing photons are produced in the atmospheres of hot low-mass evolved stars (HOLMES). To overcome this Cid Fernandes et al. (2010) have proposed a diagram that uses as a discriminator the equivalent width (EW) of the Hα emission line. They have shown that galaxies with EW(H$_\alpha$) $<$ 3Å, may not be ionized by an AGN but by the HOLMES. This diagram is known as the WHAN diagram since it involves the [N II]/Hα and EW(Hα).

In Fig. 10 and Fig. 11 we present the BPT and WHAN diagrams, respectively for AGNs and controls. These diagrams have been built with all the spaxels where the SNR in the continuum is $\geq$ 10 and the [O III]λ 5007Å emission line is detected with a minimum of 3σ confidence level, and for four different radial regions in the galaxies.

As can be seen in Fig. 10, the BPT diagrams reveal that most of the AGN emission is concentrated in the inner 0.5 R_e region of the galaxies (with Sy/LINER classification), as well as that the bulk of the emission for the control galaxies is located in the SF-dominated region. In addition, for regions outside the inner 0.5 R_e, most of the AGN hosts and control galaxies become SF-dominated and present very similar distributions. In summary, when moving radially across the galaxy (increasing R_e) what is seen is that the ionization pattern moves from the AGN-dominated region to the SF-dominated one, crossing the transition region.

On the other hand, the same behavior is not clearly seen in the WHAN diagram (Fig. 11). While the bulk of the spaxels in the inner 0.5 R_e of AGN hosts is located at consistently larger EW(Hα) values (~ 0.5 dex) than the “retired” wing of the control galaxies, spaxels in both samples also distribute along a diagonal path crossing the wAGN/sAGN regions all the way to the SF region. This extended path in the WHAN diagram corresponds to the displacement from AGN/LI(N)ER to SF-ionization in the BPT diagram across the transition region.

It is important to note that the WHAN diagram seems effective at separating the “forgotten" population of retired galaxies from true AGN-ionized ones; however, the transition region (e.g. with photons from HOLMES/SF+AGN) is not explicitly defined in this diagram. The distinction between AGN and SF objects is much more diffuse. At radial distances larger than 0.5 R_e, spaxels tend to be located in, or close to, the SF region, both for AGN hosts and control galaxies, but a significant fraction of spaxels is still located in the sAGN/wAGN region. This may be due to the fact that, as we move toward higher radii values, we observe regions where the role played by SF on the gas excitation increases, while that of the AGN decreases (Sánchez 2020), and so the EW(Hα) increases, making the locus of the region move towards the weak-AGN/SF dominated region. In the studies of Deconto-Machado et al. (2022) as in Gatto et al. (*in preparation*), on the same sample of AGN and control galaxies discussed here, we have found continuity in the kinematic properties of AGN and controls, in terms of the line widths of the [O III]λ5007Å emission lines vs. L([O III]). This can be interpreted as due to the fact that even in the regions with EW(Hα) $<$ 3 the gas may be still ionized by a mix of photons coming both from the AGN and from HOLMES. This becomes even more clear when BPT and WHAN are considered together.

In order to try to clarify the behavior described above, we have considered the BPT and WHAN together in Fig. 12: as can be seen in this figure the spaxels with larger EW(Hα) when moving to larger radii move to the SF dominated region, clearly indicating that to do a proper activity classification, besides the line ratios and EW(Hα), aperture effects also need to be considered and that the bulk of the emission outside the central region is dominated by star-forming processes (Sánchez 2020). In fact, this aperture-dependent (mis)classification has been reported by Albán & Wylezalek (2023). They found that the number of fake-AGN increases significantly for values larger than 1.0R_e and they attribute it to increased contamination from diffuse ionized gas. Sánchez (2020) shows that the ionization in the overall extension of galaxies is dominated by stellar processes (hot young stars or HOLMES), with the AGN emission being dominant in the central region of active galaxies.

5 FINAL REMARKS

We present here spaxel-by-spaxel stellar population fits for the ~10 thousand MaNGA datacubes. We provide multiple extension fits files, nominated as MEGACUBES, with maps of light- and mass-fraction contribution of each stellar population component, light-weighted and mass-weighted mean age and mean metallicity, reddening, star formation rates via stellar population (over the last 1 Myr, 5.6 Myr, 10 Myr, 14 Myr, 20 Myr, 32 Myr, 56 Myr, 100 Myr, and 200 Myr), binned population vectors in light- and mass-fraction in different age ranges (xyy≤10 Myr; 14 Myr< xyo ≤56 Myr; 100 Myr< xiy ≤500 Myr; 630 Myr < xii ≤800 Myr; 890 Myr< xio ≤2.0 Gyr; 5.0 Gyr< xo ≤13 Gyr). Parameters characterising the emission-line profiles of Hβ, [O III]$\lambda\lambda$4959,5007, He Iλ5876, [O I]λ6300, Hα [N II]$\lambda\lambda$6548,6583 and [S II]$\lambda\lambda$6716,6731, are also provided for each spaxel. All the MEGACUBES are available through a web interface (`https://manga.linea.org.br/` or `https://www.if.ufrgs.br/~riffel/software/megacubes/`), where each one of them can be inspected, downloaded, and interacted with via different plots.

We analysed the MEGACUBES for the final AGN sample (293) and control galaxies (586) in the MaNGA survey selected according to the criteria from Rembold et al. (2017), in which the control galaxies are matched to the AGN according to stellar mass, distance, inclination, and galaxy type.

We have also presented a global analysis of the stellar population of the final set of AGNs and compared them with the control galaxies sample. We found that the young and intermediate-age populations show an outwards increasing gradient for AGNs and controls, while the old component decreases outwards, indicating that the galaxies are facing a rejuvenation process. We find that the fraction of intermediate-age stellar population is higher in AGN hosts than that found in the control sample, and this difference becomes larger for higher-luminosity AGNs. This has been interpreted by us as the fact that an extra amount of gas is available in these more luminous sources and that most likely it originates from mass loss from the intermediate-age stellar population. We have also found that the mean metalicities show a similar trend for AGN hosts and control galaxies showing a decreasing gradient with increasing radius, with AGN hosts showing a slightly shallower gradient. Additionally, for regions R $<$ 0.5 R$_e$ the AGN hosts metallicity is biased towards lower values

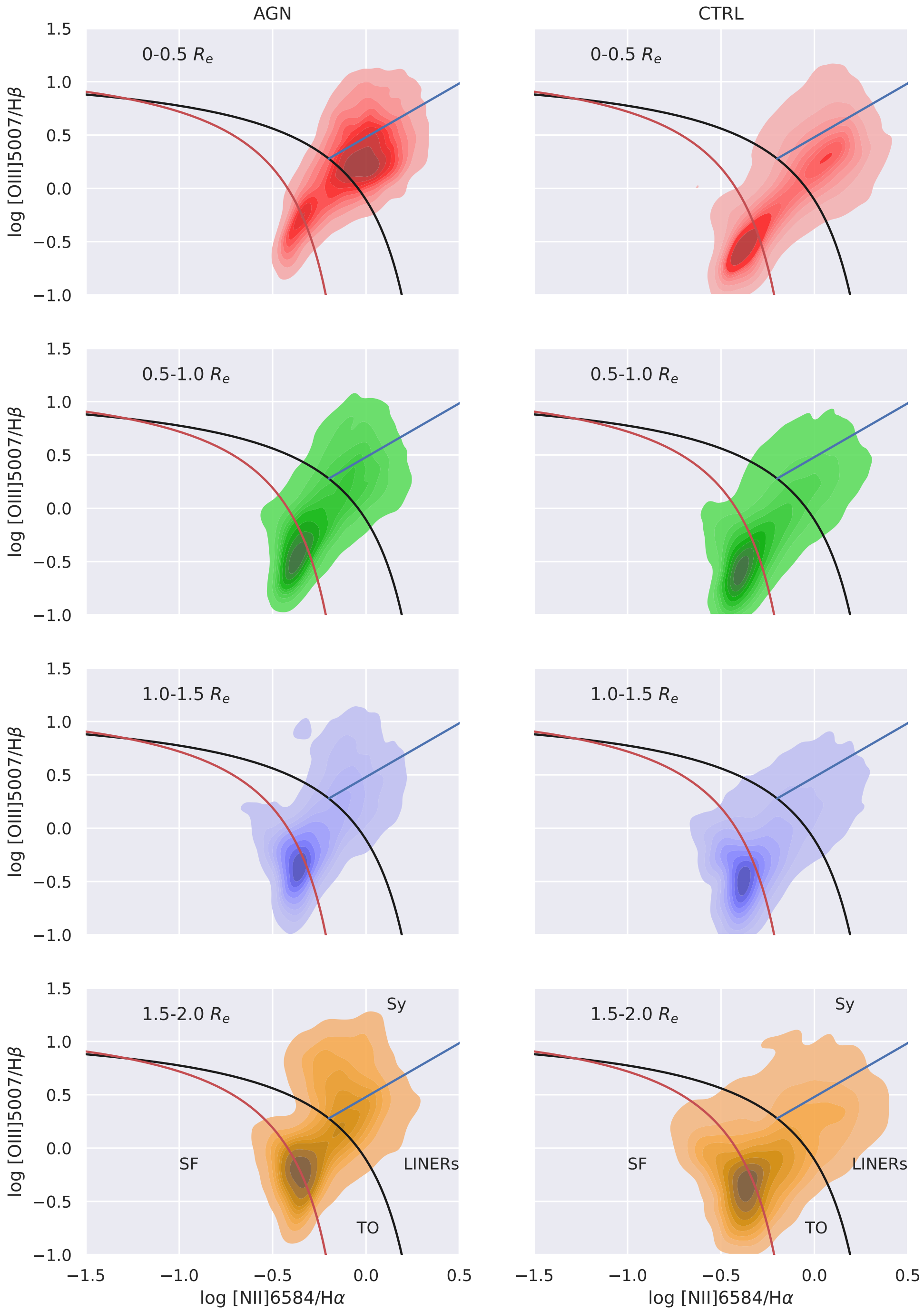

Figure 10. BPT diagnostic diagram for our AGN and control samples. In these diagrams, we show all the spaxels where SNR in the continuum is ≥ 10 and the [O III]λ 5007Å emission line is detected with a 3σ confidence level. Different radial values are shown, from top to bottom: 0 – 0.5 R_e (red), 0.5 – 1.0 R_e (green), 1.0 – 1.5 R_e (blue), and 1.5 – 2.0 R_e (yellow). Black and red lines correspond to the empirical and theoretical criteria to separate AGN-like and H ii-like objects proposed by Kewley et al. (2001) and Kauffmann et al. (2003b), respectively. The blue line represents the separation between AGN-like and LINERS-like sources proposed by Cid Fernandes et al. (2010).

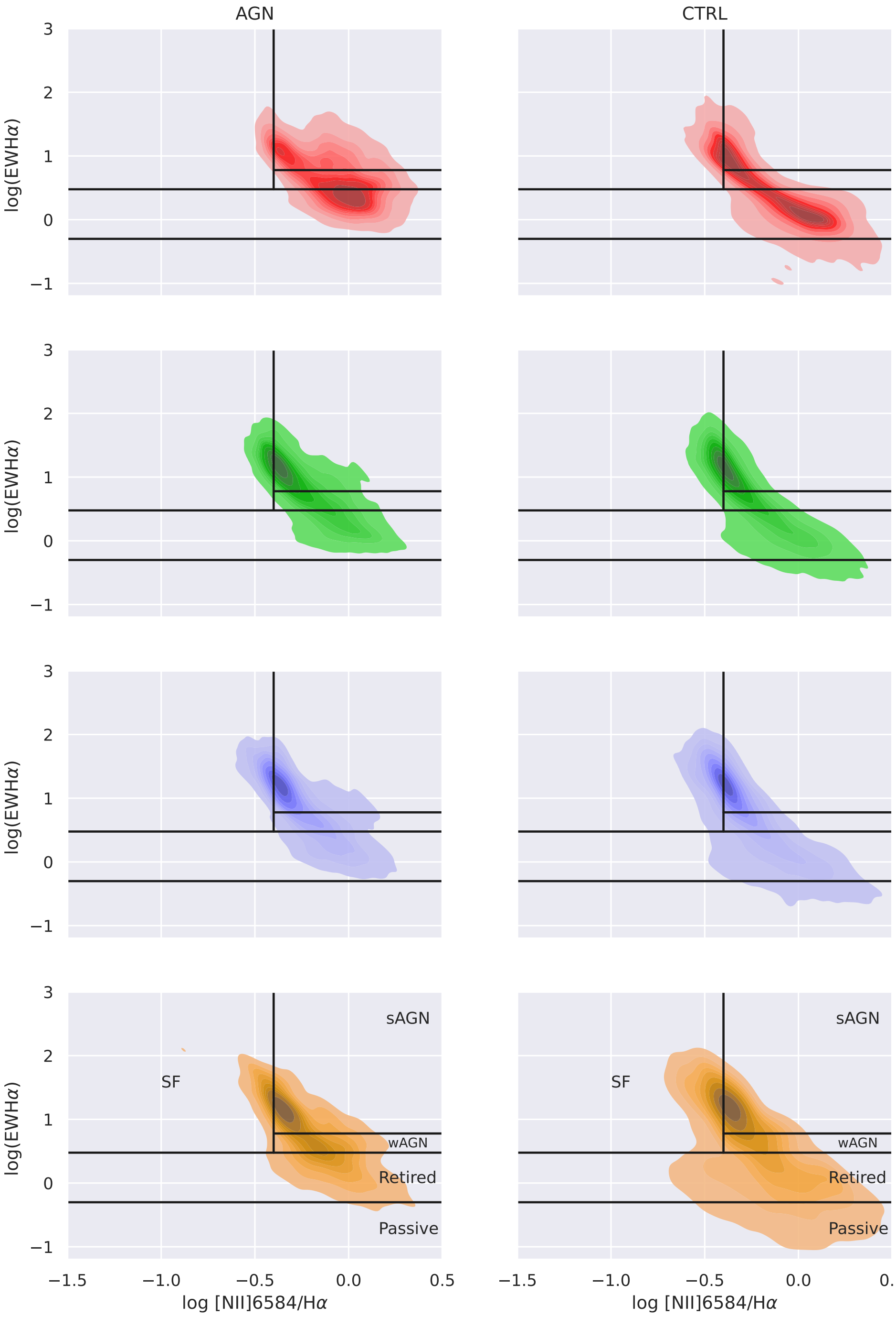

Figure 11. WHAN diagnostic diagram for our AGN and control samples for the same data-points as in Fig. 10

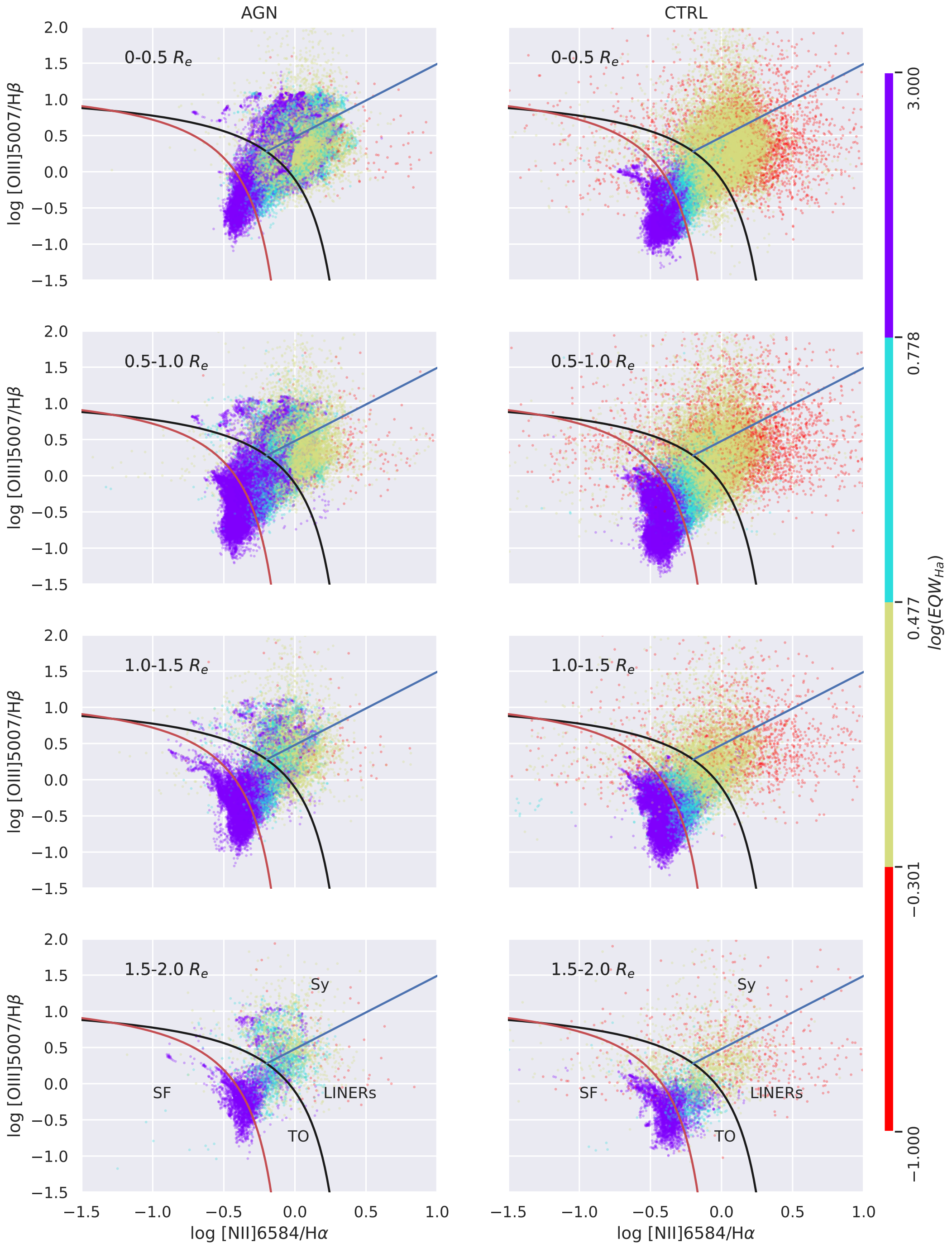

Figure 12. BPT diagnostic diagram for our AGN and control samples for distinct radial distances (from top to bottom: 0 – 0.5 R_e, 0.5 – 1.0 R_e, 1.0 – 1.5 R_e, and 1.5 – 2.0 R_e) with each spaxel colored according to the equivalent width (EW) of the Hα emission line (using the limits of the WHAN for EWHα). The lines are the same as in Fig. 10.

when compared with the control galaxies, as well as when compared with larger radii values. This is in agreement with the behavior found when studying the gas phase abundances.

Analysis of the global properties of the gas excitation via BPT and WHAN diagrams have also been presented. The spatially resolved BPT diagrams reveal that the AGN emission is concentrated in the inner 0.5 R_e region of the galaxies (with Sy/LINER classification), as well as that the bulk of the distribution for the control galaxies is located in the SF-dominated region. Additionally, besides the dependence on aperture size for proper activity type classification, we show that the BPT diagram has to be used together with the strength of the Hα equivalent width. We thus present a "composite" BPT+WHAN diagram to be used for as a more comprehensive diagnostic of the emitting gas excitation in galaxies.

ACKNOWLEDGMENTS

We thank the anonymous referee for useful suggestions which helped to improve the paper. RR acknowledges support from the Fundación Jesús Serra and the Instituto de Astrofísica de Canarias under the Visiting Researcher Programme 2023-2025 agreed between both institutions. RR, also acknowledges support from the ACIISI, Consejería de Economía, Conocimiento y Empleo del Gobierno de Canarias and the European Regional Development Fund (ERDF) under grant with reference ProID2021010079, and the support through the RAVET project by the grant PID2019-107427GB-C32 from the Spanish Ministry of Science, Innovation and Universities MCIU. This work has also been supported through the IAC project TRACES, which is partially supported through the state budget and the regional budget of the Consejería de Economía, Industria, Comercio y Conocimiento of the Canary Islands Autonomous Community. RR also thanks to Conselho Nacional de Desenvolvimento Científico e Tecnológico (CNPq, Proj. 311223/2020-6, 304927/2017-1, 400352/2016-8, and 404238/2021-1), Fundação de amparo à pesquisa do Rio Grande do Sul (FAPERGS, Proj. 16/2551-0000251-7 and 19/1750-2), Coordenação de Aperfeiçoamento de Pessoal de Nível Superior (CAPES, Proj. 0001). RAR acknowledges support from CNPq and FAPERGS. GSI acknowledges support from CNPq (142514/2018-7) and FAPESP (Fundação de Amparo à Pesquisa do Estado de São Paulo, Proj. 2022/11799-9). We are also grateful to LIneA's IT team which has supported the creation of the web portal and the INCT e-Universo. CRA acknowledges support from the projects "Feeding and feedback in active galaxies", with reference PID2019-106027GB-C42, funded by MICINN-AEI/10.13039/501100011033, and "Quantifying the impact of quasar feedback on galaxy evolution", with reference EUR2020-112266, funded by MICINN-AEI/10.13039/501100011033 and the European Union NextGenerationEU/PRTR.

SDSS is managed by the Astrophysical Research Consortium for the Participating Institutions of the SDSS Collaboration including the Brazilian Participation Group, the Carnegie Institution for Science, Carnegie Mellon University, the Chilean Participation Group, the French Participation Group, Harvard-Smithsonian Center for Astrophysics, Instituto de Astrofisica de Canarias, The Johns Hopkins University, Kavli Institute for the Physics and Mathematics of the Universe (IPMU) / University of Tokyo, the Korean Participation Group, Lawrence Berkeley National Laboratory, Leibniz Institut für Astrophysik Potsdam (AIP), Max-Planck-Institut für Astronomie (MPIA Heidelberg), Max-Planck-Institut für Astrophysik (MPA Garching), Max-Planck-Institut für Extraterrestrische Physik (MPE), National Astronomical Observatories of China, New Mexico State University, New York University, University of Notre Dame, Observatório Nacional / MCTI, The Ohio State University, Pennsylvania State University, Shanghai Astronomical Observatory, United Kingdom Participation Group, Universidad Nacional Autónoma de México, University of Arizona, University of Colorado Boulder, University of Oxford, University of Portsmouth, University of Utah, University of Virginia, University of Washington, University of Wisconsin, Vanderbilt University, and Yale University.

DATA AVAILABILITY

The data underlying this article are available under SDSS collaboration rules, and the by-products are available at: https://manga.linea.org.br/ or `https://www.if.ufrgs.br/~riffel/software/megacubes/` following the SDSS collaboration rules.

REFERENCES

Abdurro'uf et al., 2022, The Seventeenth Data Release of the Sloan Digital Sky Surveys: Complete Release of MaNGA, MaStar and APOGEE-2 Data (arxiv:2112.02026), doi:10.3847/1538-4365/ac4414

Agostino C. J., et al., 2021, The Astrophysical Journal, 922, 156

Aguado D. S., et al., 2019, The Astrophysical Journal Supplement Series, 240, 23

Alam S., et al., 2015, The Astrophysical Journal Supplement Series, 219, 12

Albán M., Wylezalek D., 2023, Classifying the Full SDSS-IV MaNGA Survey Using Optical Diagnostic Diagrams: Presentation of AGN Catalogs in Flexible Apertures, doi:10.48550/arXiv.2302.08519

Armah M., et al., 2023, Monthly Notices of the Royal Astronomical Society, 520, 1687

Baldry I. K., Glazebrook K., Brinkmann J., Ivezić Ž., Lupton R. H., Nichol R. C., Szalay A. S., 2004, The Astrophysical Journal, 600, 681

Baldwin J. A., Phillips M. M., Terlevich R., 1981, Publications of the Astronomical Society of the Pacific, 93, 5

Belfiore F., et al., 2019, The Astronomical Journal, 158, 160

Benedetti J. P. V., et al., 2023, Monthly Notices of the Royal Astronomical Society

Bessiere P. S., Ramos Almeida C., 2022, Monthly Notices of the Royal Astronomical Society, 512, L54

Bieri R., Dubois Y., Silk J., Mamon G. A., Gaibler V., 2016, Monthly Notices of the Royal Astronomical Society, 455, 4166

Blanton M. R., et al., 2017, The Astronomical Journal, 154, 28

Brammer G. B., et al., 2009, The Astrophysical Journal, 706, L173

Bundy K., et al., 2015, Astrophysical Journal, 798, 7

Cardelli J. A., Clayton G. C., Mathis J. S., 1989, The Astrophysical Journal, 345, 245

Cherinka B., et al., 2019, The Astronomical Journal, 158, 74

Cid Fernandes R., 2018, Monthly Notices of the Royal Astronomical Society, 480, 4480

Cid Fernandes R., Gu Q., Melnick J., Terlevich E., Terlevich R., Kunth D., Rodrigues Lacerda R., Joguet B., 2004, Monthly Notices of the RAS, 355, 273

Cid Fernandes R., Mateus A., Sodré L., Stasińska G., Gomes J. M., 2005, Monthly Notices of the RAS, 358, 363

Cid Fernandes R., Stasińska G., Schlickmann M. S., Mateus A., Vale Asari N., Schoenell W., Sodré L., 2010, Monthly Notices of the Royal Astronomical Society, 403, 1036

Cid Fernandes R., et al., 2013, Astronomy and Astrophysics, 557, A86

Cid Fernandes R., et al., 2014, Astronomy & Astrophysics, Volume 561, id.A130, $<$NUMPAGES$>$19$<$/NUMPAGES$>$ pp., 561, A130

Conselice C. J., 2014, Annual Review of Astronomy and Astrophysics, 52, 291

Crain R. A., et al., 2015, Monthly Notices of The Royal Astronomical Society, 450, 1937

Croton D. J., et al., 2006, Monthly Notices of The Royal Astronomical Society, 365, 11

Cuadra J., Nayakshin S., Springel V., Di Matteo T., 2006, Monthly Notices of the Royal Astronomical Society, 366, 358

Davies R. I., Sternberg A., Lehnert M. D., Tacconi-Garman L. E., 2005, The Astrophysical Journal, 633, 105

Deconto-Machado A., et al., 2022, Astronomy and Astrophysics, 659, A131

Dimauro P., et al., 2022, Monthly Notices of the Royal Astronomical Society, 513, 256

Dottori H., Díaz R. J., Carranza G., Lípari S., Santos Jr. J., 2005, The Astrophysical Journal, 628, L85

Drory N., et al., 2015, The Astronomical Journal, 149, 77

Eales S., de Vis P., Smith M. W. L., Appah K., Ciesla L., Duffield C., Schofield S., 2017, Monthly Notices of the Royal Astronomical Society, 465, 3125

El-Badry K., Wetzel A., Geha M., Hopkins P. F., Kereš D., Chan T. K., Faucher-Giguère C.-A., 2016, The Astrophysical Journal, 820, 131

Fabian A. C., 2012, Annual Review of Astronomy and Astrophysics, 50, 455

Gallagher R., Maiolino R., Belfiore F., Drory N., Riffel R., Riffel R. A., 2019, Monthly Notices of the Royal Astronomical Society, 485, 3409

Goddard D., et al., 2017, Monthly Notices of the Royal Astronomical Society, 466, 4731

González Delgado R. M., Cerviño M., Martins L. P., Leitherer C., Hauschildt P. H., 2005, Monthly Notices of the Royal Astronomical Society, 357, 945

Gunn J. E., et al., 2006, The Astronomical Journal, 131, 2332

Hopkins P. F., 2012, Monthly Notices of the RAS, 420, L8

Ibarra-Medel H. J., et al., 2016, Monthly Notices of the Royal Astronomical Society, 463, 2799

Ilha G. S., et al., 2022, Monthly Notices of the Royal Astronomical Society, 516, 1442

Ishibashi W., Fabian A. C., 2012, Monthly Notices of the Royal Astronomical Society, 427, 2998

Kauffmann G., et al., 2003a, Monthly Notices of the Royal Astronomical Society, 341, 54

Kauffmann G., et al., 2003b, Monthly Notices of the RAS, 346, 1055

Kewley L. J., Dopita M. A., Sutherland R. S., Heisler C. A., Trevena J., 2001, The Astrophysical Journal, 556, 121

King A., Pounds K., 2015, Annual Review of Astronomy and Astrophysics, 53, 115

Koski A. T., 1978, The Astrophysical Journal, 223, 56

Law D. R., et al., 2015, The Astronomical Journal, 150, 19

Law D. R., et al., 2016, The Astronomical Journal, 152, 83

Law D. R., et al., 2021, The Astronomical Journal, 161, 52

Lintott C., et al., 2011, Monthly Notices of the Royal Astronomical Society, 410, 166

Mallmann N. D., et al., 2018, Monthly Notices of the Royal Astronomical Society, 478, 5491

Martín-Navarro I., Shankar F., Mezcua M., 2022, Monthly Notices of the Royal Astronomical Society, 513, L10

Martins L. P., Rodríguez-Ardila A., Diniz S., Gruenwald R., de Souza R., 2013, Monthly Notices of the RAS, 431, 1823

Muzzin A., et al., 2013, The Astrophysical Journal, 777, 18

Nayakshin S., Zubovas K., 2012, Monthly Notices of the Royal Astronomical Society, 427, 372

Noeske K. G., et al., 2007, The Astrophysical Journal Letters, 660, L47

Paspaliaris E. D., Xilouris E. M., Nersesian A., Bianchi S., Georgantopoulos I., Masoura V. A., Magdis G. E., Plionis M., 2023, Astronomy and Astrophysics, 669, A11

Rees M. J., 1989, Monthly Notices of the Royal Astronomical Society, 239, 1P

Rembold S. B., et al., 2017, Monthly Notices of the Royal Astronomical Society, 472, 4382

Riess A. G., et al., 2022, The Astrophysical Journal, 934, L7

Riffel R., Pastoriza M. G., Rodríguez-Ardila A., Maraston C., 2007, Astrophysical Journal, Letters, 659, L103

Riffel R., Pastoriza M. G., Rodríguez-Ardila A., Bonatto C., 2009, Monthly Notices of the RAS, 400, 273

Riffel R., Ruschel-Dutra D., Pastoriza M. G., Rodríguez-Ardila A., Santos Jr. J. F. C., Bonatto C. J., Ducati J. R., 2011, Monthly Notices of the RAS, 410, 2714

Riffel R., et al., 2015, Monthly Notices of the RAS, 450, 3069

Riffel R. A., et al., 2016, Monthly Notices of the Royal Astronomical Society, 461, 4192

Riffel R. A., Storchi-Bergmann T., Riffel R., Dahmer-Hahn L. G., Diniz M. R., Schönell A. J., Dametto N. Z., 2017, Monthly Notices of the Royal Astronomical Society, 470, 992

Riffel R. A., et al., 2018, Monthly Notices of the Royal Astronomical Society, 474, 1373

Riffel R., et al., 2021a, Monthly Notices of the Royal Astronomical Society, 501, 4064

Riffel R. A., Bianchin M., Riffel R., Storchi-Bergmann T., Schönell A. J., Dahmer-Hahn L. G., Dametto N. Z., Diniz M. R., 2021b, Monthly Notices of the Royal Astronomical Society, 503, 5161

Riffel R. A., et al., 2021c, Monthly Notices of the Royal Astronomical Society, 504, 3265

Riffel R., et al., 2022, Monthly Notices of the Royal Astronomical Society, 512, 3906

Ruschel-Dutra 2020, Danielrd6/Ifscube v1.0, Zenodo, doi:10.5281/zenodo.3945237

Ruschel-Dutra D., et al., 2021, Monthly Notices of the Royal Astronomical Society, 507, 74

Salvador-Rusiñol N., Vazdekis A., La Barbera F., Beasley M. A., Ferreras I., Negri A., Dalla Vecchia C., 2020, Nature Astronomy, 4, 252

Salvador-Rusiñol N., Beasley M. A., Vazdekis A., Barbera F. L., 2021, Monthly Notices of the Royal Astronomical Society, 500, 3368

Sánchez S. F., 2020, Annual Review of Astronomy and Astrophysics, vol. 58, p.99-155, 58, 99

Sánchez S. F., et al., 2013, Astronomy and Astrophysics, 554, A58

Sánchez S. F., Walcher C. J., Lopez-Cobá C., Barrera-Ballesteros J. K., Mejía-Narváez A., Espinosa-Ponce C., Camps-Fariña A., 2021, Revista Mexicana de Astronomia y Astrofisica, 57, 3

Schaye J., et al., 2015, Monthly Notices of the Royal Astronomical Society, 446, 521

Schlegel D. J., Finkbeiner D. P., Davis M., 1998, The Astrophysical Journal, 500, 525

Schnorr-Müller A., et al., 2021, Monthly Notices of the Royal Astronomical Society, 507, 300

Smee S. A., et al., 2013, The Astronomical Journal, 146, 32

Springel V., et al., 2005, Nature, 435, 629

Steiner J. E., Menezes R. B., Ricci T. V., Oliveira A. S., 2009, Monthly Notices of the Royal Astronomical Society, 395, 64

Storchi-Bergmann T., Schnorr-Müller A., 2019, Nature Astronomy, 3, 48

Storchi-Bergmann T., McGregor P. J., Riffel R. A., Simões Lopes R., Beck T., Dopita M., 2009, Monthly Notices of the RAS, 394, 1148

Storchi-Bergmann T., Riffel R. A., Riffel R., Diniz M. R., Borges Vale T., McGregor P. J., 2012, Astrophysical Journal, 755, 87

Tacconi L. J., Genzel R., Sternberg A., 2020, Annual Review of Astronomy and Astrophysics, vol. 58, p.157-203, 58, 157

Thomas D., et al., 2013, Monthly Notices of the Royal Astronomical Society, 431, 1383

Trussler J., Maiolino R., Maraston C., Peng Y., Thomas D., Goddard D., Lian J., 2020, Monthly Notices of the Royal Astronomical Society, 491, 5406

Vazdekis A., Sánchez-Blázquez P., Falcón-Barroso J., Cenarro A. J., Beasley M. A., Cardiel N., Gorgas J., Peletier R. F., 2010, Monthly Notices of the Royal Astronomical Society, 404, 1639

Vazdekis A., Koleva M., Ricciardelli E., Röck B., Falcón-Barroso J., 2016, Monthly Notices of the RAS, 463, 3409

Vázquez-Mata J. A., et al., 2022, Monthly Notices of the Royal Astronomical Society, 512, 2222

Vogelsberger M., et al., 2014, Nature, 509, 177

Wake D. A., et al., 2017, The Astronomical Journal, 154, 86

Wang X., Loeb A., 2018, New Astronomy, 61, 95

Westfall K. B., et al., 2019, The Astronomical Journal, 158, 231

Wetzel A. R., Tinker J. L., Conroy C., 2012, Monthly Notices of the Royal Astronomical Society, 424, 232

Yan R., et al., 2016a, The Astronomical Journal, 151, 8

Capítulo 8

Considerações Finais

Como produto desse trabalho, processamos cerca de 10000 cubos de dados do *survey* MaNGA com o nosso software URUTAU e os códigos IFSCUBE e STARLIGHT. Cada cubo de dados contém uma série de propriedades derivadas da síntese de população estelar e podem ser acessados pelo portal do LINeA (`https://manga.linea.org.br/`) que foi desenvolvido para acessar, interagir e baixar os cubos de dados processados. Entre outras aspectos (veja Apendice 8.1), utilizamos o produto desse processamento para analisar a fonte primária de ionização do gás e as populações estelares de AGNs observadas pelo MaNGA, resultados estes descritos nos dois capítulos anteriores.

Primeiramente apresentamos uma análise comparando as taxas de formação estelar nos spaxels classificados via BPT e WHAN como dominados por formação estelar derivadas via linhas de recombinação do hidrogênio e via ajuste da população estelar para uma sub-amostra dos objetos (à época pouco mais de 5 mil objetos haviam sido observados pelo survey).

O $\Sigma\mathrm{SFR}_\star$ nos últimos 20 Myrs e $\Sigma\mathrm{SFR}_{\mathrm{Gas}}$ mostram a melhor correlação entre todos os intervalos de idade testados, incluindo ou não na análise os spaxels de SF de galáxias hospedeiras de AGN. A equação de transformação é $\log(\Sigma\mathrm{SFR}_\star) = (0.872 \pm 0.004)\log(\Sigma\mathrm{SFR}_{\mathrm{Gas}}) - (0.075 \pm 0.006)$ ou $\log(\Sigma\mathrm{SFR}_{\mathrm{Gas}}) = (1.147 \pm 0.005)\log(\Sigma\mathrm{SFR}_\star) + (0.086 \pm 0.080)$. Este resultado abre um novo caminho para obter as taxas de formação estelar (SFRs) em galáxias hospedeiras de AGN, mesmo na NLR e ENLR, onde o AGN domina a excitação das linhas de emissão e a SFR não pode ser obtida diretamente a partir dos fluxos da linha de hidrogênio.

Algumas AGN mostram um excesso de $\Sigma\mathrm{SFR}$ em relação ao restante da amostra, que atribuímos tentativamente a um reservatório de gás maior e maior eficiência de formação estelar. Coincidentemente, esses AGNs parecem ter vizinhos próximos, o que poderia ter impulsionado a formação estelar.

Descobrimos que a extinção visual $A_{V,g}$ derivada do decremento de Balmer é de 2,63 a 2,86 vezes maior do que a extinção derivada via síntese da população estelar, $A_{V,\star}$. Esse resultado está em acordo com resultados anteriores da literatura baseados em amostras muito menores. Interpretamos a diferença como sendo devido ao fato de que STARLIGHT trabalha com um avermelhamento único para todas as populações, e o avermelhamento do conteúdo estelar é dominado pela população mais velha, que é menos extinta do que a população estelar jovem que teria extinção similar à do gás em regiões de formação de estrelas.

No capítulo 7, apresentamos ajustes da população estelar spaxel a spaxel para cerca de 10 mil cubos de dados do MaNGA. Fornecemos vários arquivos FITS com diferentes extensões, denominados MEGACUBES, com mapas de contribuição de fração de luz e massa de cada componente da população estelar, idade e metalicidade médias ponderadas por luz e massa, avermelhamento, taxas de formação estelar (nos últimos 1 Myr, 5.6 Myr, 10 Myr, 14 Myr, 20 Myr, 32 Myr, 56 Myr, 100 Myr e 200 Myr), vetores de população em diferentes intervalos de idade binadas por fração de luz e massa (xyy$\leq$10 Myr; 14 Myr$<$ xyo $\leq$56 Myr; 100 Myr$<$ xiy $\leq$500 Myr; 630 Myr $<$ xii $\leq$800 Myr; 890 Myr$<$ xio $\leq$2.0 Gyr; 5.0 Gyr$<$ xo $\leq$13 Gyr). Parâmetros que caracterizam os perfis de linha de emissão de Hβ, [O III]$\lambda\lambda$4959,5007, He Iλ5876, [O I]λ6300, Hα [N II]$\lambda\lambda$6548,6583 e [S II]$\lambda\lambda$6716,6731 também são fornecidos para cada spaxel. Todos os MEGACUBES estão disponíveis por meio de uma interface web (`https://manga.linea.org.br/`), onde cada um deles pode ser visualizado, inspecionado por meio de diferentes gráficos e baixado.

Analisamos os MEGACUBES para a amostra final de AGNs (293) e galáxias de controle (586) survey MaNGA, selecionados de acordo com os critérios de Rembold et al. (2017), nos quais as galáxias de controle são pareadas com os AGNs de acordo com massa estelar, distância, inclinação e tipo de morfológico.

Também apresentamos uma análise global da população estelar do conjunto final de AGNs e os comparamos com a amostra de galáxias de controle. Descobrimos que as populações estelares jovens e de idade intermediária mostram um gradiente crescente para fora tanto para os AGNs quanto para os controles, enquanto o componente velho diminui para fora, indicando que as galáxias estão passando por um processo de rejuvenescimento. Verificamos que a fração de população estelar de idade intermediária é maior nos hospedeiros de AGNs do que na amostra de controle, e essa diferença se torna maior para AGNs de maior luminosidade. Isso foi interpretado por nós como o fato de que uma quantidade extra de gás está disponível nessas fontes mais luminosas e que provavelmente se origina da perda de massa da população estelar de idade intermediária. Também descobrimos que as metalicidades médias mostram uma tendência semelhante para hospedeiras de AGN e galáxias de controle, mostrando um gradiente decrescente com o aumento do raio, com as hospedeiras de AGN apresentando um gradiente ligeiramente mais suave. Além disso, para regiões R < 0.5,R$_e$, a metalicidade dos AGN está enviesada para valores mais baixos quando comparada com as galáxias de controle, assim como quando comparada com valores de raios maiores. Isso está de acordo com o comportamento encontrado ao estudar as abundâncias do gás.

Também foram apresentadas análises das propriedades globais da excitação do gás por meio de diagramas BPT e WHAN. Os diagramas BPT espacialmente resolvidos revelam que a emissão do AGN está concentrada na região interna de $0.5,R_e$ das galáxias (com classificação Sy/LINER), assim como a maior parte da distribuição para as galáxias de controle está localizada na região dominada por formação estelar. Além disso, além da dependência do tamanho da abertura para classificação adequada do tipo de atividade, verificamos que o diagrama BPT deve ser usado em conjunto com a largura equivalente de . Apresentamos assim um diagrama "composto" BPT+WHAN a ser usado como um diagnóstico mais acurado na classificação do mecanismo dominante na excitação do gás emissor em galáxias. A titulo de ilustração aqui comparamos também estes diagramas de diagnostico (composto) em escalas físicas, de kpc, conforme pode ser visto na figura XXX...

8.1 Perspectivas

Os resultados apresentados aqui demonstram claramente os potenciais do software modular URUTAU. Um dos grandes legados do presente trabalho é o próprio software URUTAU e seus produtos MEGACUBES. A fim de ilustrar a sua versatilidade apresentamos abaixo uma aplicação do mesmo a um cubo do instrumento MUSE anexado ao Very Large Telescope e um exemplo de aplicação à um cubo do instrumento SIFS anexado ao telescópio SOAR. Os dados do SIFS foram obtidos com o projeto *AGN Before and After: Towards a balanced view of the connection between large-scale and circum-nuclear gas phases.* (projeto: SO2021B-102, P.I. Rogério Riffel).

As figuras 8.1-8.5, mostramos alguns resultados obtidos para a galáxia NGC2992 usando os cubos de dados do MUSE e SIFS, mostrando que o URUTAU é flexível e pode ser aplicado em qualquer cubo de dados.

Além de aumentar a funcionalidade do URUTAU através de novos módulos, o

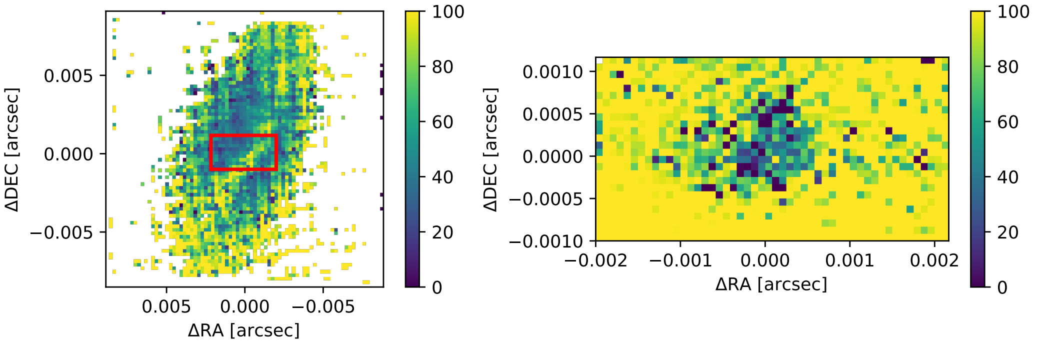

(a)

Figura 8.1: Comparação dos mapas de contribuição de luz das populações jovens (Xy $\leq$ 56 Myr) para a galáxia NGC2992 extraídos dos cubos do MUSE (esquerda) e SIFS (direita). O retângulo vermelho representa a área observada pelo SIFS.

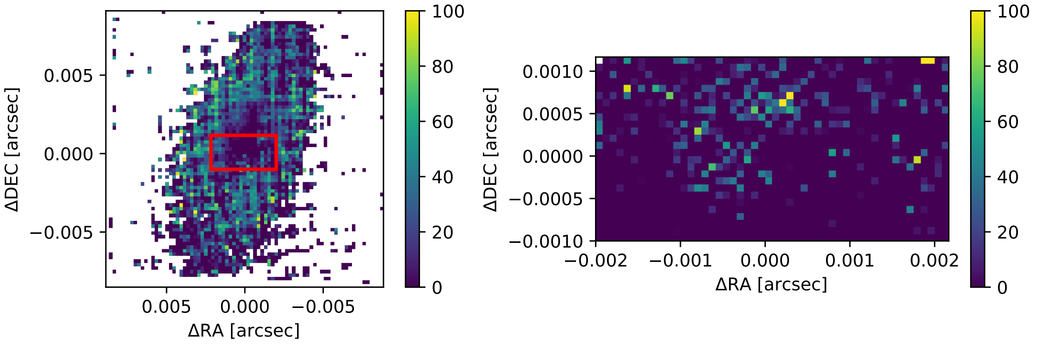

(a)

Figura 8.2: Comparação dos mapas de contribuição de luz das populações de idades intermediárias (100 Myr $<$ Xi $\leq$ 2.0 Gyr) .

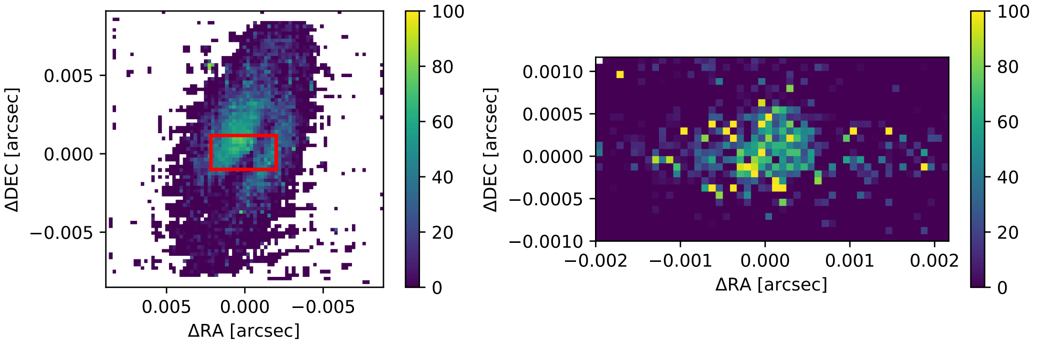

(a)

Figura 8.3: Comparação dos mapas de contribuição de luz das populações velhas (5.0 Gyr $<$ Xo $\leq$ 13 Gyr) .

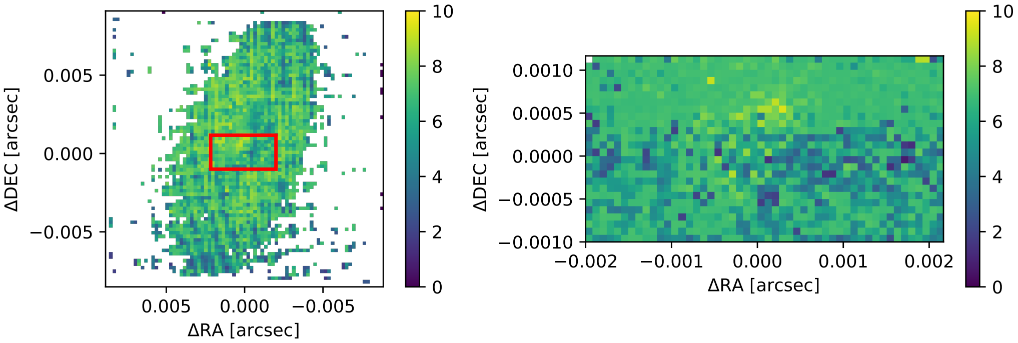

(a)

Figura 8.4: Comparação dos mapas de idades (em log) médias pesadas em luz.

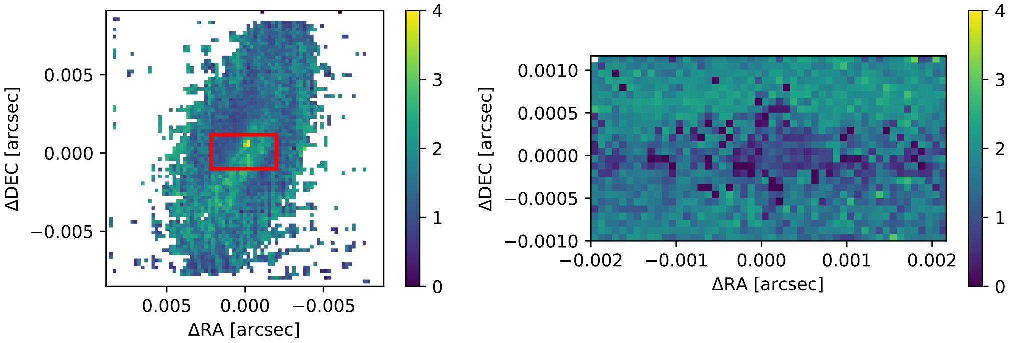

(a)

Figura 8.5: Comparação dos mapas de extinção por poeira (Av).

urutau será submetido para publicação através de um artigo dedicado em revista (Mallmann & Riffel, 2023).

Apêndice A: Outros resultados científicos que foram gerados pelo URUTAU/MEGACUBE

Abaixo listamos outros resultados que foram gerados graças ao desenvolvimento do URUTAU e, em especial, sua versão posterior MEGACUBE.

- do Nascimento J. C., Dors O. L., Storchi-Bergmann T., Mallmann N. D., Riffel R., Ilha G. S., Riffel R. A., et al., 2022, MNRAS, 513, 807.
- Kakkad D., Sani E., Rojas A. F., Mallmann N. D., Veilleux S., Bauer F. E., Ricci F., et al., 2022, MNRAS, 511, 2105.
- Schnorr-Müller A., Trevisan M., Riffel R., Chies-Santos A. L., Furlanetto C., Ricci T. V., Lohmann F. S., et al., 2021, MNRAS, 507, 300.
- do Nascimento J. C., Storchi-Bergmann T., Mallmann N. D., Riffel R., Ilha G. S., Riffel R. A., Rembold S. B., et al., 2019, MNRAS, 486, 5075.
- Ilha G. S., Riffel R. A., Schimoia J. S., Storchi-Bergmann T., Rembold S. B., Riffel R., Wylezalek D., et al., 2019, MNRAS, 484, 252.
- Mallmann N. D., Riffel R., Storchi-Bergmann T., Rembold S. B., Riffel R. A., Schimoia J., da Costa L. N., et al., 2018, MNRAS, 478, 5491.
- Goddard D., Thomas D., Maraston C., Westfall K., Etherington J., Riffel R., Mallmann N. D., et al., 2017, MNRAS, 466, 4731.
- Goddard D., Thomas D., Maraston C., Westfall K., Etherington J., Riffel R., Mallmann N. D., et al., 2017, MNRAS, 465, 688.

Referências Bibliográficas

[1] ABDURRO'UF, , ACCETTA, KATHERINE, AERTS, CONNY, SILVA AGUIRRE, VíCTOR, AHUMADA, ROMINA, AJGAONKAR, NIKHIL, FILIZ AK, N., ALAM, SHADAB, ALLENDE PRIETO, CARLOS, ALMEIDA, ANDRÉS, ANDERS, FRIEDRICH, ANDERSON, SCOTT F., ANDREWS, BRETT H., ANGUIANO, BORJA, AQUINO-ORTíZ, ERIK, ARAGÓN-SALAMANCA, ALFONSO, ARGUDO-FERNÁNDEZ, MARIA, ATA, METIN, AUBERT, MARIE, AVILA-REESE, VLADIMIR, BADENES, CARLES, BARBÁ, RODOLFO H., BARGER, KAT, BARRERA-BALLESTEROS, JORGE K., BEATON, RACHAEL L., BEERS, TIMOTHY C., BELFIORE, FRANCESCO, BENDER, CHAD F., BERNARDI, MARIANGELA, BERSHADY, MATTHEW A., BEUTLER, FLORIAN, BIDIN, CHRISTIAN MONI, BIRD, JONATHAN C., BIZYAEV, DMITRY, BLANC, GUILLERMO A., BLANTON, MICHAEL R., BOARDMAN, NICHOLAS FRASER, BOLTON, ADAM S., BOQUIEN, MÉDÉRIC, BORISSOVA, JURA, BOVY, JO, BRANDT, W. N., BROWN, JORDAN, BROWNSTEIN, JOEL R., BRUSA, MARCELLA, BUCHNER, JOHANNES, BUNDY, KEVIN, BURCHETT, JOSEPH N., BUREAU, MARTIN, BURGASSER, ADAM, CABANG, TUESDAY K., CAMPBELL, STEPHANIE, CAPPELLARI, MICHELE, CARLBERG, JOLEEN K., WANDERLEY, FÁBIO CARNEIRO, CARRERA, RICARDO, CASH, JENNIFER, CHEN, YAN-PING, CHEN, WEI-HUAI, CHERINKA, BRIAN, CHIAPPINI, CRISTINA, CHOI, PETER DOOHYUN, CHOJNOWSKI, S. DREW, CHUNG, HAEUN, CLERC, NICOLAS, COHEN, ROGER E., COMERFORD, JULIA M., COMPARAT, JOHAN, DA COSTA, LUIZ, COVEY, KEVIN, CRANE, JEFFREY D., CRUZ-GONZALEZ, IRENE, CULHANE, CONNOR, CUNHA, KATIA, DAI, Y. SOPHIA, DAMKE, GUILLERMO, DARLING, JEREMY, DAVIDSON, JR., JAMES W., DAVIES, ROGER, DAWSON, KYLE, DE LEE, NATHAN, DIAMOND-STANIC, ALEKSAN-

DAR M., CANO-DíAZ, MARIANA, SÁNCHEZ, HELENA DOMíNGUEZ, DONOR, JOHN, DUCKWORTH, CHRIS, DWELLY, TOM, EISENSTEIN, DANIEL J., ELSWORTH, YVONNE P., EMSELLEM, ERIC, ERACLEOUS, MIKE, ESCOFFIER, STEPHANIE, FAN, XIAOHUI, FARR, EMILY, FENG, SHUAI, FERNÁNDEZ-TRINCADO, JOSÉ G., FEUILLET, DIANE, FILIPP, ANDREAS, FILLINGHAM, SEAN P., FRINCHABOY, PETER M., FROMENTEAU, SEBASTIEN, GALBANY, LLUíS, GARCíA, RAFAEL A., GARCíA-HERNÁNDEZ, D. A., GE, JUNQIANG, GEISLER, DOUG, GELFAND, JOSEPH, GÉRON, TOBIAS, GIBSON, BENJAMIN J., GODDY, JULIAN, GODOY-RIVERA, DIEGO, GRABOWSKI, KATHLEEN, GREEN, PAUL J., GREENER, MICHAEL, GRIER, CATHERINE J., GRIFFITH, EMILY, GUO, HONG, GUY, JULIEN, HADJARA, MASSINISSA, HARDING, PAUL, HASSELQUIST, STEN, HAYES, CHRISTIAN R., HEARTY, FRED, HERNÁNDEZ, JESÚS, HILL, LEWIS, HOGG, DAVID W., HOLTZMAN, JON A., HORTA, DANNY, HSIEH, BAU-CHING, HSU, CHIN-HAO, HSU, YUN-HSIN, HUBER, DANIEL, HUERTAS-COMPANY, MARC, HUTCHINSON, BRIAN, HWANG, HO SEONG, IBARRA-MEDEL, HÉCTOR J., CHITHAM, JACOB IDER, ILHA, GABRIELE S., IMIG, JULIE, JAEKLE, WILL, JAYASINGHE, THARINDU, JI, XIHAN, JOHNSON, JENNIFER A., JONES, AMY, JÖNSSON, HENRIK, KATKOV, IVAN, KHALATYAN, DR., ARMAN, KINEMUCHI, KAREN, KISKU, SHOBHIT, KNAPEN, JOHAN H., KNEIB, JEAN-PAUL, KOLLMEIER, JUNA A., KONG, MIRANDA, KOUNKEL, MARINA, KRECKEL, KATHRYN, KRISHNARAO, DHANESH, LACERNA, IVAN, LANE, RICHARD R., LANGGIN, RACHEL, LAVENDER, RAMON, LAW, DAVID R., LAZARZ, DANIEL, LEUNG, HENRY W., LEUNG, HO-HIN, LEWIS, HANNAH M., LI, CHENG, LI, RAN, LIAN, JIANHUI, LIANG, FU-HENG, LIN, LIHWAI, LIN, YEN-TING, LIN, SICHENG, LINTOTT, CHRIS, LONG, DAN, LONGAPEÑA, PENÉLOPE, LÓPEZ-COBÁ, CARLOS, LU, SHENGDONG, LUNDGREN, BRITT F., LUO, YUANZE, MACKERETH, J. TED, DE LA MACORRA, AXEL, MAHADEVAN, SUVRATH, MAJEWSKI, STEVEN R., MANCHADO, ARTURO, MANDEVILLE, TRAVIS, MARASTON, CLAUDIA, MARGALEF-BENTABOL, BERTA, MASSERON, THOMAS, MASTERS, KAREN L., MATHUR, SAVITA, MCDERMID, RICHARD M., MCKAY, MYLES, MERLONI, ANDREA, MERRIFIELD, MICHAEL, MESZAROS, SZABOLCS, MIGLIO, ANDREA, DI MILLE, FRANCESCO, MIN-

NITI, DANTE, MINSLEY, REBECCA, MONACHESI, ANTONELA, MOON, JEONGIN, MOSSER, BENOIT, MULCHAEY, JOHN, MUNA, DEMITRI, MUÑOZ, RICARDO R., MYERS, ADAM D., MYERS, NATALIE, NADATHUR, SESHADRI, NAIR, PREETHI, NANDRA, KIRPAL, NEUMANN, JUSTUS, NEWMAN, JEFFREY A., NIDEVER, DAVID L., NIKAKHTAR, FARNIK, NITSCHELM, CHRISTIAN, O'CONNELL, JULIA E., GARMA-OEHMICHEN, LUIS, LUAN SOUZA DE OLIVEIRA, GABRIEL, OLNEY, RICHARD, ORAVETZ, DANIEL, ORTIGOZA-URDANETA, MARIO, OSORIO, YEISSON, OTTER, JUSTIN, PACE, ZACHARY J., PADILLA, NELSON, PAN, KAIKE, PAN, HSI-AN, PARIKH, TANIYA, PARKER, JAMES, PEIRANI, SEBASTIEN, PEÑA RAMíREZ, KARLA, PENNY, SAMANTHA, PERCIVAL, WILL J., PEREZ-FOURNON, ISMAEL, PINSONNEAULT, MARC, POIDEVIN, FRÉDÉRICK, POOVELIL, VIJITH JACOB, PRICE-WHELAN, ADRIAN M., BÁRBARA DE ANDRADE QUEIROZ, ANNA, RADDICK, M. JORDAN, RAY, AMY, REMBOLD, SANDRO BARBOZA, RIDDLE, NICOLE, RIFFEL, ROGEMAR A., RIFFEL, ROGÉRIO, RIX, HANS-WALTER, ROBIN, ANNIE C., RODRíGUEZ-PUEBLA, ALDO, ROMAN-LOPES, ALEXANDRE, ROMÁN-ZÚÑIGA, CARLOS, ROSE, BENJAMIN, ROSS, ASHLEY J., ROSSI, GRAZIANO, RUBIN, KATE H. R., SALVATO, MARA, SÁNCHEZ, SEBÁSTIAN F., SÁNCHEZ-GALLEGO, JOSÉ R., SANDERSON, ROBYN, SANTANA ROJAS, FELIPE ANTONIO, SARCENO, EDGAR, SARMIENTO, REGINA, SAYRES, CONOR, SAZONOVA, ELIZAVETA, SCHAEFER, ADAM L., SCHIAVON, RICARDO, SCHLEGEL, DAVID J., SCHNEIDER, DONALD P., SCHULTHEIS, MATHIAS, SCHWOPE, AXEL, SERENELLI, ALDO, SERNA, JAVIER, SHAO, ZHENGYI, SHAPIRO, GRIFFIN, SHARMA, ANUBHAV, SHEN, YUE, SHETRONE, MATTHEW, SHU, YIPING, SIMON, JOSHUA D., SKRUTSKIE, M. F., SMETHURST, REBECCA, SMITH, VERNE, SOBECK, JENNIFER, SPOO, TAYLOR, SPRAGUE, DANI, STARK, DAVID V., STASSUN, KEIVAN G., STEINMETZ, MATTHIAS, STELLO, DENNIS, STONE-MARTINEZ, ALEXANDER, STORCHI-BERGMANN, THAISA, STRINGFELLOW, GUY S., STUTZ, AMELIA, SU, YUNG-CHAU, TAGHIZADEH-POPP, MANUCHEHR, TALBOT, MICHAEL S., TAYAR, JAMIE, TELLES, EDUARDO, TESKE, JOHANNA, THAKAR, ANI, THEISSEN, CHRISTOPHER, TKACHENKO, ANDREW, THOMAS, DANIEL, TOJEIRO, RITA, HERNANDEZ TOLEDO, HECTOR, TROUP, NICHO-

LAS W., TRUMP, JONATHAN R., TRUSSLER, JAMES, TURNER, JACQUELINE, TUTTLE, SARAH, UNDA-SANZANA, EDUARDO, VÁZQUEZ-MATA, JOSÉ ANTONIO, VALENTINI, MARICA, VALENZUELA, OCTAVIO, VARGAS-GONZÁLEZ, JAIME, VARGAS-MAGAÑA, MARIANA, ALFARO, PABLO VERA, VILLANOVA, SANDRO, VINCENZO, FIORENZO, WAKE, DAVID, WARFIELD, JACK T., WASHINGTON, JESSICA DIANE, WEAVER, BENJAMIN ALAN, WEIJMANS, ANNE-MARIE, WEINBERG, DAVID H., WEISS, ACHIM, WESTFALL, KYLE B., WILD, VIVIENNE, WILDE, MATTHEW C., WILSON, JOHN C., WILSON, ROBERT F., WILSON, MIKAYLA, WOLF, JULIEN, WOOD-VASEY, W. M., YAN, RENBIN, ZAMORA, OLGA, ZASOWSKI, GAIL, ZHANG, KAI, ZHAO, CHENG, ZHENG, ZHENG, ZHENG, ZHENG, ZHU, KAI. The Seventeenth Data Release of the Sloan Digital Sky Surveys: Complete Release of MaNGA, MaStar, and APOGEE-2 Data. **ApJS**, v. 259, n. 2, p. 35, April 2022.

[2] AHUMADA, ANDREA V., VEGA-NEME, LUIS R., CLARIÁ, JUAN J., MINNITI, JAVIER H. Spectroscopic Fundamental Parameters of 16 Young Large Magellanic Cloud Star Clusters. **PASP**, v. 131, n. 996, p. 024101, Feb 2019.

[3] BALDWIN, J. A., PHILLIPS, M. M., TERLEVICH, R. Classification parameters for the emission-line spectra of extragalactic objects. **PASP**, v. 93, p. 5–19, February 1981.

[4] BECKMANN, VOLKER, SHRADER, CHRIS R. **Active Galactic Nuclei**: 2012.

[5] BUNDY, K., BERSHADY, M. A., LAW, D. R., YAN, R., DRORY, N., MACDONALD, N., WAKE, D. A., CHERINKA, B., SÁNCHEZ-GALLEGO, J. R., WEIJMANS, A.-M., THOMAS, D., TREMONTI, C., MASTERS, K., COCCATO, L., DIAMOND-STANIC, A. M., ARAGÓN-SALAMANCA, A., AVILA-REESE, V., BADENES, C., FALCÓN-BARROSO, J., BELFIORE, F., BIZYAEV, D., BLANC, G. A., BLAND-HAWTHORN, J., BLANTON, M. R., BROWNSTEIN, J. R., BYLER, N., CAPPELLARI, M., CONROY, C., DUTTON, A. A., EMSELLEM, E., ETHERINGTON, J., FRINCHABOY, P. M., FU, H., GUNN, J. E., HARDING, P., JOHNSTON, E. J., KAUFFMANN, G., KINEMUCHI, K., KLAENE, M. A., KNAPEN, J. H., LEAUTHAUD, A., LI, C., LIN, L., MAIOLINO, R., MALANUSHENKO, V., MALANUSHENKO, E., MAO, S., MARASTON, C., MCDERMID, R. M., MERRIFIELD, M. R., NICHOL, R. C., ORAVETZ, D., PAN, K., PAREJKO, J. K., SANCHEZ, S. F.,

SCHLEGEL, D., SIMMONS, A., STEELE, O., STEINMETZ, M., THANJAVUR, K., THOMPSON, B. A., TINKER, J. L., VAN DEN BOSCH, R. C. E., WESTFALL, K. B., WILKINSON, D., WRIGHT, S., XIAO, T., ZHANG, K. Overview of the SDSS-IV MaNGA Survey: Mapping nearby Galaxies at Apache Point Observatory. **ApJ**, v. 798, p. 7, January 2015.

[6] BURTSCHER, L., DAVIES, R. I., SHIMIZU, T. T., RIFFEL, R., ROSARIO, D. J., HICKS, E. K. S., LIN, M. Y., RIFFEL, R. A., SCHARTMANN, M., SCHNORR-MÜLLER, A., STORCHI-BERGMANN, T., ORBAN DE XIVRY, G., VEILLEUX, S. LLAMA: Stellar populations in the nuclei of ultra-hard X-ray-selected AGN and matched inactive galaxies. **A&A**, v. 654, p. A132, October 2021.

[7] CARDELLI, J. A., CLAYTON, G. C., MATHIS, J. S. The relationship between infrared, optical, and ultraviolet extinction. **ApJ**, v. 345, p. 245–256, October 1989a.

[8] CARDELLI, JASON A., CLAYTON, GEOFFREY C., MATHIS, JOHN S. The Relationship between Infrared, Optical, and Ultraviolet Extinction. **ApJ**, v. 345, p. 245, Oct 1989b.

[9] CHEN, X. Y., LIANG, Y. C., HAMMER, F., PRUGNIEL, PH., ZHONG, G. H., RODRIGUES, M., ZHAO, Y. H., FLORES, H. Comparing six evolutionary population synthesis models by performing spectral synthesis for galaxies. **A&A**, v. 515, p. A101, Jun 2010.

[10] CID FERNANDES, R., GONZÁLEZ DELGADO, R. M., GARCÍA BENITO, R., PÉREZ, E., DE AMORIM, A. L., SÁNCHEZ, S. F., HUSEMANN, B., FALCÓN BARROSO, J., LÓPEZ-FERNÁNDEZ, R., SÁNCHEZ-BLÁZQUEZ, P., VALE ASARI, N., VAZDEKIS, A., WALCHER, C. J., MAST, D. Resolving galaxies in time and space. II. Uncertainties in the spectral synthesis of datacubes. **Astronomy & Astrophysics, Volume 561, id.A130, <NUMPAGES>19</NUMPAGES> pp.**, v. 561, p. A130, January 2014.

[11] CID FERNANDES, R., GU, Q., MELNICK, J., TERLEVICH, E., TERLEVICH, R., KUNTH, D., RODRIGUES LACERDA, R., JOGUET, B. The star formation history of Seyfert 2 nuclei. **MNRAS**, v. 355, p. 273–296, November 2004.

[12] CID FERNANDES, R., MATEUS, A., SODRÉ, L., STASIŃSKA, G., GOMES, J. M. Semi-empirical analysis of Sloan Digital Sky Survey galaxies - I. Spectral synthesis method. **MNRAS**, v. 358, p. 363–378, April 2005.

[13] CID FERNANDES, R., PÉREZ, E., GARCÍA BENITO, R., GONZÁLEZ DELGADO, R. M., DE AMORIM, A. L., SÁNCHEZ, S. F., HUSEMANN, B., FALCÓN BARROSO, J., SÁNCHEZ-BLÁZQUEZ, P., WALCHER, C. J., MAST, D. Resolving galaxies in time and space. I. Applying STARLIGHT to CALIFA datacubes. **Astronomy and Astrophysics**, v. 557, p. A86, September 2013.

[14] CID FERNANDES, R., STASIŃSKA, G., MATEUS, A., VALE ASARI, N. A comprehensive classification of galaxies in the Sloan Digital Sky Survey: how to tell true from fake AGN? **MNRAS**, v. 413, p. 1687–1699, May 2011.

[15] CID FERNANDES, R., STASIŃSKA, G., SCHLICKMANN, M. S., MATEUS, A., VALE ASARI, N., SCHOENELL, W., SODRÉ, L. Alternative diagnostic diagrams and the 'forgotten' population of weak line galaxies in the SDSS. **MNRAS**, v. 403, p. 1036–1053, April 2010.

[16] CIOTTI, L., OSTRIKER, J. P., PROGA, D. Feedback from Central Black Holes in Elliptical Galaxies. III. Models with Both Radiative and Mechanical Feedback. **ApJ**, v. 717, p. 708–723, July 2010.

[17] CONROY, CHARLIE. Modeling the Panchromatic Spectral Energy Distributions of Galaxies. **ARA&A**, v. 51, n. 1, p. 393–455, Aug 2013.

[18] CROTON, DARREN J., SPRINGEL, VOLKER, WHITE, SIMON D. M., DE LUCIA, G., FRENK, C. S., GAO, L., JENKINS, A., KAUFFMANN, G., NAVARRO, J. F., YOSHIDA, N. The many lives of active galactic nuclei: cooling flows, black holes and the luminosities and colours of galaxies. **MNRAS**, v. 365, n. 1, p. 11–28, Jan 2006.

[19] DAHMER-HAHN, L. G., RIFFEL, R., RODRíGUEZ-ARDILA, A., RIFFEL, R. A., STORCHI-BERGMANN, T., MARINELLO, M., DAVIES, R. I., BURTSCHER, L., RUSCHEL-DUTRA, D., ROSARIO, D. J. Stellar populations in local AGNs: evidence for enhanced star formation in the inner 100 pc. **MNRAS**, v. 509, n. 3, p. 4653–4668, January 2022.

[20] DAHMER-HAHN, LUIS GABRIEL, RIFFEL, ROGÉRIO, RODRíGUEZ-ARDILA, ALBERTO, MARTINS, LUCIMARA P., KEHRIG, CAROLINA, HECKMAN, TIMOTHY M., PASTORIZA, MIRIANI G., DAMETTO, NATACHA Z. Probing evolutionary population synthesis models in the near infrared with early-type galaxies. **MNRAS**, v. 476, n. 4, p. 4459–4480, Jun 2018.

[21] DAVIES, R. I., MACIEJEWSKI, W., HICKS, E. K. S., TACCONI, L. J., GENZEL, R., ENGEL, H. Stellar and Molecular Gas Kinematics Of NGC 1097: Inflow Driven by a Nuclear Spiral. **ApJ**, v. 702, p. 114–128, September 2009.

[22] DAVIES, R. I., MÜLLER SÁNCHEZ, F., GENZEL, R., TACCONI, L. J., HICKS, E. K. S., FRIEDRICH, S., STERNBERG, A. A Close Look at Star Formation around Active Galactic Nuclei. **ApJ**, v. 671, p. 1388–1412, December 2007.

[23] DRORY, N., MACDONALD, N., BERSHADY, M. A., BUNDY, K., GUNN, J., LAW, D. R., SMITH, M., STOLL, R., TREMONTI, C. A., WAKE, D. A., YAN, R., WEIJMANS, A. M., BYLER, N., CHERINKA, B., COPE, F., EIGENBROT, A., HARDING, P., HOLDER, D., HUEHNERHOFF, J., JAEHNIG, K., JANSEN, T. C., KLAENE, M., PAAT, A. M., PERCIVAL, J., SAYRES, C. The MaNGA Integral Field Unit Fiber Feed System for the Sloan 2.5 m Telescope. **AJ**, v. 149, p. 77, February 2015.

[24] ELVIS, M. A Structure for Quasars. **ApJ**, v. 545, p. 63–76, December 2000.

[25] GONZÁLEZ DELGADO, R. M., CERVIÑO, M., MARTINS, L. P., LEITHERER, C., HAUSCHILDT, P. H. Evolutionary stellar population synthesis at high spectral resolution: Optical wavelengths. **Monthly Notices of the Royal Astronomical Society**, v. 357, p. 945–960, March 2005.

[26] HECKMAN, T. M., BEST, P. N. The Coevolution of Galaxies and Supermassive Black Holes: Insights from Surveys of the Contemporary Universe. **ARA&A**, v. 52, p. 589–660, August 2014.

[27] HICKS, E. K. S., DAVIES, R. I., MACIEJEWSKI, W., EMSELLEM, E., MALKAN, M. A., DUMAS, G., MÜLLER-SÁNCHEZ, F., RIVERS, A. Fueling Active Galactic Nuclei. I. How the Global Characteristics of the Central Kiloparsec of Seyferts Differ from Quiescent Galaxies. **ApJ**, v. 768, p. 107, May 2013.

[28] HOPKINS, P. F. Dynamical delays between starburst and AGN activity in galaxy nuclei. **MNRAS**, v. 420, p. L8–L12, February 2012.

[29] KAUFFMANN, G., HECKMAN, T. M., TREMONTI, C., BRINCHMANN, J., CHARLOT, S., WHITE, S. D. M., RIDGWAY, S. E., BRINKMANN, J., FUKUGITA, M., HALL, P. B., IVEZIĆ, Ž., RICHARDS, G. T., SCHNEIDER, D. P. The host galaxies of active galactic nuclei. **MNRAS**, v. 346, p. 1055–1077, December 2003.

[30] KAWAKATU, N., WADA, K. Coevolution of Supermassive Black Holes and Circumnuclear Disks. **ApJ**, v. 681, p. 73–83, July 2008.

[31] KORMENDY, J., HO, L. C. Coevolution (Or Not) of Supermassive Black Holes and Host Galaxies. **ARA&A**, v. 51, p. 511–653, August 2013.

[32] LANÇON, A., GONNEAU, A., VERRO, K., PRUGNIEL, P., ARENTSEN, A., TRAGER, S. C., PELETIER, R., CHEN, Y. P., COELHO, P., FALCÓN-BARROSO, J., HAUSCHILDT, P., HUSSER, T. O., JAIN, R., LYUBENOVA, M., MARTINS, L., SÁNCHEZ BLÁZQUEZ, P., VAZDEKIS, A. A comparison between X-shooter spectra and PHOENIX models across the HR-diagram. **A&A**, v. 649, p. A97, May 2021.

[33] LAW, D. R., YAN, R., BERSHADY, M. A., BUNDY, K., CHERINKA, B., DRORY, N., MACDONALD, N., SÁNCHEZ-GALLEGO, J. R., WAKE, D. A., WEIJMANS, A.-M., BLANTON, M. R., KLAENE, M. A., MORAN, S. M., SANCHEZ, S. F., ZHANG, K. Observing Strategy for the SDSS-IV/MaNGA IFU Galaxy Survey. **AJ**, v. 150, p. 19, July 2015.

[34] LEJA, JOEL, JOHNSON, BENJAMIN D., CONROY, CHARLIE, DOKKUM, PIETER G.VAN , BYLER, NELL. Deriving physical properties from broadband photometry with prospector: Description of the model and a demonstration of its accuracy using 129 galaxies in the local universe. **The Astrophysical Journal**, v. 837, n. 2, p. 170, mar 2017.

[35] LINTOTT, CHRIS, SCHAWINSKI, KEVIN, BAMFORD, STEVEN, SLOSAR, ANå¾E, LAND, KATE, THOMAS, DANIEL, EDMONDSON, EDD, MASTERS, KAREN, NICHOL, ROBERT C., RADDICK, M. JORDAN, SZALAY, ALEX, ANDREESCU, DAN, MURRAY, PHIL, VANDENBERG, JAN. Galaxy Zoo 1: Data release of morphological classifications for nearly 900 000 galaxies. **Monthly Notices of the Royal Astronomical Society**, v. 410, p. 166–178, January 2011.

[36] MALLMANN, NÍCOLAS DULLIUS, RIFFEL, ROGÉRIO, STORCHI-BERGMANN, THAISA, REMBOLD, SANDRO BARBOZA, RIFFEL, ROGEMAR A, SCHIMOIA, JADERSON, DA COSTA, LUIZ NICOLACI, ÁVILA-REESE, VLADIMIR, SANCHEZ, SEBASTIAN F, MACHADO, ALICE D, CIROLINI, RAFAEL, ILHA, GABRIELE S, DO NASCIMENTO, JANAÍNA C. The first 62 AGN observed with SDSS-IV MaNGA – II. Resolvedstellar populations. **Monthly Notices of the Royal Astronomical Society**, v. 478, n. 4, p. 5491–5504, August 2018.

[37] MALLMANN, NíCOLAS DULLIUS, RIFFEL, ROGÉRIO, STORCHI-BERGMANN, THAISA, REMBOLD, SANDRO BARBOZA, RIFFEL, ROGEMAR A., SCHIMOIA, JADERSON, DA COSTA, LUIZ NICOLACI, ÁVILA-REESE, VLADIMIR, SANCHEZ, SEBASTIAN F., MACHADO, ALICE D., CIROLINI, RAFAEL, ILHA, GABRIELE S., NASCIMENTO, JANAíNA C. DO. The first 62 AGN observed with SDSS-IV MaNGA - II. Resolvedstellar populations. **MNRAS**, v. 478, n. 4, p. 5491–5504, Aug 2018.

[38] MALLMANN, NÍCOLAS DULLIUS, RIFFEL, ROGÉRIO. ndmallmann/urutau: Urutau, August 2023.

[39] MARTINS, LUCIMARA P., LIMA-DIAS, CíRIA, COELHO, PAULA R. T., LAGANÁ, TATIANA F. Testing stellar population fitting ingredients with Globular Clusters I: Stellar libraries. **MNRAS**, v. 484, n. 2, p. 2388–2402, Apr 2019.

[40] MO, HOUJUN, VAN DEN BOSCH, FRANK C., WHITE, SIMON. **Galaxy Formation and Evolution**: 2010.

[41] PETERSON, B. M. **Active galactic nuclei**, p. 138. 2009.

[42] RAMOS ALMEIDA, CRISTINA, RICCI, CLAUDIO. Nuclear obscuration in active galactic nuclei. **Nature Astronomy**, v. 1, p. 679–689, Oct 2017.

[43] REMBOLD, S. B., SHIMOIA, J. S., STORCHI-BERGMANN, T., RIFFEL, R., RIFFEL, R. A., MALLMANN, N. D., DO NASCIMENTO, J. C., MOREIRA, T. N., ILHA, G. S., MACHADO, A. D., CIROLINI, R., DA COSTA, L. N., MAIA, M. A. G., SANTIAGO, B. X., SCHNEIDER, D. P., WYLEZALEK, D., BIZYAEV, D., PAN, K., MÜLLER-SÁNCHEZ, F. The first 62 AGNs observed with SDSS-IV MaNGA - I. Their characterization and definition of a control sample. **MNRAS**, v. 472, p. 4382–4403, December 2017.

[44] REMBOLD, SANDRO B., SHIMOIA, JÁDERSON S., STORCHI-BERGMANN, THAISA, RIFFEL, ROGÉRIO, RIFFEL, ROGEMAR A., MALLMANN, NÍCOLAS D., DO NASCIMENTO, JANAÍNA C., MOREIRA, THALES N., ILHA, GABRIELE S., MACHADO, ALICE D., CIROLINI, RAFAEL, DA COSTA, LUIZ N., MAIA, MARCIO A. G., SANTIAGO, BASÍLIO X., SCHNEIDER, DONALD P., WYLEZALEK, DOMINIKA, BIZYAEV, DMITRY, PAN, KAIKE, MÜLLER-SÁNCHEZ, FRANCISCO. The first 62 AGNs observed with SDSS-IV MaNGA - I. Their characterization and definition of a control sample. **Monthly Notices of the Royal Astronomical Society**, v. 472, p. 4382–4403, December 2017.

[45] RIFFEL, R., PASTORIZA, M. G., RODRíGUEZ-ARDILA, A., BONATTO, C. Probing the near-infrared stellar population of Seyfert galaxies. **MNRAS**, v. 400, p. 273–290, November 2009.

[46] RIFFEL, R., PASTORIZA, M. G., RODRíGUEZ-ARDILA, A., DAMETTO, N. Z., RUSCHEL-DUTRA, D., RIFFEL, R. A., STORCHI-BERGMANN, T., MARTINS, L. P., MASON, R., HO, L. C., PALOMAR XD TEAM, . **Models Constraints from Observations of Active Galaxies**, v. 497 of **Astronomical Society of the Pacific Conference Series**, p. 459. 2015.

[47] RIFFEL, R. A., COLINA, L., STORCHI-BERGMANN, T., PIQUERAS LÓPEZ, J., ARRIBAS, S., RIFFEL, R., PASTORIZA, M., SALES, D. A., DAMETTO, N. Z., LABIANO, A., DAVIES, R. I. A SINFONI view of the nuclear activity and circumnuclear star formation in NGC 4303. **MNRAS**, v. 461, p. 4192–4205, October 2016.

[48] RIFFEL, ROGÉRIO, DAHMER-HAHN, LUIS G., RIFFEL, ROGEMAR A., STORCHI-BERGMANN, THAISA, DAMETTO, NATACHA Z., DAVIES, RICHARD, BURTSCHER, LEONARD, BIANCHIN, MARINA, RUSCHEL-DUTRA, DANIEL, RICCI, CLAUDIO, ROSARIO, DAVID J. Gemini NIFS survey of feeding and feedback processes in nearby active galaxies - VI. Stellar populations. **MNRAS**, v. 512, n. 3, p. 3906–3921, May 2022.

[49] SÁNCHEZ, S. F., WALCHER, C. J., LOPEZ-COBÁ, C., BARRERA-BALLESTEROS, J. K., MEJÍA-NARVÁEZ, A., ESPINOSA-PONCE, C., CAMPS-FARIÑA, A. From Global to Spatially Resolved in Low-Redshift Galaxies. **Revista Mexicana de Astronomia y Astrofisica**, v. 57, p. 3–38, April 2021.

[50] SÁNCHEZ, SEBASTIÁN F. Spatially Resolved Spectroscopic Properties of Low-Redshift Star-Forming Galaxies. **Annual Review of Astronomy and Astrophysics, vol. 58, p.99-155**, v. 58, p. 99, August 2020.

[51] SARZI, M., ALLARD, E. L., KNAPEN, J. H., MAZZUCA, L. M. Star formation and stellar populations across nuclear rings in galaxies. **MNRAS**, v. 380, p. 949–962, September 2007.

[52] SCHLEGEL, D. J., FINKBEINER, D. P., DAVIS, M. Maps of Dust Infrared Emission for Use in Estimation of Reddening and Cosmic Microwave Background Radiation Foregrounds. **ApJ**, v. 500, p. 525–553, June 1998.

[53] SMEE, STEPHEN A., GUNN, JAMES E., UOMOTO, ALAN, ROE, NATALIE, SCHLEGEL, DAVID, ROCKOSI, CONSTANCE M., CARR, MICHAEL A., LEGER, FRENCH, DAWSON, KYLE S., OLMSTEAD, MATTHEW D., BRINKMANN, JON, OWEN, RUSSELL, BARKHOUSER, ROBERT H., HONSCHEID, KLAUS, HARDING, PAUL, LONG, DAN, LUPTON, ROBERT H., LOOMIS, CRAIG, ANDERSON, LAUREN, ANNIS, JAMES, BERNARDI, MARIANGELA, BHARDWAJ, VAISHALI, BIZYAEV, DMITRY, BOLTON, ADAM S., BREWINGTON, HOWARD, BRIGGS, JOHN W., BURLES, SCOTT, BURNS, JAMES G., CASTANDER, FRANCISCO JAVIER, CONNOLLY, ANDREW, DAVENPORT, JAMES R.A., EBELKE, GARRETT, EPPS, HARLAND, FELDMAN, PAUL D., FRIEDMAN, SCOTT D., FRIEMAN, JOSHUA, HECKMAN, TIMOTHY, HULL, CHARLES L., KNAPP, GILLIAN R., LAWRENCE, DAVID M., LOVEDAY, JON, MANNERY, EDWARD J., MALANUSHENKO, ELENA, MALANUSHENKO, VIKTOR, MERRELLI, ARONNE JAMES, MUNA, DEMITRI, NEWMAN, PETER R., NICHOL, ROBERT C., ORAVETZ, DANIEL, PAN, KAIKE, POPE, ADRIAN C., RICKETTS, PAUL G., SHELDEN, ALAINA, SANDFORD, DALE, SIEGMUND, WALTER, AUDREY SIMMONS, , SHANE SMITH, D., SNEDDEN, STEPHANIE, SCHNEIDER, DONALD P., RAO, MARK SUBBA, TREMONTI, CHRISTY, WADDELL, PATRICK, YORK, DONALD G. The multi-object, fiber-fed spectrographs for the Sloan Digital Sky Survey and the Baryon Oscillation Spectroscopic Survey. **Astron. J.**, 2013.

[54] SOMERVILLE, R. S., HOPKINS, P. F., COX, T. J., ROBERTSON, B. E., HERNQUIST, L. A semi-analytic model for the co-evolution of galaxies, black holes and active galactic nuclei. **MNRAS**, v. 391, p. 481–506, December 2008.

[55] STEINER, J. E., MENEZES, R. B., RICCI, T. V., OLIVEIRA, A. S. PCA Tomography: How to extract information from data cubes. **Monthly Notices of the Royal Astronomical Society**, v. 395, p. 64–75, May 2009.

[56] STORCHI-BERGMANN, T., GONZÁLEZ DELGADO, R. M., SCHMITT, H. R., CID FERNANDES, R., HECKMAN, T. Circumnuclear Stellar Population, Morphology, and Environment of Seyfert 2 Galaxies: An Evolutionary Scenario. **ApJ**, v. 559, p. 147–156, September 2001.

[57] STORCHI-BERGMANN, THAISA, SCHNORR-MÜLLER, ALLAN. Observational constraints on the feeding of supermassive black holes. **Nature Astronomy**, v. 3, n. 1, p. 48–61, jan 2019.

[58] TERLEVICH, E., DIAZ, A. I., TERLEVICH, R. On the behaviour of the IR CA II triplet in normal and active galaxies. **MNRAS**, v. 242, p. 271–284, January 1990.

[59] VAZDEKIS, A., KOLEVA, M., RICCIARDELLI, E., RÖCK, B., FALCÓN-BARROSO, J. UV-extended E-MILES stellar population models: Young components in massive early-type galaxies. **Monthly Notices of the RAS**, v. 463, p. 3409–3436, December 2016.

[60] VÁZQUEZ-MATA, J. A., HERNÁNDEZ-TOLEDO, H. M., AVILA-REESE, V., HERRERA-ENDOQUI, M., RODRÍGUEZ-PUEBLA, A., CANO-DÍAZ, M., LACERNA, I., MARTÍNEZ-VÁZQUEZ, L. A., LANE, R. SDSS IV MaNGA: Visual morphological and statistical characterization of the DR15 sample. **Monthly Notices of the Royal Astronomical Society**, v. 512, p. 2222–2244, May 2022.

[61] ZUBOVAS, K., BOURNE, M. A. Do AGN outflows quench or enhance star formation? **MNRAS**, v. 468, p. 4956–4967, July 2017.